Summer 2010

Investigating the source of thermal anomalies in the northern United Arab Emirates (UAE) desert using geophysical methods

Khalid Ahmad

Department: Geosciences and Geological and Petroleum Engineering

INVESTIGATING THE SOURCE OF THERMAL ANOMALIES IN THE NORTHERN UNITED ARAB EMIRATES (UAE) DESERT USING GEOPHYSICAL METHODS

by

KHALID AHMAD

A DISSERTATION

Presented to the Faculty of the Graduate School of the

MISSOURI UNIVERSITY OF SCIENCE AND TECHNOLOGY

In Partial Fulfillment of the Requirements for the Degree

DOCTOR OF PHILOSOPHY

in

GEOPHYSICS

2010

Approved by

Estella Atekwana, Advisor
Abdeldjelil Belarbi
Jeffery Cawlfield
J David Rogers
Farouk El Baz
Neil Anderson

ABSTRACT

We conducted geophysical surveys to investigate the source of thermal anomalies and to delineate any potential water transport pathways from the recharge zones in the Oman Mountains to the location of the temporal thermal anomalies within the desert plain of the United Arab Emirates (UAE). In the visible region of the spectrum of both ASTER and MODIS satellite images, the desert plain of the UAE appears as a bare sandy surface. However, detailed examination of these images in the thermal bands reveal cooler thermal anomalies within the desert plain following major rainfall events. This anomaly has a cooler surface of approximately 20 ºC lower than the surroundings with a lifespan of several days. It has been hypothesized that moist surfaces, following rainfall events in an arid hot desert could be an indirect indication of locations with groundwater accumulation. Two regional fault zones, Dibba (DFZ) (NE-SW) and Hatta (HFZ)(NW-SE) were traced from ASTER satellite images and SRTM (~90 m) elevation data, but it remained unclear whether they extend into the thermal anomaly area.

Audiomagnetotelluric (AMT) and ground magnetic data were acquired to verify the possible extension of these fault zones into the thermal anomaly area. AMT data were acquired along profiles positioned perpendicular to the DFZ and HFZ trends and over a 3-D survey grid covering the anomaly area. The ground magnetic survey delineated the extension of both fault zones into the gravel plains area but not into the anomaly area probably due to the thicker sand cover. 2D AMT apparent resistivity sections show a low resistivity structure coincident with the thermal anomalies that parallel the DFZ trend. A conductive structure over the thermal anomaly area, coincident with the extension of the HFZ, was characterized from AMT 2-D inversions. The results suggest that the DFZ and HFZ extend from the recharge areas in the mountain into the desert plains. The results also suggest that these faults play a vital role in transmitting infiltrated rainwater from the Oman Mountains into the desert plain of the UAE where freshwater accumulates after rainfall events causing the thermal anomalies.

.

ACKNOWLEDGMENTS

I would like to express my deepest appreciation to Dr. Estella Atekwana for her guidance and support. I feel privileged and honored to be her student and grateful to be part of her research group. I would like to thank the members of my committee, Dr. J Dave Rogers, Dr. Faouk El Baz, Dr. Neil Anderson, Dr. Jeffrey Cawlfield, and Dr. Abdeldjelil Belarbi for volunteering their time.

Dr. Farouk El Baz and Dr. Eman Ghoneim form the Center for remote sensing-Boston University introduced the idea of this project to me and provided valuable advise. They also provided me with the remote sensing data. Also, I would like to thank Dr. Maxwell Meju from Lancaster University-UK for his guidance in the design of the magnetotelluric (MT) survey and for providing me with the instruments used to acquire the MT data. I would like to offer my sincere gratitude to the United Arab Emirates University for providing the financial support and funding of the research work. I am thankful to my friends Mohammad Amiri, Bader Shaheen, and Moeen Mosa for their their help with the acquisitions of the magnetic and MT data. The National Centre of Meteorology and Seismology (NCMS) of UAE provided logistical support during the fieldwork. I am grateful to Mr. Abdulla Al Mandoos the general manager of NCMS for accepting my request and special thanks to Mr. Khalid Al Ziraihi and Mr. Omar Diraz form NCMS for their help with AMT data acquisition. The Dubai government provided funding for fieldwork. Many thanks to Dr. A. Bin Hazeem and A. bin Humaidan from Dubai government for their cooperation. Also I appreciate Mr. Ghaith Al Ghaith and Mr. Greg Simkins from Emirates Airlines for helping me with the permission to survey within Emirates Airline's properties (Dubai Desert Conservation Reserve (DDCR)). Many thanks to Dr. Kevin Mickus from Missouri State University and Dr. George Jiracek from San Diego State University for helping with processing of the MT data and for providing me with the WinGLink software. Finally, I would like to thank Oklahoma State University for allowing me to use their facilities during this project.

This work would not have been posible without the love and support of my parents, my wife Muna, my sisters, my brothers, and my children Ayesha, Roudha, and Shamsa.

TABLE OF CONTENTS

LIST OF ILLUSTRATIONS

LIST OF TABLES

1. INTRODUCTION

1.1. BACKGROUND

Urban development in the United Arab Emirates (UAE) (Figure. 1.1) is limited due to scarcity of water supply. The population growth in the last three decades has caused a rapid increase in the rate of water consumption. Since groundwater is consumed rapidly and not recharged due to the arid climatic condition of the UAE, this situation demands the country to find other sources of water. Despite the high costs, seawater desalinization is the best solution for this problem. Transporting the desalinized water to the country's interior is costly. Therefore the coastal cities will benefit from desalinized seawater, but the interior cities will remain dependent on the conventional ground water resources. There is a need to identify potential areas for groundwater resources. Therefore, thermal satellite infrared imaging (TIR) techniques have been used for hydrological exploration in the UAE. In a recent study, thermal images of the northern UAE acquired in 2002 and 2003 showed cooler thermal anomalies in a specific area of the northern UAE (Figure 1.2). The cause of the anomaly is suggested to result from soil temperature variation due to cooler groundwater (Ghoneim et al., 2005). It has been hypothesized that the source of groundwater are buried faults underlying the study area that transport the ground water from the recharge area in the mountain to the aquifers beneath the anomaly area. These faults the Dibba Fault Zone (DFZ) and Hatta Fault Zone (HFZ) are exposed in the mountain (Figure. 1.3). Due to the size of the anomaly area, the use of wells to investigate the cause of the anomaly will be costly. Additionally, limited geologic outcrops prevent any field geologic mapping. Thus there is a need to find alternative technology to ground truth the thermal anomaly. In this respect, geophysical methodologies offer a great advantage of investigating the cause of the thermal anomaly.

Hydrogeophysical investigations are limited in UAE, as most geophysical investigations are mainly for oil exploration. However, there is a need for identifying new sources of water. Also, there is a need to train a new generation of UAE citizens in geophysics applied to hydrologic investigations. This study however is timely because it fulfills part of this vision and should result in capacity building in the UAE.

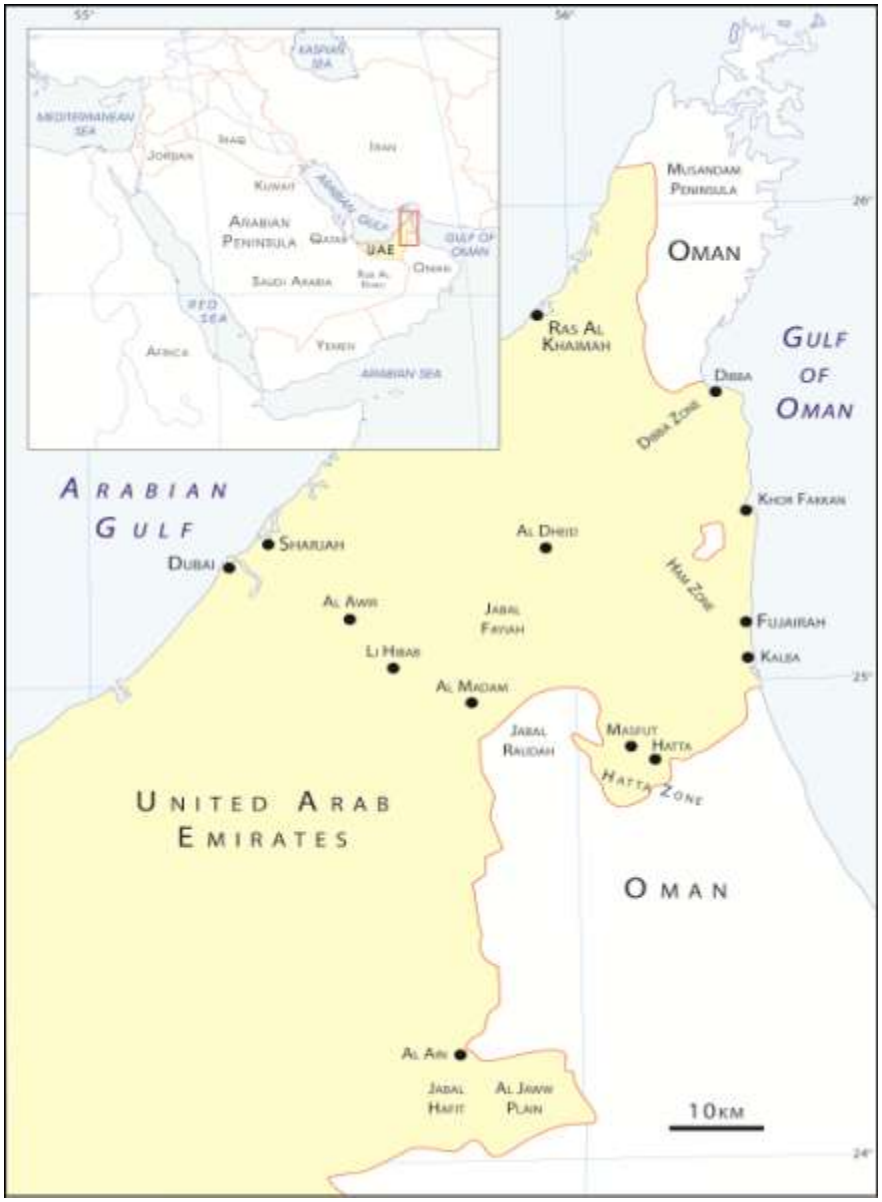

Figure 1.1. Location Map of the northern United Arab Emirates.

Groundtruthing of anomalies mapped from remote sensing data is often verified by drilling or structural geologic mapping (Ghoneim et al., 2005). However, in desert environments such as in the UAE where outcrops are limited or buried, geophysical methods may play an important role in groundtruthing the satellite data.

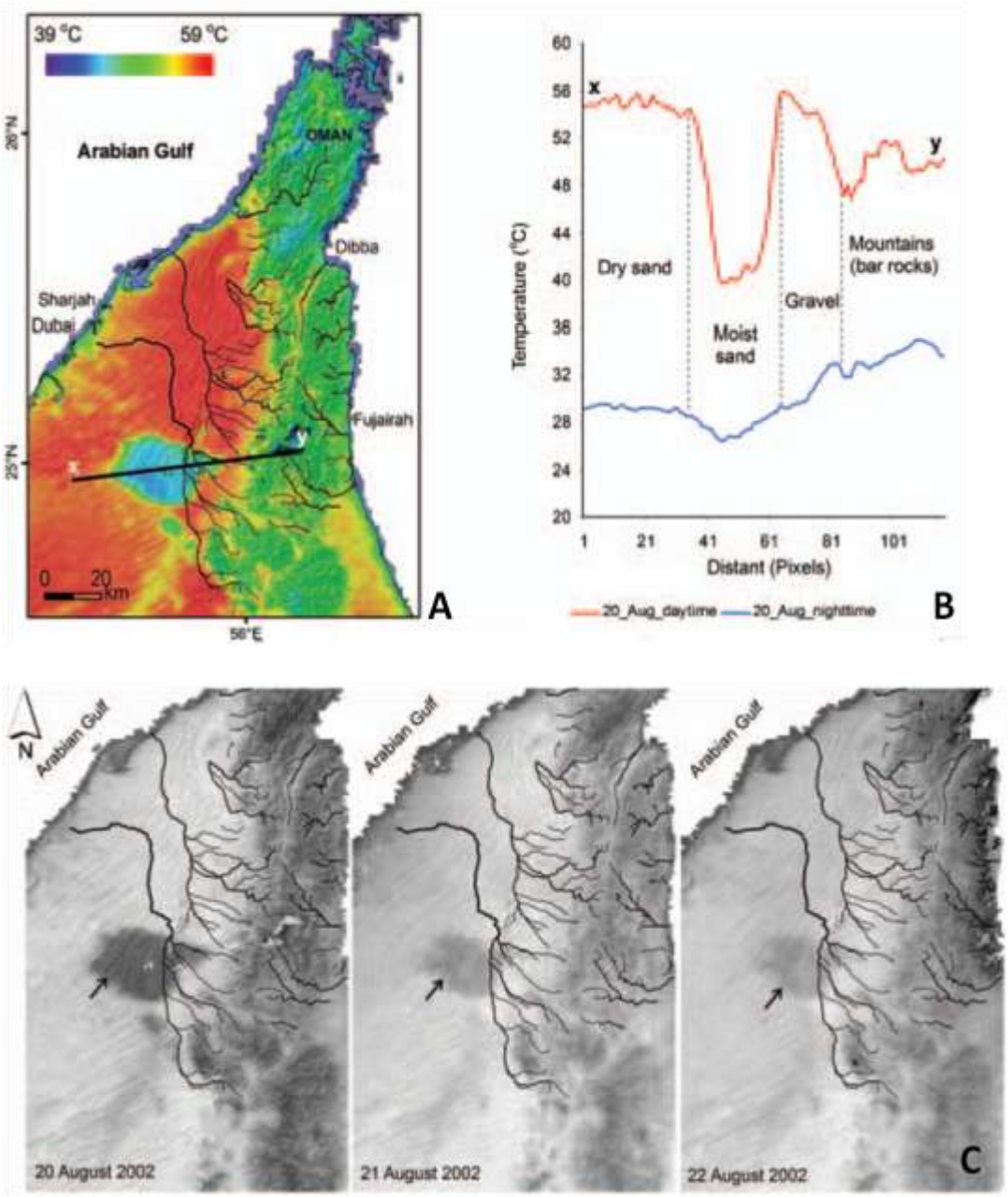

Figure 1.2. A) Thermal-infrared images of the northern United Arab Emirates acquired in 2002 show a cooler surface of approximately 20 ºC lower than the surrounding. B) The graph shows temperature response to the moist soil, dry soil and dry gravel. C) The thermal anomaly has a lifespan of several days, from (Ghoneim, 2008).

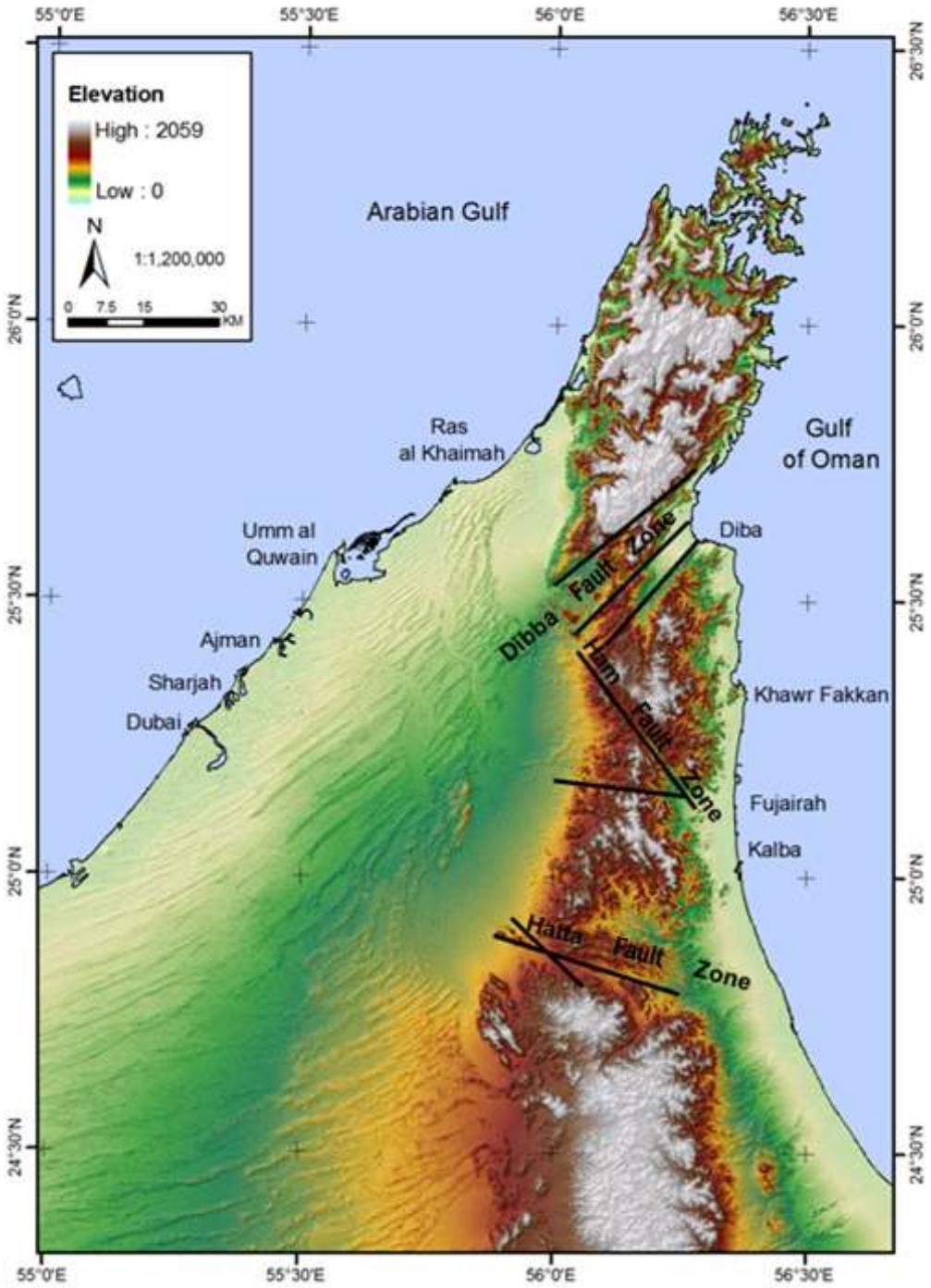

Figure 1.3. Major fault zones of the northern United Arab Emirates mapped from Digital Elevation Models (DEM) image (Ghoneim et al., 2005). The Dibba and Hatta fault zones are exposed in the mountains.

1.2. STUDY AREA

The study is located in the northern UAE. The UAE lies in the southeastern part of the Arabian Peninsula between Latitudes 22° 40´ and 26° 00´ N and Longitudes 51° 00´ and 56° 00´ E (Figure 1.1). It is bordered on the north by the Arabian Gulf, on the east by the Sultanate of Oman and the Gulf of Oman and on the south and the west by the Kingdom of Saudi Arabia (Figure 1.1). The total area of the UAE is about $83000km^2$. This study is located within the gravel and desert plains of the northern UAE.

1.3. CLIMATIC CONDITIONS

The UAE is located in one of the hottest regions of the world and is characterized by a uniform temperature that is hot, arid and dry in the summer season and mild in the winter season, except in the mountain area to the east where the temperatures are lower due to the elevations that reach 2000 m. The average daytime temperature in the summer season (May – September) is 40°C and the temperature reaches a maximum in July. In the winter season (November – March), the average daytime temperature is 25°C and the temperature reaches the minimum in January (Rizk, 1999). Straddling the Tropic of Cancer, the UAE's climate as a result is classified subtropical. It receives the maximum solar radiation on June 21st when the incident angle of the sun rays is 90° and the minimum influence of the sun on UAE on Dec 21st when the incident angle of the sun rays is 43° (Garamoon, 1996).

The UAE receives infrequent amounts of rainfall from year to year. In addition, several years may pass with no rain. Most of the precipitation/rainfall occurs on the eastern mountains and decreases towards the west within the gravel plain, desert and west coast. The annual average rainfall is 110 mm and the highest rainfall recorded was 205 mm in 1986. The rainfall in the UAE is controlled by two sources; NW winds from the Mediterranean that cause the rain in the winter season, and in the summer, the northern part of the UAE receives a small amount of rain from the Indian Ocean (Al Sharhan et al., 2001).

The humidity in UAE is affected mainly by the two water bodies that border the UAE, the Arabian Gulf and the Gulf of Oman. Relative humidity declines sharply moving inland. For example it reaches 60% or more in Abu Dhabi, 45% in Al Ain and

25% at southern UAE boarders with Saudi Arabia in Rub Al Khali area (Figure 1.1). The monthly average relative humidity in the summer is around 50% and 60% during the winter (Al Sharhan et al., 2001).

High temperature, low humidity, and long hours of sunshine are contributing factors raising the rate of the evaporation in the UAE (Ministry of Agriculture and Fisheries, 1981). Most parts of the UAE are characterized by high evaporation rates. The annual evaporation rates reach 12 mm/day in the western and southwestern desert which is the highest rate in the UAE. The eastern mountains of the UAE, western gravel plain, and foreland desert has the second highest annual evaporation rate that ranges between 10-11 mm/day. Coastal areas have the lowest annual evaporation rates in the UAE where evaporation rates reaches between 7.5-8 mm/day in the western coast, and increase on the eastern coast to 9-9.5 mm/day due to the high wind speed (Al Sharhan et al., 2001).

1.4. PREVIOUS WORK

1.4.1. Geophysical and Geological Investigations of Al Jaw Plain. Seismic profiles (Figure 1.4) of the gravel plain (Al Jaw Plain) in Al Ain city (See figure 1.1 for location) documented the presence of a buried system of folds and thrust faults under the Al Jaw Plain. Also, this study shows that a very complex structure system of folds and faults underlies the sand dunes area in northern Al Jaw Plain (Woodward and Al Sharhan, 1994).

Noweir and Al Sharhan (2000) investigated the Huwayyah Anticline north of the Al Jaw Plain in Al Ain area. The structural interpretation of this study suggests that the Huwayyah Anticline developed above within the Semail Ophiolite, at the time of the Ophiolite emplacement. Both case studies of the Al-Jaw Plain area suggest that faults zones within the subsurface layers (including ophiolite) are present. Since the Al Jaw area has lithologic and stratigraphic similarity with the study area, there is a good possibility of fault occurrence in the study area.

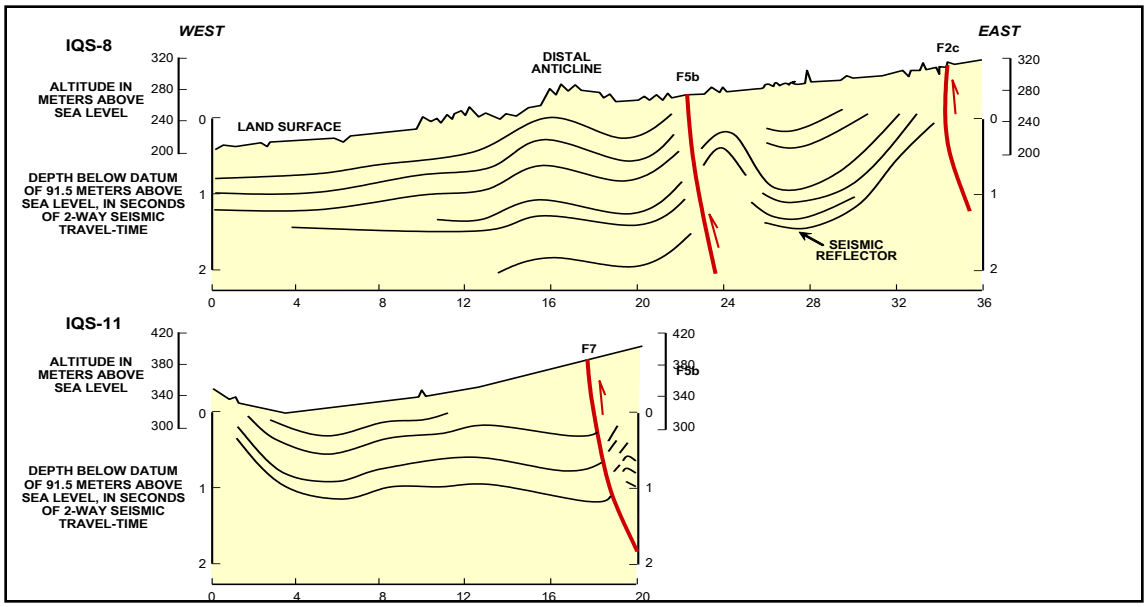

Figure 1.4. Interpreted seismic lines at Al Jaw Plain and north of Al Jaw Plain, (modified after Woodward, 1994).

1.4.2. Thermal Infrared Imaging. The United Arab Emirates (UAE) government used remote sensing investigations for purpose of groundwater exploration in the northern UAE (Figure 1.1) during 2002 to 2004. Satellite Thermal infrared (TIR) data were used to map temperature variations in the sand dunes area in the northern UAE. This study documented cooler thermal anomalies that might indicate possible soil moisture. Systematic analyses of the cloud free daytime images of both the Advanced Spaceborne Thermal Emission and Reflection (ASTER) and Moderate Resolution Imaging Spectroradiometer (MODIS) Land Surface Temperature (LST) images and data correlated with those of the Tropical Rainfall Measuring Mission (TRMM) rainfall revealed a large cooler anomaly in the western desert plain.

Satellite thermal infrared images (TIR) of the northern UAE on 20 August 2002 (Figure 1.2), showed an anomaly in the area between Li Hibab town (Dunes Area) and the vicinity of the Fayah Mountain. The anomaly was roughly circular in shape ~20 km in diameter. The difference in the recorded temperature was about 20º C (Ghoneim,

2008). The image was compared with images of the day before and the days after 20 August 2002 to interpret the cause of the anomaly. The data from August 19th did not show any anomalies, but the data from the days after August 20th showed the anomaly at the same place with the size of the anomaly decreasing as time progressed with a lifespan of more than three days (Figure 1.2). A year later, thermal anomalies appeared again on August 9th 2003 in the same area but with a linear shape trending NE-SW as shown in (Figure 1.6). The difference in the recorded temperature was about 13º C, and vanished within a period of 5 days (Ghoneim et al., 2005). Meteorological records (based mainly on the TRMM space data) (Figure 1.5) suggested the occurrence of a major rainfall event in the mountain areas prior to the appearance of the thermal anomaly. Therefore, it has been hypothesized that subsurface water accumulation might be the cause of the appearance of the thermal anomalies.

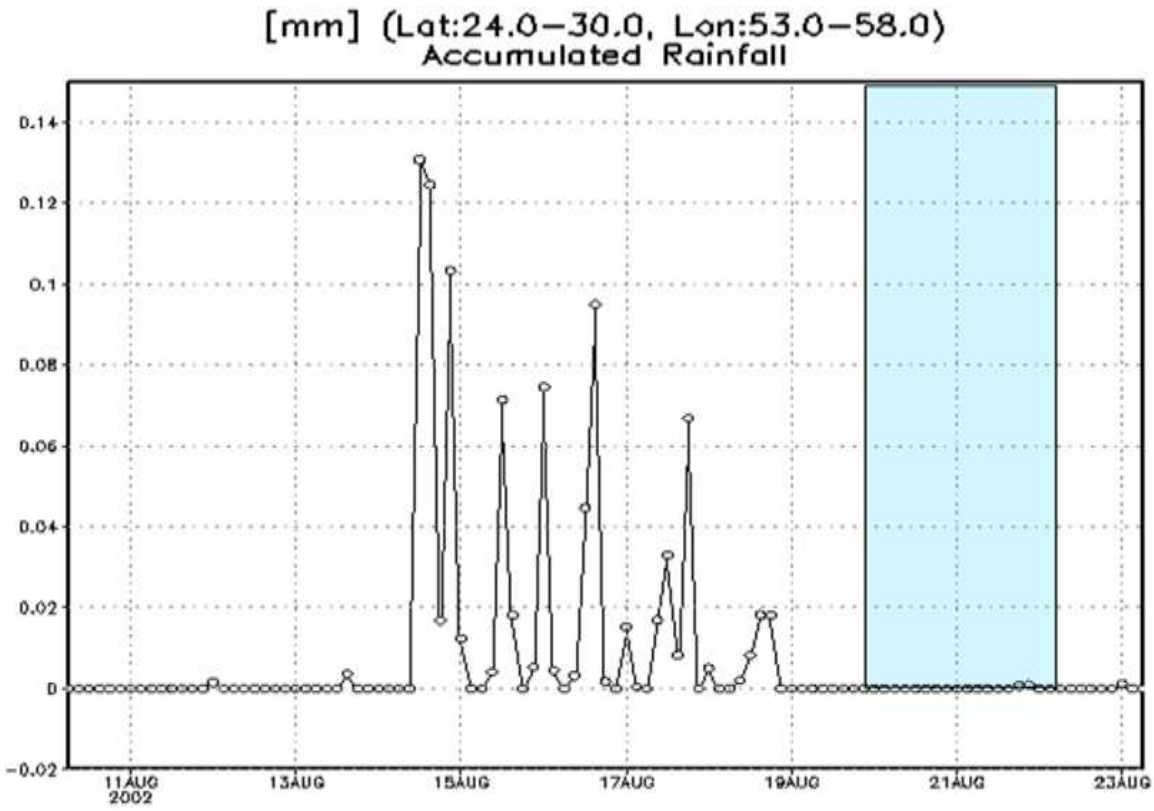

Figure 1.5. Tropical Rainfall Measuring Mission (TRMM) data of August 2002, from (Ghoneim et al., 2005). Blue area represents the time when the thermal anomalies appeared.

Ghoneim et al., (2005) reported that the major faults in the region, particularly those occupied by major drainages, are most likely acting as subterranean streams that facilitate the transport of the rainwater for long distances underground. Along these faults, water moves (surface and subsurface) from the Oman Mountains (recharge zone) to the nearby western desert plain (discharge zone). Fractures play a key role in enhancing groundwater recharge, especially when they control major drainage courses. Fractures form important loci for groundwater (Singhal and Gupta 1999), where they control recharge from rainfall, particularly in mountainous regions.

Two regional fault zones, Dibba (DFZ) (NE-SW) and Hatta (HFZ) (NW-SE) were traced from ASTER satellite images and Shuttle Radar Topography Mission (SRTM) (~90 m) elevation data, but it remains unclear whether they intersect in the thermal anomaly area. Therefore, the current study investigates the possible western extension of the two fault zones and determines the possible relationship between such anomalies and lineaments in the western desert plain area. It has been hypothesized that moist surfaces, following rainfall events in an arid hot desert, could be an indirect indication of locations with groundwater accumulation (Ghoneim et al., 2005).

Results obtained from remote sensing data are required to be verified either by drilling or by field mapping of the structural geology of the investigated site. However, in desert environments such as in the UAE where outcrops are limited or buried, geophysical methods most likely play a significant role in validating results derived from space data. Accordingly, both the audiomagnetotelluric and ground magnetic methods were utilized in the present study to verify the cause of the thermal anomaly.

1.5. OBJECTIVES

The purpose of this study is to test the hypothesis that thermal anomalies observed on remote sensing images over the deserts of United Arab Emirates are the result of cooler shallow water reservoir fed by subsurface faults (DFZ & HFZ) extending from the Hajar Mountains. Therefore, the objectives of this study are to utilize geophysical techniques to verify the cause of the thermal anomaly by:

- Investigating the possible extension of the DFZ and HFZ.
- Mapping any potential aquifers in the study area.

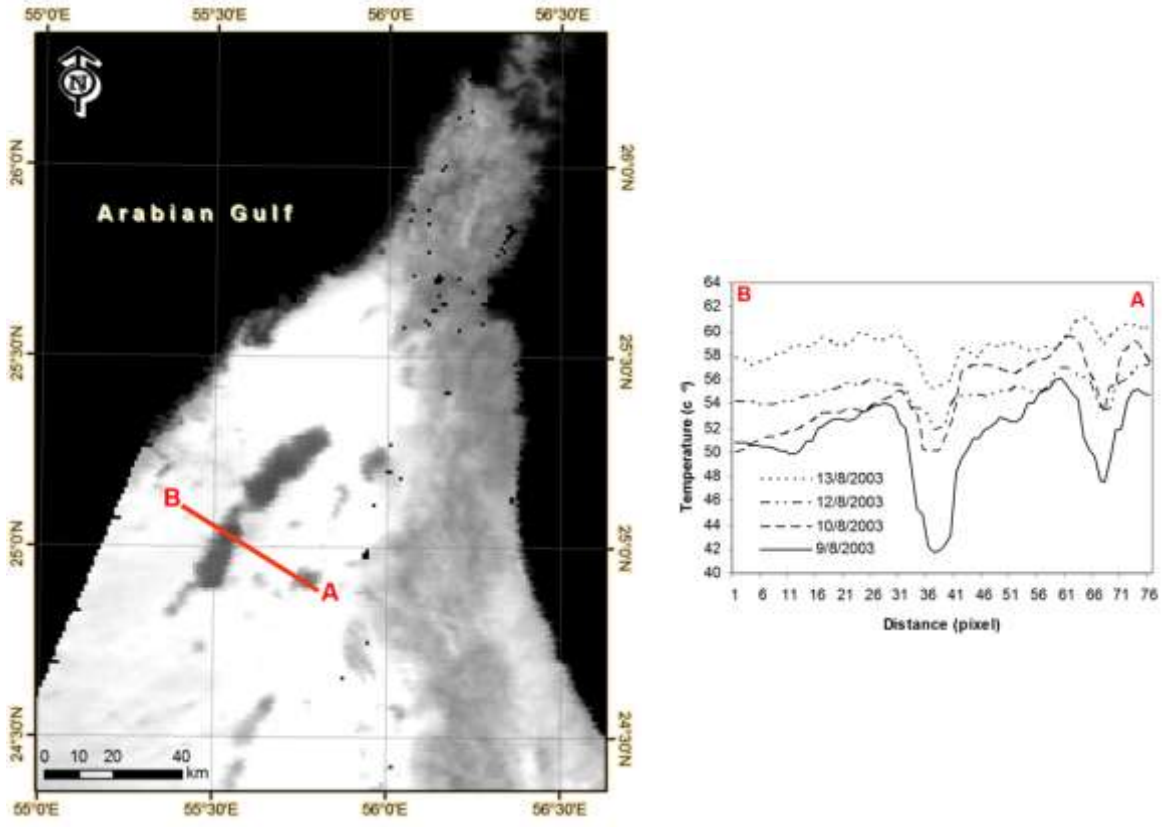

Figure 1.6. Thermal anomaly appears in Aug 03 a year after the first anomaly and a cross section A-B through the anomalies, from (Ghoneim et al., 2005).

2. GEOLOGY

2.1. INTRODUCTION

The UAE is located in the NE edge of the Arabian plate (Kusky et al., 2005). The Arabian plate was part of the African plate and known as the Afro-Arabian plate. Tectonically, both the Arabian and African plates act as a unit. Arabia was separated from the Afro-Arabian plate during the Cenozoic Era (25 m.y.), with Arabia moving away from Africa towards the northeast resulting in opening of the Red Sea and impacting the Eurasian plate causing the Zagros thrusting zone (Edgell et al., 2006).

Since the UAE is located on the eastern part of Arabia, both UAE and Arabia have the same sedimentary sequence. In the eastern margin of the Arabian Shield, the Precambrian continental basement is covered by a sequence of younger Phanerozoic sedimentary rocks ranging in age from Cambrian to the Quaternary and having a thickness from zero to 15 km. Part of this sequence is exposed only in the northern Hajar Mountains (Figure. 2.1) on the northeast Arabia and a series of anticline ridges such as the Hafit and Faiyah ridges (Figure 2.1) at the eastern edge of the desert plain (Ministry of Agriculture and Fisheries, 1981).

Due to the geomorphologic conditions of the UAE where most of the lands are covered by sand dunes (90%) (Al-Nuaimi et al., 2003), the geological history of the UAE is known from outcrops exposed in the Hajar Mountains, seismic data acquired for oil exploration, and well information only. This chapter provides a brief description of the geological, geomorphologic setting, and hydrological setting of the northern UAE. In addition, the geological and structural setting of the DFZ, HFZ and the area of the thermal anomalies is also discussed.

2.2. GEOLOGICAL SETTING OF THE NORTHERN UAE

Glennie et al., (1974) divided the geology of the northern UAE into three major rock units based on their origins which include from youngest to oldest: autochthonous units, allochthonous units, and neo-autochthonous units (Figure 2.1).

Figure 2.1. Geologic Map of northern United Arab Emirates modified from (Noweir et al., 1998).

2.2.1. The Autochthonous Units of Northern UAE. These units are represented by the Hajar Super Group (Figure 2.2) with a thickness of 3700 m overlying the Precambrian basement, and considered to be a stable part of Arabian Platform underlying most of the UAE.

The Hajar Super Group consists of shallow-water shelf carbonates deposited on the Arabian continental passive margin from the Permian to the Cenomanian except for

the deep water limestone and cherts that were deposited as a result of sea level transgression during the Upper Jurrasic to Lower Cretaceous (Kazmin et al., 1986). The Hajar Super Group is exposed to the north of the DFZ forming the Musandam Peninsula. This group is divided into five subgroups (Figure 2.1), from older to younger, Ru'us Al Jibal, Elphinstone, Musandam, Wasia and Aruma (Lippard et al., 1982).

2.2.2. Allochthounus Units of Northern UAE. Allochthounous Units of the Northern UAE are associated with ocean curst emplacement on the northeastern Arabia during Mesozoic. Glennie et al., (1974) divided these units into four subgroups described from the base to top as follow:

2.2.2.1 Sumeini group. In the northern UAE, a succession of Permian to mid-Cretaceous (Cenomanian) sediments known as Sumeini Group underlies the Hawasina complex, cherty Muti Formation, and Maastrichtian shallow marine limestone. These units resulted from obducted continental slope sediments. Glennie et al. (1973) considered the Sumeini Group a parautochthonous rock unit due to the distance of transport from the original depositional site which is relatively small compared to the other allochthounus units (i.e. Hawasina Complex, Haybi Complex and Semail Ophiolite). These sequences are comprised of thin-bedded argillaceous lime mudstones with inter-bedded slope facies conglomerates, breccias and olistostorme deposits (Searle, 1988).

2.2.2.2 Hawasina group. The Hawasina sediments were deposited on the continental slope and Deep Ocean in the Tethyan ocean floor. Hawasina Group deposition is equivalent in time to the Sumeini Group and the Hajar Super Group from Middle Permian to Cretaceous. Unlike the Sumeini rock units which were deposited on the slope between the continental edge and the ocean floor, the Hajar Super Group rock units were deposited in a shallow-water environment, the Hawasina sediments were deposited in extremely deep ocean, then uplifted and transported to the continental margin pushing beneath it the Sumeini Group that were deposited on the continental slope to overlie the Hajar Super Group in eastern Arabia. As a result, these rocks are highly deformed in the northern UAE. This process occurred during the movement of the Semail Ophiolite (Oman and UAE Ophiolite) in Late Cretaceous. Therefore, huge Semail Ophiolite nappes overly the Hawasina group, and both are uncomfortably overlain by the

Maastrichtian and early Tertiary sedimentary rocks (Glennie et al., 1973 & 1974). Lithologically, the Hawasina sequence is comprised of quartz sand, conglomerates, carbonate turbidities, silicified limestone, radiolarian chert, shallow marine limestone associated with deep water sediments and substrate of sheared basalt pillow lavas (Al Sharhan and Nairn, 1997).

2.2.2.3 Haybi group. Searle and Malpas (1980) have documented an allochthonous rock unit that lies between Semail Ophiolite to the top and the Hawasina group sediments below, named the Haybi Complex (Figure 2.2). The Haybi and Hawasina have similar lithological composition but the Haybi is characterized by basic volcanic and metamorphic units such as serpentinite, since this unit is attached to the obducted igneous materials.

2.2.2.4 Semail Ophiolite. The UAE and Oman Ophiolites (Figure 2.1) known as the Semail Ophiolite, are the largest and the best exposed Ophiolites in the world (Pearce et al., 1981). The total area of the Semail Ophiolite is more than 1000 km^2, about 550 km long and up to 150 km in width (Searle and Cox, 1999). The thickness of the complete ophiolite sequence obducted onto eastern Arabia is 12 km (Searle, 1988). The obduction of the Semail Ophiolite occurred during the Turonian to Campanian (71-90 m.a.), pushing beneath it and in front of it the rest of the Allochthounus units that have been discussed in previous sections**.**

The ophiolite sequence lithology is characterized by radiolarian cherts, pillow lavas, sheeted dykes, gabbros and cumulate peridotite-gabbros and upper mantle harzburgite and dunite (Searle and Cox, 1999). Compared to the other Allochthounus units in the UAE, the Ophiolite occupies most of the Hajar Mountains within UAE and extends from the DFZ in the north to the HFZ in the south.

2.2.3. The Neoautochthonous Units of Northern UAE. The sediments that overlie Late Cretaceous nappes are known as neoautochthonous units. This succession is dominted by limestone sediments that are ~ 600 m thick and refers to Maastrichtian, Paleocene and Eocene ages (Glennie et al., 1974).

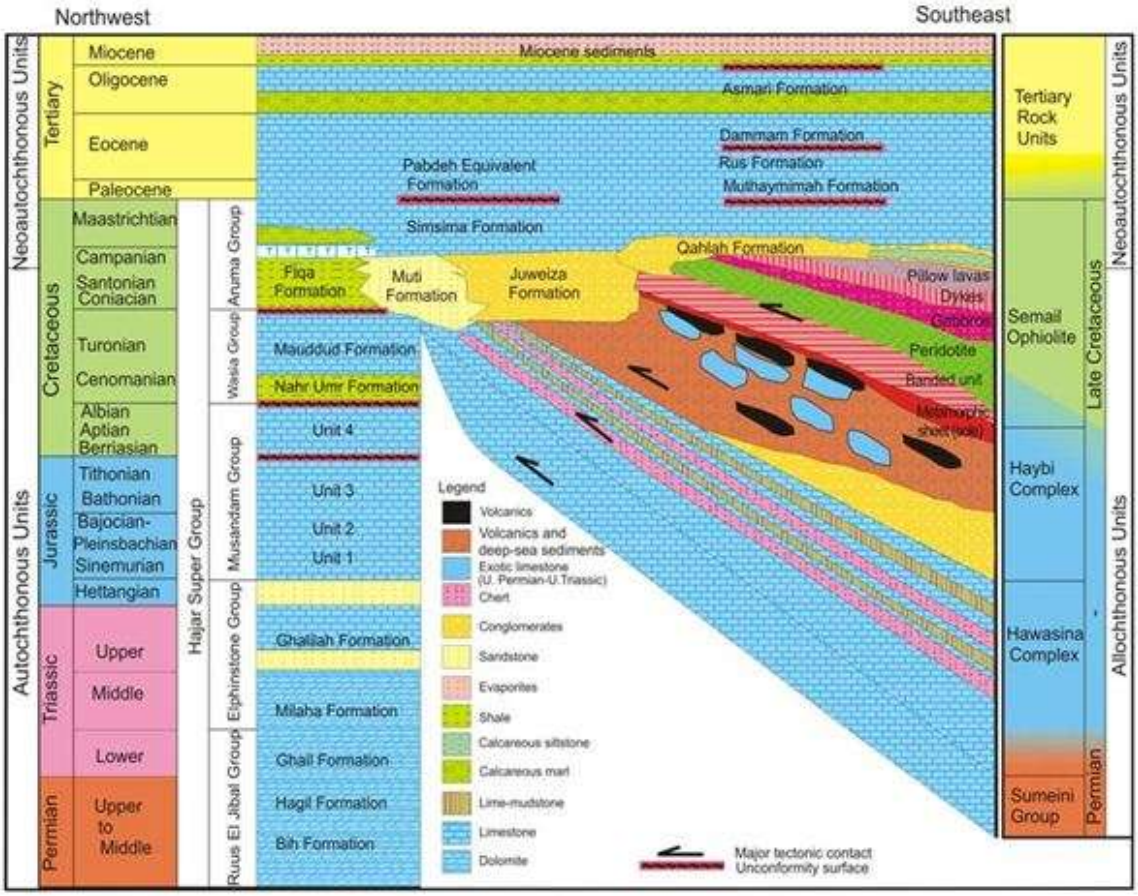

Figure 2.2. Lithostratigraphic chart of the Northern United Arab Emirates (UAE) modified from Abdelghany, (2003).

2.3. GEOMORPHOLOGIC SETTING OF THE NORTHERN UAE

The Northern UAE is divided into three main geomorphologic regions including the Hajar Mountains in the east, the gravel plain in the middle, and the desert plain in the west (Figure. 2.3). Due to the diversity of the geomorphologic features, the geomorphology of study area should be understood for better hydrological evaluation of the area.

Figure 2.3. Geomorpholic features map of the northern UAE modified from (Rizk and Garamoon, 2006).

2.3.1. Hajar Mountains. Lippard et al., (1982) divided the Hajar Mountains into two geological units based on their location with respect to the DFZ including:

1) Musandam peninsula to the north, locally called Ru'us Al Jibal (meaning head of the mountains) due to their heights that reach 2000 m which are the highest in the UAE. Geologically, the Ru'us Al Jibal is an exposure of a thick part of the sequence that covers Arabia and mainly consists of Mesozoic carbonate. 2) To the south of the DFZ the Semail

ophiolite outcrops and extends to the central part of the Sultanate of Oman. This portion is characterized by gentler slopes compared to the Ru'us Al Jibal. It is highly fractured at its surface and has a dense network of drainage patterns; hence the Hajar Mountains are considered the main recharge area that controls rain water distribution through the fractures and valleys in the UAE (Ministry of Agriculture and Fisheries, 1981).

2.3.2. Gravel Plain. The gravel plain of the UAE is divided by the Hajar Mountains into eastern and western gravel plain. The eastern gravel plain is located between the Hajar Mountains and the Gulf of Oman; it is narrow because of the close proximity of the mountains to the sea. Most of our present study area is located in the western gravel plain bounded by the Hajar Mountains to the east and the desert plain to the west. The western gravel plain extends from Ras Al Khaimah in the north to Al Madam area, and then it appears again in the Jaw area - Al Ain city to the south. The elevation of the gravel plain increases to the south where it reaches 350 m above sea level in Al Ain, 250 m above sea level in Al Madam area and at sea level in Ras Al Khaimah (Ministry of Agriculture and Fisheries, 1981); the width of the gravel plain increases towards the south.

The low relief of the gravel plain results from a series of coalescing alluvial fans and sediments deposited by recent or former river valleys from the Hajar Mountains (Al Farraj and Harvey, 2004). These fans and sediments are characterized by gravel ranging from boulder size at the foothills and fine gravel at the fringes of the desert plain. The gravel plain is dissected by valleys that extend from the Hajar Mountain catchment area and other small anticlines on the west of the gravel plain. The valleys start from the Hajar Mountains and extend to the south crossing the desert plain to the Arabian Gulf in the north, but they hardly reach the Arabian Gulf, once every ten years based on the rate of precipitation (Rizk and Garamoon, 2006). The gravel plain is bordered by a group of small surface anticlines (i.e. Faiyah and Hafit) to the west (Figure 2.3).

2.3.3. Desert Plain. In the UAE, the desert plain comprises sand dunes and inland sabkhas. Sand dunes cover most of the desert plain area that occupy 90% of the UAE area (Figure 2.3) (Al-Nuaimi et al., 2003). Sand dune heights range from 10-20 meters at the borders of the coast and gravel plain zones, where they reach a maximum of ~ 200 meters in the south of UAE; however in the study area, west of the Al Fayah anticlines,

the average height of the dunes reaches 50 meters (Ministry of Agriculture and Fisheries, 1982).

Sabkhas which are flat saline crust of clays, silts or sands occur in the interdune areas. They result from evaporation of the rain water or surface water that is raised from the subsurface by capillary action. Inland sabkhas are more widespread to the south of the UAE away from the study area (Glennie, 2001).

Unlike other geomorphologic features, most of the sand dunes migrate and change their positions within a period of one year except those that are fixed by a relatively dense cover of short shrubs and large dunes. Different types of sand dunes can be recognized in the UAE desert plain such as linear, transverse, barchans, barchanoid, and star dunes. The shape of the dunes is controlled by climatic factors, underlying sediments, and source of the sand (Embabi, 1991).

2.4. STRUCTURAL SETTING OF THE NORTHERN UAE

Understanding the structural geology of the DFZ and HFZ are important since these two fault zones are considered as the main structures controlling the hydrological setting of the northern UAE. Also, the structural geology beneath the anomaly area is discussed in order to provide an appropriate interpretation of the geophysical data.

2.4.1. Dibba Fault Zone (DFZ). The Dibba fault zone (DFZ) occurs in the north east of the UAE, separating the Musandam peninsula to the north and Oman Mountains (Semail Ophiolite) to the south. The DFZ is a window within the Hajar Mountains that extends from the town of Dibba on the Gulf of Oman to the Ithin area inland with a length of ~ 25 km and a width of 10 km (Lippard et al., 1982).

Tectonically, the NE-SW trending DFZ is interpreted by Robertson et al., (1990a) as a minor transform fault that developed during the opening of the Tethys Ocean. It is considered an extension of a major transform fault called “Oman or Dibba Line” that crosses the gulf of Oman and is associated with other major faults such as the Zendan Fault that bounds the Zagros Mountain to the east and Makran coast to the east, and extends further north into the south east of Iran (Lippard et al., 1982).

Normal faults occur between the DFZ and the Musandam units and are interpreted as hinged listric normal fault resulting from the Musandam uplift, with the

greater (500 m) amount of throw in the north-east than in the south-west (Searle, 1988). Also, normal faults aligned parallel to the DFZ have been characterized from offshore seismic data collected in the gulf of Oman east of the town of Dibba (Searle, 1983).

The sediments within the DFZ (Figure 2.4) reflect the emplacement of the Tethys Ocean floor onto the carbonate of the Hajar Super Group (Searle, 1983). These sediments consists of the Mayhah Formation that is part of Sumaini group carbonates, Hawasina complex which is presented by four formations that are Hamrat Duru Group, Dibba formation, Dhera formation and Shamal formation, Haybi complex, and Oman "Exotic" of Al Qamar Mountain (Glennie et al., 1974). Also units of metamorphic units that resulted from the subduction process have been found in DFZ such as metamorphic sheets, harzburgite slices and sub-ophiolite serpintinite (Searle, 1983). Previous geological investigations have characterized the DFZ within the mountains but the possible extension of this structure beneath the gravel and desert plain is still unclear.

2.4.2. Hatta Fault Zone (HFZ). The Hatta fault zone (HFZ) is located 60 km to the south of the DFZ. Both are controlled by the same tectonic event and have similar lithological units that resulted from ophiolite emplacement in the late Cretaceous. The HFZ trends NW-SE and extends from the Gulf of Oman to the Masfut area, a distance of 50 km inland and surrounded by ophiolite mountains (Nasir and Klemd, 1998).

Structurally, the HFZ is a transform or transitional fault system that was formed by right lateral faulting during the spreading of the Neo-Tethys Ocean (Robertson et al., 1990b). The Roudha anticline, a Tertiary fold trends in the same direction as the HFZ and is placed to the northwest of HFZ, suggesting that the Hatta transform fault zone has been reactivated (Nasir et al., 2003).

In the HFZ (Figure 2.5) the allochthonous complex comprises of platform slope carbonates belonging to the Sumeini group, sediments of the deep ocean related to Hawasina complex, units of Hamrat Duru that consists of turbiditic radiolarian cherts, calciturbidites, shale, and pillow lavas of Late to Early Jurassic-Early (Robertson et al., 1990b).

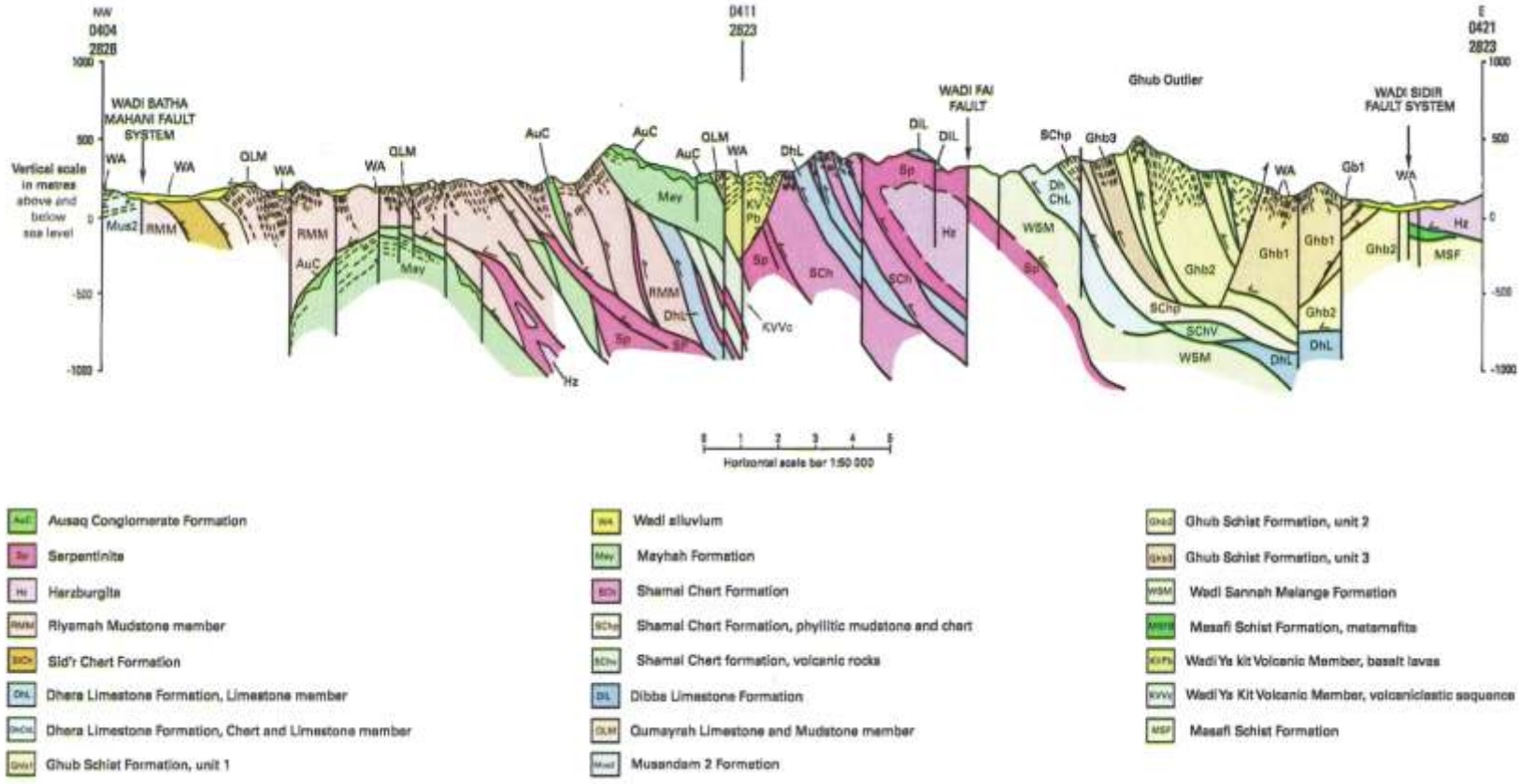

Figure 2.4. Cross section of the Dibba Fault Zone (DFZ) from Styles et al. (2006).

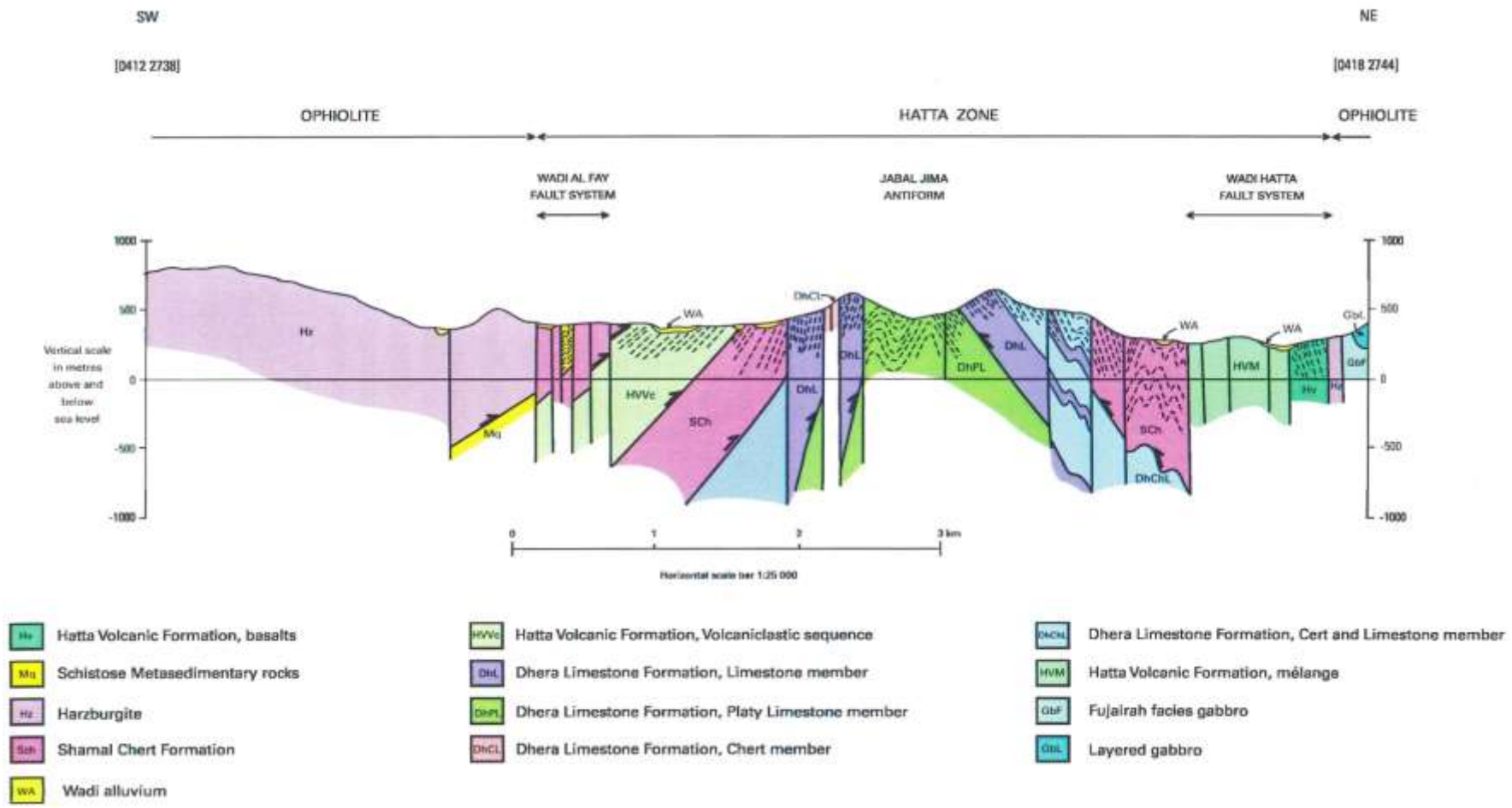

Figure 2.5. Cross section of the Hatta Fault Zone (HFZ) from Styles et al. (2006).

2.5. HYDROLOGICAL SETTING OF THE NORTHERN UAE

Surface and groundwater transport from recharge to discharge areas in the northern UAE, especially to the west of the Hajar Mountains is controlled by surface geomorphologic (Rizk & Al Sharhan, 2003) and major geological structures such as DFZ, HFZ and Ham zone (Rizk & Garamoon, 2006). Rizk and Al Sharhan (2003) classified the aquifer of the UAE into five types:

1. Limestone aquifer that is located in Ras Al Khaimah Emirate in the North.
2. Hafit aquifers in Al Ain City in the south.
3. The fractured ophiolite aquifers in the east resulting from the faulting of the ophiolite units.
4. Gravel aquifers that store most of the fresh water of the UAE and sand dunes aquifers of the south and west which cover the majority of the UAE area.
5. Sand dunes aquifers characterized by brackish water since it is located away from the recharge area.

The main source of ground water recharge is rainfall in the Hajar Mountains. Here the rainfall concentrates on the east and north of the country. The hydraulic head map (Figure 2.6) suggests that the mountains are the main ground water recharge area in the UAE (Rizk & Al Sharhan, 2003). Some of the rain infiltrates into the bedrock fractures, while the rest is channeled into wadis to the east and west of the mountains. The Eastern wadis discharge directly into the Gulf of Oman (Rizk & Garamoon, 2006). However, on the western side of the mountains, wadis barely reach the Gulf (once every ten years) due to the distance and the sand dunes that block the wadis from reaching the gulf (Glennie, 2001). Therefore, wadis lose their water by evaporation or infiltration to the gravel plain and desert plain aquifers.

Remote sensing studies by Ghoneim (2008) and geochemistry studies by Rizk & Garamoon (2006) suggest that lineaments and wadis trending parallel to the DFZ, HFZ and Ham fault zones channel the ground water from the recharge area in the Hajar Mountains to the western gravel and sand plain aquifers.

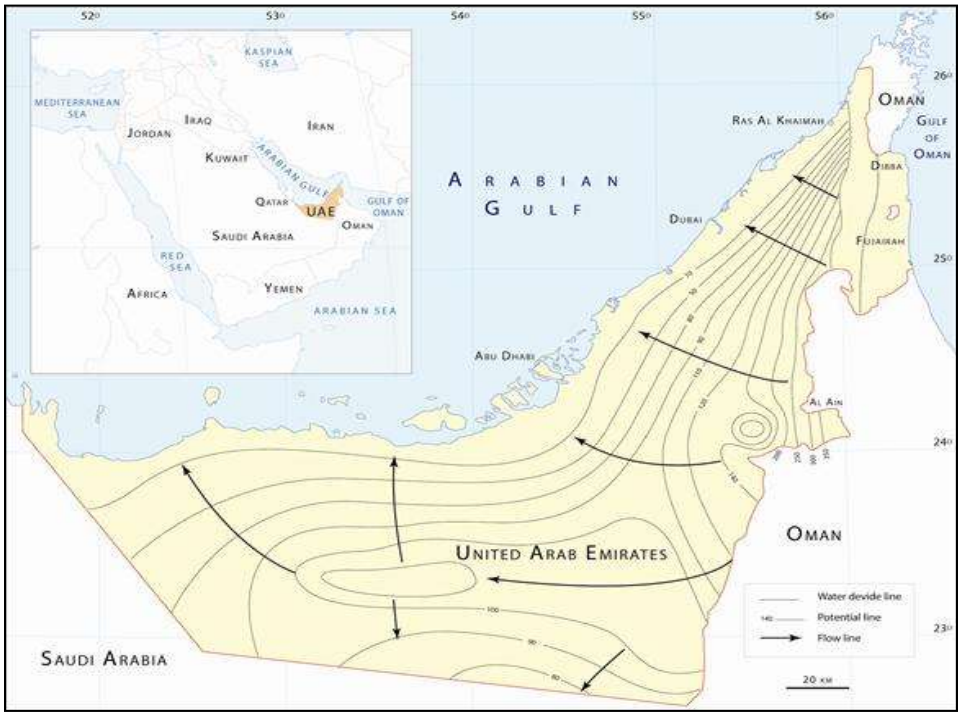

Figure 2.6. Hydraulic Head Map from Al Sharhan et al. (2001).

3. METHODS

3.1. INTRODUCTION

The magnetic and a hybrid magnetotulluric method were used to investigate three areas; the Dibba Fault Zone (DFZ), the Hatta Fault Zone (HFZ) and thermal anomaly areas. In this chapter a brief theory is presented for the geophysical techniques discussed. More extensive discussions can be found in the literature and many standard geophysics texts such us Telford et al., (1990), Grant and West (1965), Blakely (1995), Mickus (2000), Cagniard (1953), Vozoff (1972), Tikhonov (1950).

3.2. MAGNETIC METHOD

This method measures variations in the Earth's magnetic field resulting from subsurface rock magnetization or anthropogenic source variations. The strength of the Earth's magnetic field increases from ~ 25,000 nanoteslas (nT) at the magnetic equator to ~ 70,000 nT at the poles.

3.2.1. The Theory of the Magnetic Method. Coulomb's law describes the magnetic force F between two magnetic poles of strength $\boldsymbol{m_1}$ and $\boldsymbol{m_2}$ separated by a distance r as follows:

$$F = \frac{1}{\mu}\frac{m_1 m_2}{r^2} \qquad (3.1)$$

Where μ is the magnetic permeability of the medium and is unity in water and air.

Similar to the magnet, the earth has a magnetic field that consists of potential line of strength and two oppositely charged poles (north and south). The strength of a magnetic field (*H*) is a vector quantity that changes due to the distance from the magnetic pole represented by the following relation:

$$H = \frac{F}{m'} = \frac{m}{r^2} \qquad (3.2)$$

Where m' is unit magnetic pole, unit of the magnetic strength is NanoTesla (nT) in SI units, Oersted (Oe) and Gammas (γ) in cgs units.

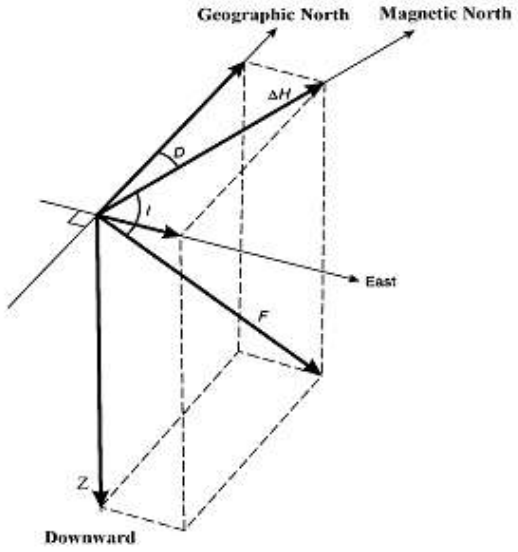

Figure 3.1. The magnetic field components (F is the direction of the main magnetic field, H is the Horizontal, I is the inclination and D is the Declination) modified from (Telford et al., 1990).

The primary physical property investigated with the magnetic method is the magnetic susceptibility (*k*), which is the ability of the materials (rocks) to be magnetized by an external magnetic field and is given as:

$$\mathbf{I} = k\mathbf{H} \qquad (3.3)$$

$$k\ (\text{cgs}) = 4\pi k\ (\text{SI}) \qquad (3.4)$$

I stand for the intensity of induced magnetization, *k* stands for proportionality constant (Magnetic Susceptibility). The magnetic susceptibility vary based on the magnetic minerals present; the rocks that rich magnetite such as mafic and ultramafic rocks are characterized by higher magnetic susceptibilities comparing to felsic rocks. The magnetic induction (**B**) is the sum of the external magnetic field (***H***) and the magnetic field produced by the magnetized materials (***H`***) where ***H`*** = 4π**I**

$$\mathbf{B} = \mu_0 (1 + k)\, \mathbf{H} \qquad (3.5)$$

Where, μ_0 is the magnetic permeability of free space ($4\pi \times 10^{-7}\ N.A^{-2}$). For any magnetic survey including this work, we measure total field strength magnetic intensity which consists of the main field, the external field, and the anomalous field.

The main magnetic field is produced in the core of the earth and results from convection currents in the outer core. The field varies relatively slowly with time (known as secular variations). Approximately 98% of the Earth's field is of internal origin. Seven magnetic field elements (Fig. 3.2) can be used to describe the main field of the earth and includes the field magnitude (F) which can be resolved into a vertical component vector (Z) and a horizontal component vector (H). The horizontal component can be resolved into a geographic north and a geographic east component. Other field elements include the magnetic inclination (I) which is the angle between a compass needle and a horizontal, magnetic declination (D), which is the angle between a compass needle and the true north (Figure 3.2).

The second component of the earth's magnetic field is the external magnetic field produced by electrical currents in the earth's ionosphere, consisting of particles ionized by solar radiation and put into motion by solar tidal force. This field varies rapidly with time and it is partly random (magnetic storms) and partly cyclical (diurnal variations). This accounts for ~2% of the Earth's magnetic field.

The anomalous field is the third magnetic component of the total field strength. The anomalous field is produced by ferrimagnectic minerals in the crust. This anomalous field is superimposed on the main geomagnetic field. The anomalous field is of primary

concern in exploration and results from variations in rock susceptibilities. This field is constant in time and place and results from variations in magnetic properties of crustal rocks and from anthropogenic sources.

3.2.2. Magnetic Data Acquisition. Since The DFZ and HFZ are observed within ophiolite sequences that are characterized by high magnetic susceptibility, the magnetic method can be successfully used to delineate fault zones provided the fault zones have a contrast in susceptibility with the surrounding unfaulted rocks. Typically, faulting enhances weathering resulting in lower susceptibilities of the rocks within the fault zones. Alternatively, movement of fluids within the fault zones can result in the alteration of mineral phases or the deposition of new minerals that are either more magnetic or less magnetic. Hence, magnetic surveys can be used to delineate fault zones (Telford et al., 1990).

The magnetic survey was divided into three grids: The DFZ grid area designed to delineate the possible extension of the DFZ underneath the gravel plain area was 41 km x 5 km; the HFZ grid area designed to delineate the possible extension of HFZ was 32.5 km x 5 km, and the thermal anomaly grid area designed to investigate and compare the geological structure beneath the anomaly area and the surrounding area, was 24 km x 8 km (Figure. 3.2). For the three grids, the magnetic data were acquired along lines at 500m spacing and the spacing between measuring points in each profile was 500m (Figures. A1, A2 & A3). A total of 901 points were measured over the DFZ grid, 715 points over HFZ, and 829 points over thermal anomalies area. The acquisition parameters of the magnetic surveys are summarized in Appendix A on tables A.1, A.2, and A.3.

The total field magnetic data were acquired using a Geometrics G-858 cesium vapor magnetometer with a sensitivity of 0.05 nanoTesla (nT). A handheld receiver global position system GPSMAP 60CSx by Garmin was used to define the survey area and to determine the position of the stations.

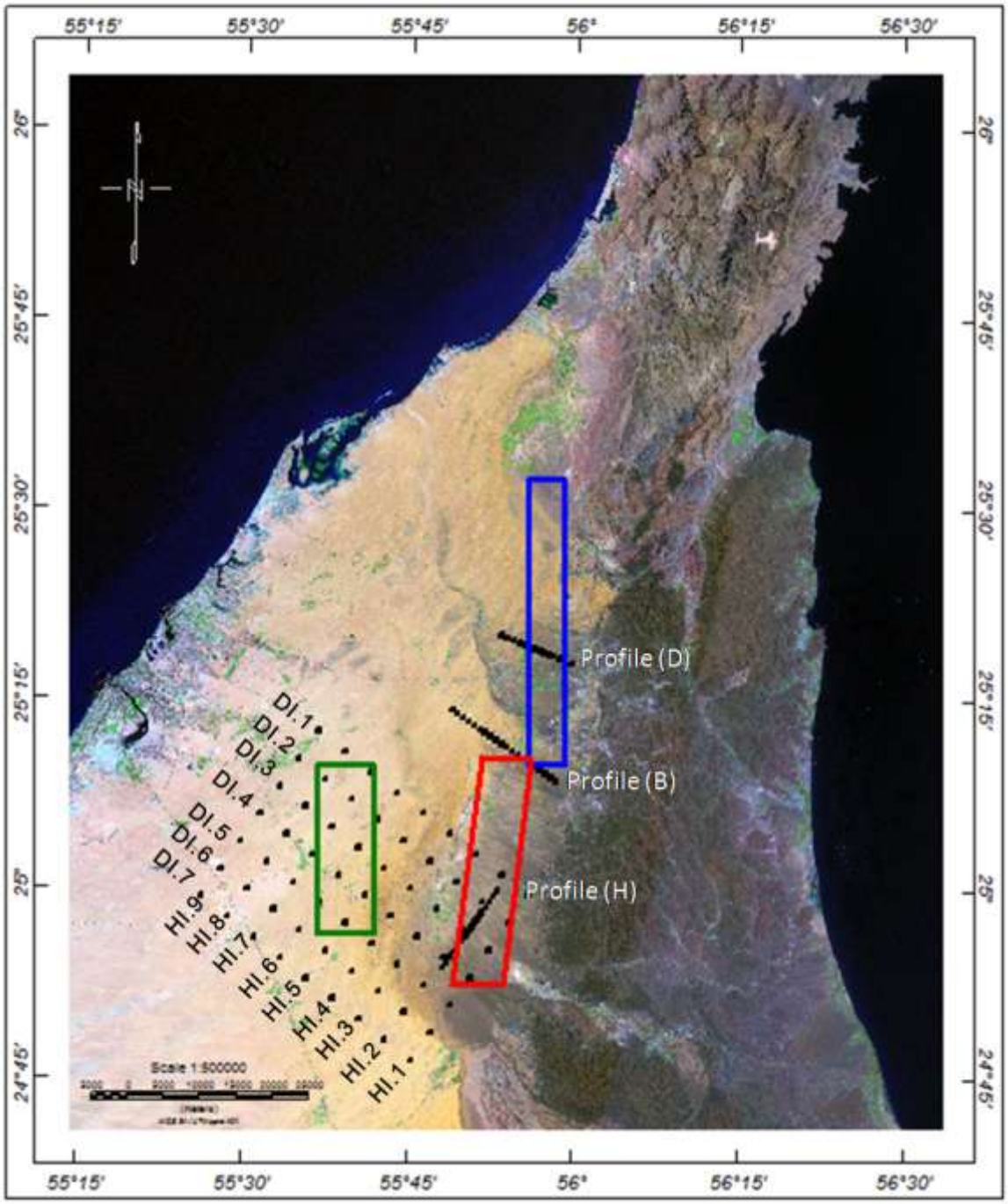

Figure 3.2. Satellite image of the northern United Arab Emirates showing the location of the magnetic surveys, Dibba grid area (Blue Rectangle), Hatta grid area (Red Rectangle) and Awir grid area (Green Rectangle). The rectangles represent magnetic data shown in figures 4.1A-C respectively, and the Audio Magnetotulluric AMT station locations are shown as black dots.

3.2.3. Corrections to Magnetic Data. The Earth's magnetic field is not constant but changes with time due to magnetic storms, diurnal changes, secular variation, reversals etc. Hence, magnetic survey data must be corrected to account for these variations.

3.2.3.1 Diurnal variation. Diurnal variations are smaller but more rapid oscillations in the earth's field which have periodicity of about a day and average amplitudes of 50 nT with maximum amplitudes of 200 nT (Mickus, 2000).
They are of two types: Quiet days (Q-days) and disturbed days (D-days). The quiet days are smooth, have low amplitudes and result from solar and lunar periodicities. In contrast, disturbed days are less regular and more erratic fluctuations associated with magnetic storms and have amplitudes of 100-1000 nT, caused by solar flares/sun spot activity. They can persist for several hours, even days. For most field surveys, diurnal variations (quiet day) are determined and corrected for, analogous to drift corrections in gravity surveys. On a disturbed day, field work should be halted. In magnetic surveys, repeated readings at a base station are often used to correct for diurnal variations.
Before the beginning of the survey the diurnal variation was determined by setting up a base station in the survey grid and recording for 24 hours every 30 minutes at point (366885E 2766001N) (Figure 3.3). The largest magnetic variation was 25 nT in the period of three and half hours and the normal magnetic field was 34510 nT. Based on this data, it was determined that a three hour interval was adequate for reoccupation the base station during data acquisition. A base station was setup for each surveying day. We measured the station at the beginning of the day and repeated the base station measurement every three hours based on the above test. On the next day, we measured the base station of day one at the beginning of the survey of day two and then we setup a new base station for day two which measured every three hours similarly to the first day. This procedure was repeated till the end of the survey. The data of each day was corrected to the base station then linked to the previous day.

3.2.3.2 Secular variations. Secular variations are slow and occur over long periods and can be ignored when conducting magnetic surveys over intervals of days or weeks, but must be taken into consideration if data is collected over a period of years or when compiling data from different years or decades. Secular variations show a westward

drift of certain features at a later epoch (Telford et al., 1990). Magnetic data can be corrected for secular variations using the International Geomagnetic Reference Field (IGRF) for the epoch in question.

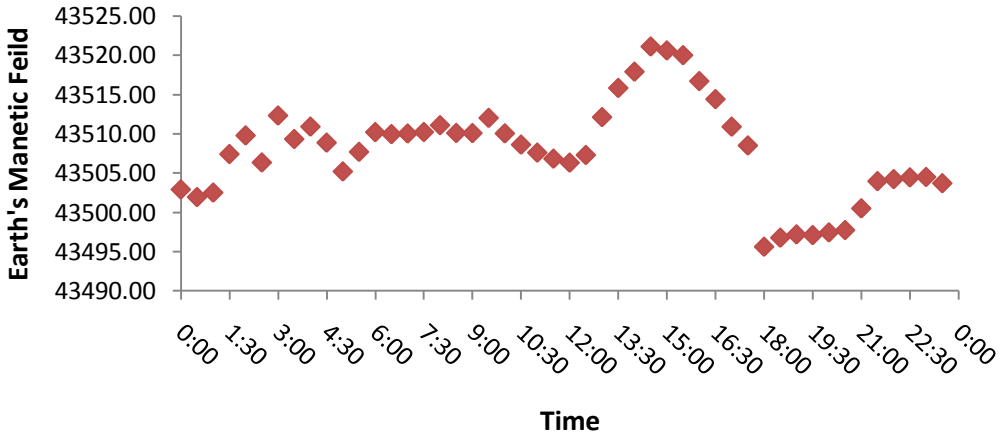

Figure 3.3. Diurnal variations at a readings base station for a twenty four-hour period

First developed in 1968, it is a mathematical representation of the earth's main magnetic field due to sources in the core and variations of the earth's field. Removal of this field from the data gives residual magnetic anomalies due solely to the geology. Removal of IGRF is applicable to surveys of large areas surveyed over long periods of time (several months to years). In smaller areas the removal of a regional trend is adequate. In this study, the IGRF was removed from the data and the results are presented as the residual magnetic anomalies.

3.2.4. Magnetic Data Processing. Magnetic anomalies are typically obscured by superposition of several anomaly sources from different depths and different sizes. This often makes the interpretation process more difficult and ambiguous. In order to interpret the sources of magnetic anomalies, it is often best to isolate anomalies from different sources. This can be achieved by the application of several mathematical filters that can enhance accentuate anomalies from target sources while attenuating anomalies from unwanted sources. Several different filtering techniques were applied to the magnetic data including upward continuation, Euler deconvolution, theta map etc. After correcting, the magnetic data from diurnal variation effect the data was imported into potential field mapping system –Oasis Montage.

3.2.4.1 Euler deconvolution. Thompson (1982) originally introduced the 3D Euler deconvolution technique for the magnetic profile data by applying Euler's homogeneity equation:

$$(x - x_0)\frac{\partial T}{\partial x} + (y - y_0)\frac{\partial T}{\partial x} + (z - z_0)\frac{\partial T}{\partial x} = N(B - T) \qquad (3.7)$$

(x_0, y_0, z_0) is the position of the magnetic source with total field T, which is identified at(x, y, z). B is a regional value of total magnetic field and N is the structural index. Reid et al (1990) developed this process to be applied to gridded data. This technique aims to determine the location and the depth to the top of the magnetic anomaly sources by utilizing first order x, y, and z derivatives. This technique can be applied for only some body types with known structural index such as sphere, cylinder, thin dike and contact (Nabighian et al, 2005). The shape of the body controls the structural index which is the rate of change in the potential field with distance (El Sadek, 2009). A 3D Euler deconvolution filter was also applied to the total field magnetic data in order to determine the depths to magnetic anomaly sources. A structural index of 1 (representing linear magnetic anomaly sources such as dikes or faults) was used for this purpose.

3.2.4.2 Theta maps. Wijns et al., (2005) introduced a new processing technique that delineates magnetic contacts. The "thetamap" is a processing technique derived from the analytic signal (introduced by Roest et al., 1992), that highlights magnetic contacts in a 2D total magnetic intensity (TMI) image. The method is ideally suited for data acquired

at low magnetic latitudes, where traditional reduction to the pole is not advisable (Wijns et al., 2005). The theta map detects edges independently of strike and amplitude and is thus most valuable at low magnetic latitudes where north-south-trending anomalies disappear in the TMI data. The angle theta is simply the horizontal derivative divided by the analytical signal as shown below (Wijns et al., 2005):

Table 3.1. Structural indices for geological structure. Modified from (www.intrepid-geophysics.com).

Value	SI Type	Shape of inferred geological structure
0.5	Step or plate edge	Step-like structures show a uniform increase or decrease in magnetic response that is similar across several traverse lines.
1	Line of dipoles	Fault/Dyke– Relatively thin sheet-like bodies that are near-vertical (wall-like)
2	Point pole	Vertical pipe– Near-vertical cylinder shaped structures.
3	Point dipole	Point source (nominally spherical)– Sources that are not continuous in any direction, normally irregular in shape but nominally spherical in mathematical models.

$$\cos(\theta) = \frac{\mathbf{A}.\hat{\mathbf{s}}}{|\mathbf{A}||\hat{\mathbf{s}}|} = \frac{\sqrt{(\partial M/\partial x)^2 + (\partial M/\partial y)^2}}{|\mathbf{A}|} \qquad (3.8)$$

Mathematically analytical signal is defined as:

$$\mathbf{A} = \frac{\partial M}{\partial x}\hat{\boldsymbol{x}} + \frac{\partial M}{\partial y}\hat{\boldsymbol{y}} + \boldsymbol{i}\frac{\partial M}{\partial z}\hat{\boldsymbol{z}} \qquad (3.9)$$

Where A is the analytic signal of magnetic intensity *M*, $\hat{\mathbf{s}}$ is a unit vector along the horizontal direction of the analytical signal, $\hat{x}, \hat{y}$ *and* $\hat{z}$ are unit vectors in a Cartesian coordinates system , $\boldsymbol{i} = \sqrt{-1}$, θ ranges from 0° to 90°. The theta map was created by dividing the map horizontal derivative map by the analytical signal using Oasis Montage system.

3.2.4.3 Continuation filtering. Simply, upward continuation filter (Robinson, 1970) smooths out near surface effects by calculating the potential field to higher elevation than that where the field is recorded. It is difficult to interpret the depth to the source due to the overlapping of high and low frequesncies, therefore the upward continuation filter is utlized to cut off these effects (Sharma, 1997; Nabighian et al., 2005) using the following equation:

$$F(x, y, -h) = \frac{h}{2\pi} \iint \frac{F(x,y,0)\partial x \partial y}{\{(x-x')^2+(y-y')^2+h^2\}^{1/2}} \qquad (3.6)$$

Where $F(x, y, -h)$ is total field at point $P(x', y', -h)$ (Telford et al., 1990). Therefore, an upward continued map approximates the regional magnetic field. This filter was applied to determine whether or not the anomalies were deep seated. Upward continuation at varying heights (100, 500, 1000, 1500 m) was applied to the magnetic data.

3.2.5. Two-Dimensional Forward Modeling. The interpretation of magnetic data requires the determination of subsurface geologic structures or models that represent the observed data. Typically, a set of models representing the subsurface geology is created and physical properties e.g., magnetic susceptibilities are assigned to the different layers or rock units. The magnetic anomalies from the different units are then calculated and matched to the observed data. This process is repeated until a good match is obtained between the observed data and the calculated anomaly. Magnetic models are non unique i.e., several models can produce the same response. Additionally, a perfect match may not necessarily produce realistic geologic models.

Hence, it is important to take into consideration the geology of the area and any other available data (e.g., well data or seismic data) in order to constrain the geologic models.

Several different algorithms can be used for the forward modeling of magnetic data (e.g., Talwani et al., 1959; Cordell and Henderson, 1968; Grant and West 1965). In the present study, the modeling software used utilizes a modeling algorithm of Talwani and Heirtzler (1964) to match the calculated model with the observed magnetic anomaly. This software requires input parameters such as magnetic inclination, magnetic declination, and magnetic susceptibilities that represent the different geological units in order to achieve the optimum model. Two-dimensional models were created using the GM-SYS software produced by the Northwest Geophysical Associates Inc (NGA)**.** The magnetic field elements used for the modeling include an inclination of 39° 3' and a magnetic declination of 1° 29'. The magnetic susceptibility values for each geological unit was obtained from the manual of GM-SYS since we used 0.000032 cgs for the sedentary rocks, 0.000349 cgs for the metamorphic units, and 0.002596 cgs for the igneous rocks. Two models were created in this project, the first is Model *A-A′* across the DFZ and *B-B′* across the HFZ (see Figure 4.1 A&B for locations). The models were constrained using well information obtained from the Ministry of Agriculture and Fisheries and from subsurface geological information obtained from the seismic cross sections and surficial geology based on the limited rock exposures.

3.3. MAGNETOTELLURIC METHOD

The magnetotelluric (MT) method is the study of the earth's natural time-varying electromagnetic fields. It studies naturally existing geomagnetic (magnetic) and electrical (telluric) fields that vary with time at the surface of the earth (Cagniard, 1953). The MT method is one of the geophysical electrical methods that measures the geoelectrical properties (resistivity) of the subsurface at depths ranges from a few meters to the mantle of the earth based on the frequency (Kaufman, 1981) due to the wide spectrum range of the magnetotelluric frequencies that is about 10^{4} to 10^{-6} Hz (Goldman, 2005). The factors that control or change the resistivity of the geological layers are the porosity, fluid

content, temperature and mineral content (Keller, 1989). The particular instrument used is a hybrid MT system.

3.3.1. The Source of the Audiomagnetotelluric Method (AMT). Vozoff (1972) states that there are two natural sources of the magnetotelluric waves: world wild thunderstorms and solar winds (Figure. 3.4). For the MT signals with frequency ranges above 1 Hz, the lightning discharges are the main source. The Earth receives around 100 lightning strokes per second (Zhang, 1997), which is enough to have continuous energy in any part of the world. This energy is trapped in the atmospheric waveguide between the ionosphere and the surface of the earth. These waves travel for long distances since the wavelength can reach the length of the Earth's circumference (i.e. Schumann resonance = 7.8 Hz) (Jiracek et al., 1995).

The second natural source, that provides electromagnetic signals (hydro-magnetic waves) with frequency below 1 Hz results from the interaction between the solar wind received from the sun and its magnetic field and Earth's magnetosphere. The processes that result from this interaction change the shape and the size of the magnetosphere and create electromagnetic fields that pass through the lower layers of the atmosphere to reach the surface of the earth (Jiracek et al., 1995).

Magnetotelluric (MT) data for this work was collected at the frequency range between 1 Hz to 10^5 Hz with a higher frequency range than the conventional MT range and within the reach of the audio frequency range, thus it is known as Audiomagnetotelluric (AMT) or Control Source Audiomagnetotelluric (CSAMT) since the signal of the natural electromagnetic sources at high frequency ranges (Audio Range) could be weak, therefore a controlled source (Man-Made Source) is utilized for shallow subsurface investigations (Zonge and Hughes, 1991).

3.3.2. The Theory of the Audiomagnetotelluric Method (AMT). AMT has the same theory of the MT method, both use the earth's electromagnetic (EM) fields. The electromagnetic fields are described by Maxwell's equations in differential form (Zonge and Hughes, 1991):

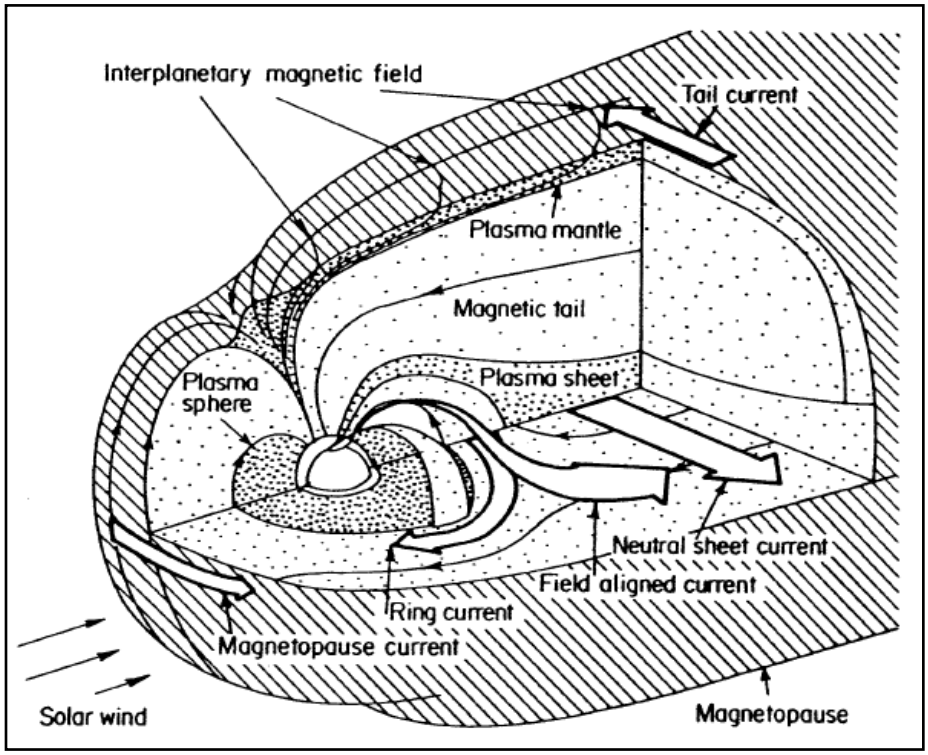

Figure 3.4. Major component of magnetospheric current system (from Potemra, 1984)

$$\nabla \times \mathbf{E} = -\frac{\partial \mathbf{B}}{\partial t} \quad \textit{(Faraday's Law)} \qquad \textit{(3.10.1)}$$

$$\nabla \times \mathbf{H} = \mathbf{J} + \frac{\partial \mathbf{D}}{\partial t} \textit{ (Ampere's Law)} \qquad \textit{(3.10.2)}$$

$$\nabla \cdot \mathbf{D} = q_v \quad \textit{(Coulomb's Law)} \qquad \textit{(3.10.3)}$$

$$\nabla \cdot \mathbf{B} = 0 \ \textit{(Continuous flux Law)} \qquad \textit{(3.10.4)}$$

The fundamental electromagnetic units are expressed in System International (SI) form:

E Electrical field intensity (V/m)

D Electrical flux density (C/m^2)

H Magnetic field intensity (A/m)

B Magnetic flux density (Wb/m^2)

J Electrical current density (A/m^2)

$\boldsymbol{\varepsilon}$ Electrical permittivity (Farads per meter)

$\boldsymbol{\mu}$ Magnetic permeability (Henrys per meter)

$\boldsymbol{q_v}$ Electrical charge density (C)

$\boldsymbol{\sigma}$ Medium's conductivity (Siemens)

$\boldsymbol{\rho}$ Resistivity (Ohm.m)

These quantities are related to each other by the following constitutive relationships that are valid for a homogenous earth or media.

$$\mathbf{B} = \mu\,\mathbf{H} \qquad (3.11.1)$$

$$\mathbf{D} = \varepsilon\mathbf{E} \qquad (3.11.2)$$

$$\mathbf{J} = \sigma\mathbf{E} \text{ (Ohm's law)} \qquad (3.11.3)$$

$$\sigma = 1/\rho \qquad (3.12)$$

By taking the curl of equation *(3.10.1)* and substituting equation *(3.10.2)* yields EM wave equations:

$$\nabla^2\mathbf{E} = \mu\left(\sigma\frac{\partial \mathbf{E}}{\partial t} + \varepsilon\frac{\partial^2 \mathbf{E}}{\partial t^2}\right) \qquad (3.13.1)$$

$$\nabla^2\mathbf{H} = \mu\left(\sigma\frac{\partial \mathbf{H}}{\partial t} + \varepsilon\frac{\partial^2 \mathbf{H}}{\partial t^2}\right) \qquad (3.13.2)$$

In most electromagnetic geophysical studies, the physical quantities ε, μ *and* σ reflect the electromagnetic properties of a material. The magnetic permeability μ can be considered to have its free space value (μ_0), the permittivity term (ε) in equation *(3.13.1)* and *(3.13.2)* can be ignored. Application of Fourier transform changes the electrical field (**E**) intensity and magnetic field intensity (**H)** from function of time to function of frequency. Equivalent to the wave equations, Helmholtz equations *(3.14.1)* & *(3.14.2)* result from applying this transformation to the wave equations (Jiracek et al., 1995):

$$(\nabla^2 + k^2)\,\mathbf{E}\,(x, y, z, \omega) = 0 \qquad (3.14.1)$$

$$(\nabla^2 + k^2)\,\mathbf{H}\,(x, y, z, \omega) = 0 \qquad (3.14.2)$$

(**E**) and (**H**) are now functions of the angular frequency (ω) which equals $2\pi f$ where *f* is frequency in Hertz and *k* is the propagation constant based on the medium and expressed as:

$$k = \omega\left[\left(\varepsilon - i\frac{\sigma}{\omega}\right)\mu\right]^{\frac{1}{2}} \qquad (3.15)$$

Since the MT method depends on the nature of the electromagnetic sources and the geoelectrical properties of the subsurface, two assumptions should be considered:

Quasistatic approximation:

The first assumption is that electrical displacement currents are neglected compared to electrical conduction currents ($\sigma \gg \omega\varepsilon$**)** at the MT frequency range which simply means that the earth is considered as a good conductor. Using this assumption named the Quasistatic approximation, the wave equations *(3.13.1) and (3.13.2)* becomes the diffusion equations as the following:

$$\nabla^2\mathbf{E} = \mu\sigma\frac{\partial \mathbf{E}}{\partial t} \qquad (3.16.1)$$

$$\nabla^2\mathbf{H} = \mu\sigma\frac{\partial \mathbf{H}}{\partial t} \qquad (3.16.2)$$

and the propagation constant can be written the the follows:

$$K = (-i\sigma\mu\omega)^{\frac{1}{2}} = (\sigma\mu\omega)^{\frac{1}{2}} e^{-i\frac{\pi}{4}} \qquad (3.17)$$

In other word, the electromagnetic field propagation within the subsurface is considered as a diffusive process that helps find Earth's conductivity response caused by ionic fluids such as saline water and magma (Jiracek et al., 1995).

Normally incident plane wave approximation:

Tikhonov (1950) and Cagniard (1953) assume the electromagnetic field as a wave incident toward the Earth's surface. In MT measurements, it has been assumed that the earth is a good conductor (Quasistatic approximation**)**; therefore the source waves are considered to be scattered and normally in the z-direction upon the Earth's surface, that is the second assumption (Jiracek et al., 1995). Electrical fields (E) and magnetic fields (H) of the plane perpendicular to the vertical propagation direction have constant magnitude and direction in case of normal refracted wave assumption in homogenous media, therefore the Helmholtz equation can be expressed in differential equation form as follows:

$$E_X(z) = E_0 e^{\mp ikz} \qquad (3.18.1)$$

$$H_Y(z) = H_0 e^{\mp ikz} \qquad (3.18.2)$$

Where E_0 and H_0 are the magnitudes of the electrical and magnetic fields at $z = 0$, minus sign is an indication of the fields reduction by traveling in $+z$ direction. The skin depth (***δ***) which provides an approximate estimate of the depth of investigation, can be recognized where the E_0 and H_0 strength reduce exponentially to 37% or 1/e of their strength at the surface (Jiracek et al., 1995).

$$\delta = \sqrt{\frac{2}{\sigma\omega\mu}} \qquad (3.19)$$

$$\delta \approx 0.5\sqrt{\rho T}\ \ [\text{km}] \qquad (3.20)$$

Where ρ is the resistivity and T is the period of the incident field.

The MT method aims to determine the resistivity (reciprocal of conductivity) of the subsurface at the measurement point, therefore the tensor impedance should be known to calculate the resistivity. Tensor impedance (Z) is the ratio of the electrical (**E**) and magnetic field (**H**) components as a function of frequency. The characteristic impedance can be expressed using E_X equation (*3.18.1*), curl of E of Maxwell's equation (*3.10.1*) and the exp ($i\omega t$) as follows:

$$Z(\omega) = \frac{\mathbf{E}(\omega)}{\mathbf{H}(\omega)} = \frac{\omega\mu_o}{k} \qquad (3.21)$$

or

$$Z_S = \frac{Ex}{Hy} \qquad (3.22)$$

At the surface where z =0, $\mathbf{E}(\omega) = Ex$ and $\mathbf{H}(\omega) = Hy$ at homogeneous half space. Surface impedance (Z_S) can be rewritten using equations (*3.17*) and (*3.21*) as follows:

$$Z_S = (\omega\mu_\circ\rho)^{\frac{1}{2}}\, e^{i\frac{\pi}{4}} \qquad (3.23)$$

From equation (3.23), the apparent resistivity of an inhomogeneous earth can be determined as shown in equation (3.24) which demonstrates the proportional relationship between surface impedance and the square root of the resistivity.

$$\rho_a = \frac{1}{\omega\mu_\circ}|Z_s|^2 \qquad (3.24)$$

Tensor impedance can be expressed in different forms based on the Earth's dimensionality, where in 3-D it can be written as linear equation in matrix form:

$$\begin{pmatrix} E_x \\ E_y \end{pmatrix} = \begin{pmatrix} Z_{xx} & Z_{xy} \\ Z_{yx} & Z_{yy} \end{pmatrix} \begin{pmatrix} H_x \\ H_y \end{pmatrix} \quad (3.25)$$

In 2-D earth the diagonal elements disappear ($Z_{xx} = 0$, $Z_{yy} = 0$ and $Z_{xy} \neq Z_{yx}$), when the geoelectrical strike is along x or y direction. As a result of this, equation (3.25) changes to

$$Z = \begin{pmatrix} Z_{xx} & Z_{xy} \\ Z_{yx} & Z_{yy} \end{pmatrix} \quad (3.26)$$

$$Z_{xy} = \frac{Ex}{Hy} \quad (3.27)$$

$$Z_{yx} = \frac{Ey}{Hx} \quad (3.28)$$

Since $\frac{1}{\omega\mu_\circ} = \frac{1}{f}$ where f is the frequency the equation 3.26 became:

$$\rho_a = \frac{1}{f} |Z_s|^2 \quad (3.29)$$

We can calculate apparent resistivity as a function of frequency in two directions:

$$\rho_{xy} = \frac{1}{f} |Z_{xy}|^2 = \frac{1}{f} \left|\frac{Ex}{Hy}\right|^2 \quad (3.30)$$

$$\rho_{yx} = \frac{1}{f} |Z_{yx}|^2 = \frac{1}{f} \left|\frac{Ey}{Hx}\right|^2 \quad (3.31)$$

The off-diagonal elements are decoupled into two polarization modes TE (Z_{xy}) and TM (Z_{yx}). TE is refers to the transverse electric mode that measures electrical field parallel to geoelectrical strike and TM represents the transverse magnetic mode that measures magnetic field parallel to geoelectrical strike. This decoupling is valid only for electromagnetic fields as plane waves where the electrical and magnetic fields are perpendicular to each other. In 1-D earth, Z elements related to each other by $Z_{xy} = -Z_{yx}$ (Jiracek et al., 1995).

3.3.3. Audiomagnetotelluric Method (AMT) Data Acquisition.

3.3.3.1 Survey design. The aim of the AMT survey was to characterize the structure beneath the anomaly area and verify the results of the magnetic survey within the gravel plain. AMT data were collected along profiles positioned perpendicular to the DFZ and HFZ trends and over a 3-D survey grid covering the anomaly area. The acquired AMT data have been divided into three groups based on the target of the survey. Profiles D, B and DI.1- DI.7 (Figure 3.2) were designed to characterize the extension of the DFZ. Profile D (19 stations) (NW-SE) is located in the mountain flank within the gravel plain close to the fault exposure in northern Hajar Mountains. Profile B (21 stations) (NW-SE) extends from the gravel plain to the desert plain covering the area between DFZ exposure and the anomaly area. Profiles (DI.1-DI.7) (NW-SE) consists of 63 stations with a spacing of 5 km over the anomaly area. The main purpose of these profiles was to characterize the structures beneath the anomaly area and at the same time delineate the possible extension of the DFZ. Stations used in DI profiles were reoriented to design the profiles HA.1- HA.9 profiles (NE-SW) HA profiles were oriented perpendicular to the HFZ to characterize it. Profile H (21 stations) (NE-SW) was designed to investigate the extension of HFZ within the anomaly area but with a higher resolution (closer spacing 500-1000 km). Acquisition parameters and more detailed information of the AMT data acquisition are available in Appendix A.

3.3.3.2 Instrumentation. A Geometrics Stratagem EH4 was used for data acquisition. This is a hybrid MT system as it records passive and active electromagnetic sources that range in frequency from 10-92,000 Hz (Geometrics, 2000). The EH4 system is called a “Hybrid system” because it records signals from natural sources at the low frequencies (10-1,000 Hz). At higher frequencies (750-92,000 Hz) the transmitter is used to enhance the weak natural signals. This system is comprised of a transmitter and a receiver. The transmitter contains two horizontal-magnetic dipoles that transmit signals in the high frequency band (around 1,000-70,000 Hz) where natural signals are weak. The receiver consists of two perpendicular lines that measure that electrical field, using metal electrodes placed into the ground and two highly sensitive magnetic coils to measure the magnetic field. These magnetometers are leveled and oriented perpendicular to each other as the same direction of the electrical receivers (Figure 3.5). All the AMT stations in this

study are orientated north-south and east-west since (Figure3.5) is always placed in the north direction. Typically the x-direction is parallel to the survey direction (perpendicular to the geological strike while the y-direction is parallel to the geologic strike (strike of structure)). The distance from the transmitter to receiver was calculated

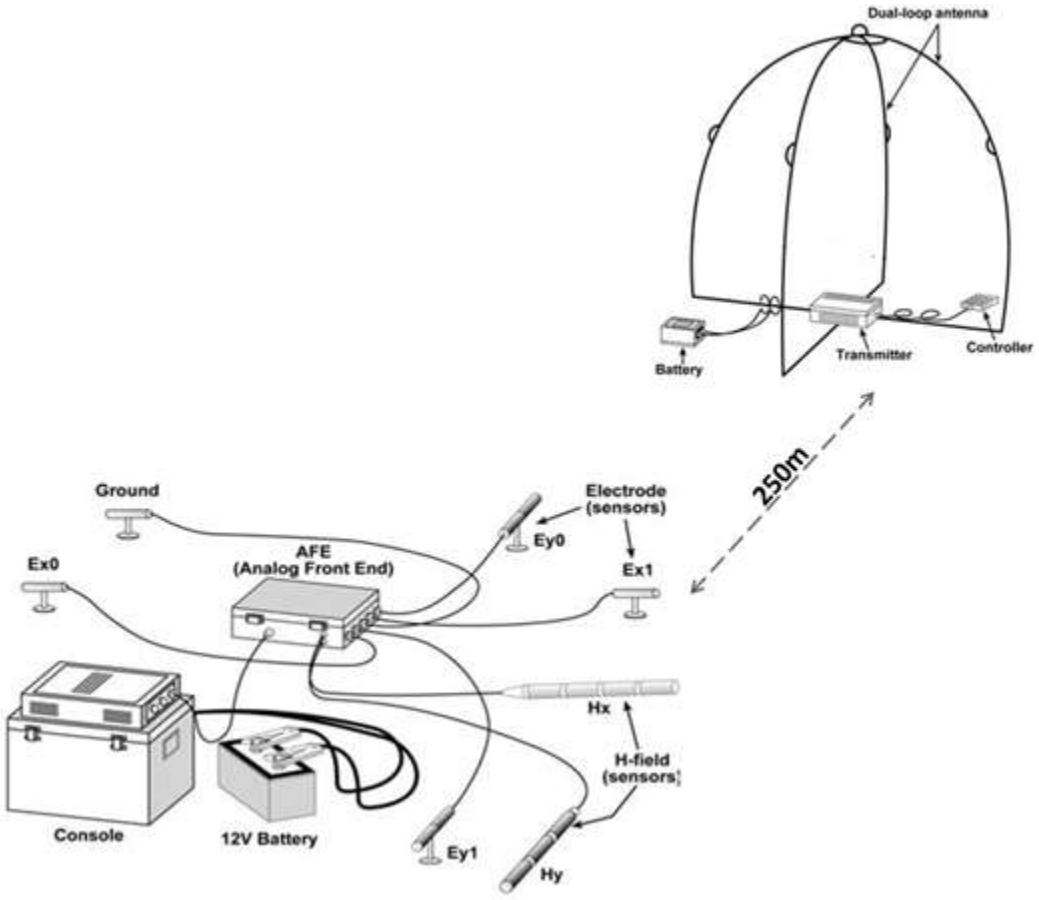

Figure 3.5. Audiomagnetotelluric (AMT) survey layout (figure modified from Geometrics, 2000)

using the skin depth equation (3.18) to ensure that it fulfills the plane wave assumption and provides sufficient signal. The data were recorded in three bands with ranges (10-

1,000 Hz), (400- 3,000 Hz) and (750-92,000 Hz). The recording at each frequency band was stacked 14 times to improve the signal to noise ratio.

3.3.4. Audiomagnetotelluric Method (AMT) Data Processing.

3.3.4.1 Field data. Downloaded data from Stratagem EH4 is divided into three files for each measuring station. X, Y and Z files, where X-files has the calculated crosspower spectra from corresponding time-series file which is obtained from Y-files that contain raw time-series data; and Z-files contain the impedance data from which the apparent resistivity and 1-dimensional resistivity soundings are calculated.

3.3.4.2 Apparent resistivity maps. The apparent resistivities of selected frequencies at all AMT stations of the thermal anomaly grid area were selected from the impedance tensor (from Z-files). These apparent resistivity values for each frequency were gridded to produce resistivity maps at different frequencies (or depth levels). This is analogous to providing the resistivity at different horizontal depth slices.
This step produces tens maps of apparent resistivity for each TE and TM mode ranging from 40 to 50,100 Hz. At this project we pick maps at three frequencies to present the whole data. The first is 200 Hz representing the deepest level, 5,010 Hz for middle depths and 50,100 Hz shallowest depth.

3.3.4.3 Data importing and conversion. The AMT field data were imported to the WinGLink processing package developed by Geosystm Inc. The data was converted to EDI format which can be identified by WinGLink. The data of each station was been named and located by providing UTM coordinates.

3.3.4.4 Sounding curves. Sounding curves are presented as plots of the log of the apparent resistivity (ρa) and the phase versus the log of the period of each station. Impedance tensors calculated from the measured electrical and magnetic field at the site were used to produce the transverse electrical (TE mode), transverse magnetic (TM mode), apparent resistivity (ρa), and phase of TE and TM modes. The data quality can be improved by editing the data displayed in sounding curves. Typically, AMT data is noisy, therefore we mask bad points, smooth the resistivity curves and move the shifted points to the smoothed curve. Shifted curves have been corrected using static shift process. At

this step, we examine the data by shifting TE (xy) curve to be equivalent to the TM (yx) curve or the reverse (Figure 3.6), then we chose the option that provide the optimum result (Figure 3.6).

3.3.5. Two-Dimentional Inversion. The 2D inversion was performed on the AMT profiles using the WinGLink software package that utilizes Rodi and Mackie (2001) algorithm code. The inversion has been applied on TE mode data, TM mode and both. The disadvantage of this code is that it uses both apparent resistivity and phase data to apply the inversion. Several stations had bad phase data while the resistivity data were perfect at this station. Due to this limitation some stations were deleted from the thermal anomaly area.

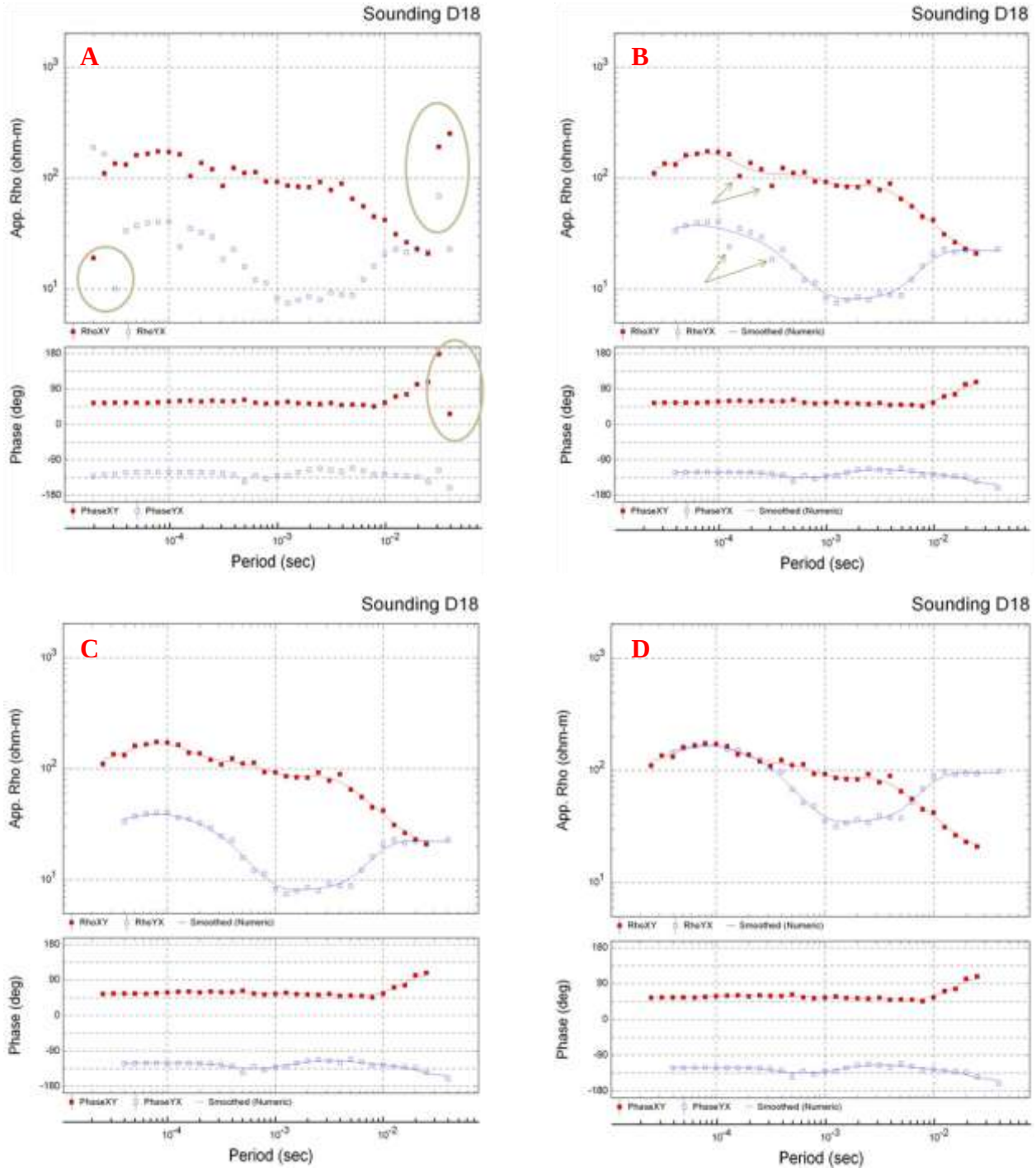

Figure 3.6. Example of processing steps used to clean and correct sounding curves. (Station D18). A) Masking bad points (Circles), B) Smoothing the curves and correcting shifted points (Arrows) to the smoothed curve, C) Figure shows the affect of static shift that been solve in D.

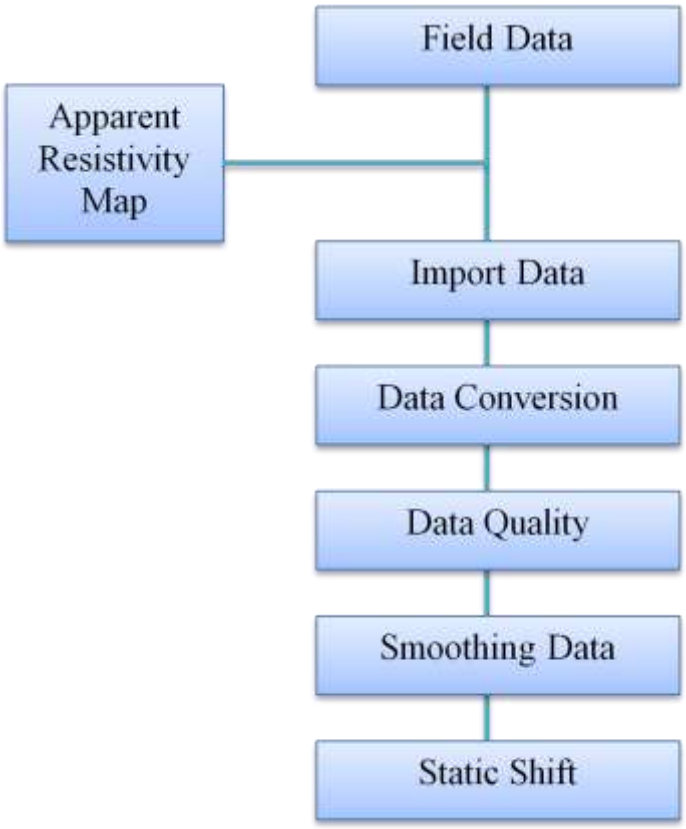

Figure 3.7. Flow chart shows the processing steps that were applied to the AMT data.

4. RESUTLS

This chapter presents the results of the geophysical investigations discussed in the previous chapter (Chapter 3). The objective of the geophysical surveys was to map the possible extension of the DFZ and HFZ into the thermal anomaly area. These faults are exposed west of the Hajar Mountains.

4.1. MAGNETIC INVESTIGATIONS

As previously discussed in section 3.2.1 the magnetic data were acquired along three grids within the gravel plain area where the surface topography does not show any expression of faulting.

4.1.1. Total Field Magnetic Data. The gridded total field magnetic data from the Dibba grid area is shown on Figure 4.1A. In general the total field magnetic anomaly values are higher (magenta) in the north and decrease to the south (light green to blue). A pronounced, linear, low magnetic anomaly is observed trending NE-SW. This magnetic anomaly appears to form the boundary between the higher (>43,700 nT) magnetic anomaly values in the north from the lower magnetic anomaly values (<43560 nT) in the south. This magnetic anomaly is ~5.0 – 7.0 km wide (Figure 4.1A). Two ambiguous linear magnetic anomalies trending NW-SE parallel to each other, have been observed to the south of the first anomaly with similar magnetic values.

The magnetic data from the Hatta grid area is shown on Figure 4.1B. As was observed for the Dibba grid, the magnetic anomaly values are higher in the north and decrease to the south. A WNW-ESE linear low magnetic anomaly is observed with magnetization values ~200 nT lower than the surrounding areas. This magnetic anomaly is located in the southern part of the grid, crossing the entire survey area from the W to E with a width of ~ 7 - 10 km (Figure 4.1B). The anomaly widens to the east. Again, this linear magnetic anomaly appears to form the boundary between higher magnetization values in the north and lower values to the south.

Further to the west within the desert plain area, the magnetic data acquired over the thermal anomaly area (Awir area (Green Rectangle Figure 3.2)) does not show any anomalous areas associated with faulting. Instead, the data (Fig. 4.1C) shows decreasing

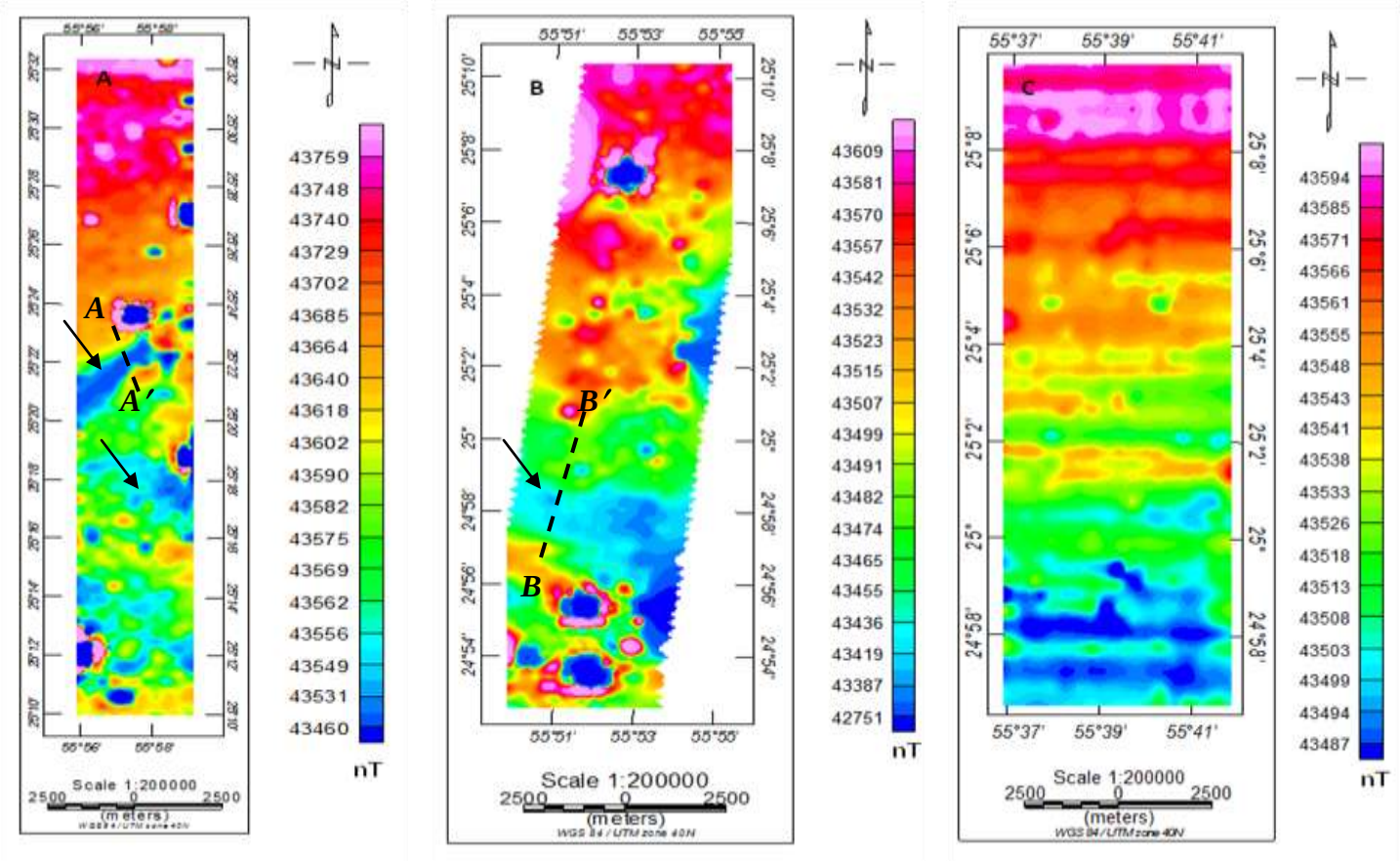

Figure 4.1. A) Total field magnetic anomaly map of the Dibba grid area. B) The total field magnetic anomaly map of the Hatta grid area. C) The total field magnetic anomaly map of the Al Awir area (see figures 3.2 A, B, and C for locations). Black arrows show the location of the magnetic anomalies, and profiles *A-A′* and *B-B′* are shown in figures 4.9 and 4.10.

total field magnetic values from north to south. These results are consistent with recent aeromagnetic data acquired in this part of the UAE (Styles et al., 2006) that did not detect any magnetic anomalies but showed a similar decrease in the total field magnetic intensity to the south (Figure 4.1C).

Additionally, the total field magnetic maps show some circular magnetic anomalies. These anomalies are characterized by an inner zone of low magnetic values surrounded by an outer zone of high magnetic values as shown on Figure. 4.2. The diameter of these rings ranges from ~1-2 km.

All the results described above are obtained from the raw data that were corrected from diurnal variation effect only (Figures 4.1). The same results were repeated when we corrected for secular variations using the International Geomagnetic Reference Field (IGRF) (Figures 4.3A, 4.4A and 4.5A), except the map of Awir area which changed without detecting any anomalies (Figure 4.5A).

4.1.2. Euler Deconvolution. A 3D Euler deconvolution filter (Reid et al., 1990) was also applied to the total field magnetic data in order to determine the depths to magnetic anomaly sources. A structural index of 1 (representing linear magnetic anomaly sources such as dikes or faults) was used for this purpose. The results of the Euler deconvolution solution (Figure 4.3B) show a clustering of solutions coincident with the low magnetic anomaly observed on Figures 4.1A and 4.3A from the Dibba grid area. These solutions have an average depth of 600 m trending NE-SW.

3D Euler deconvolution solutions from the Hatta grid area using the same parameters as for the Dibba grid area shows three distinct clusters of solutions coincident with the low magnetic anomaly observed on (Figures 4.4A and 4.4B). One set of clusters occurs within the anomaly, the second set occurs at the southern edge of the anomaly and the third occurs at the northern boundary of the anomaly (Figure 4.4B). The average value of the depth associated with this low magnetic anomaly is 600 m.

The solutions for the circular anomalies of both the Dibba and Hatta areas have an average depth of 200 m (Figures 4.4B and 4.4B).

4.1.3. Theta Maps. The application of the Theta technique (Wijns et al., 2005) on the magnetic data confirms the occurrence of the detected linear anomalies in Dibba and Hatta areas (Figures 4.3C and 4.4C). The fault anomalies are narrower on the Theta maps. Also the circular anomalies appear smaller on the Theta maps.

4.1.4. Upward Continuation. The upward continuation filter (Robinson, 1970) was applied to the magnetic data to determine whether or not the magnetic sources associated with the mapped anomalies are deep seated. The upward continuation results from the Dibba grid area (Figure 4.6 A-D) suggest that the linear anomaly shown in Figure 4.3 A persists in the upward continued data to a height of 500 m (Figures. 4.6 A and B). However, the anomaly is not present on the upward continued data at a height of 1000 m (Figures. 4.6 C).

The upward continued data from the Hatta grid area (Fig. 4.7 A and B) suggest that the linear anomaly observed on the total field magnetic data (Fig. 4.4 A) is readily seen on the 100 and 500 m (Fig. 4.7 A and B) upward continued data but is not present on the 1000 m upward continued data (Fig. 4.7 C). The upward continued maps accentuate the boundary between the higher magnetic values to the north and the lower magnetic values to the south.

The upward continued data of the Awir area (Figure 4.8) did not show any anomalies similar to the raw magnetic map. The high magnetic ring surrounding the low magnetic zones in the circular anomalies are attenuated on the upward continued maps (Figures 4.6 and 4.7).

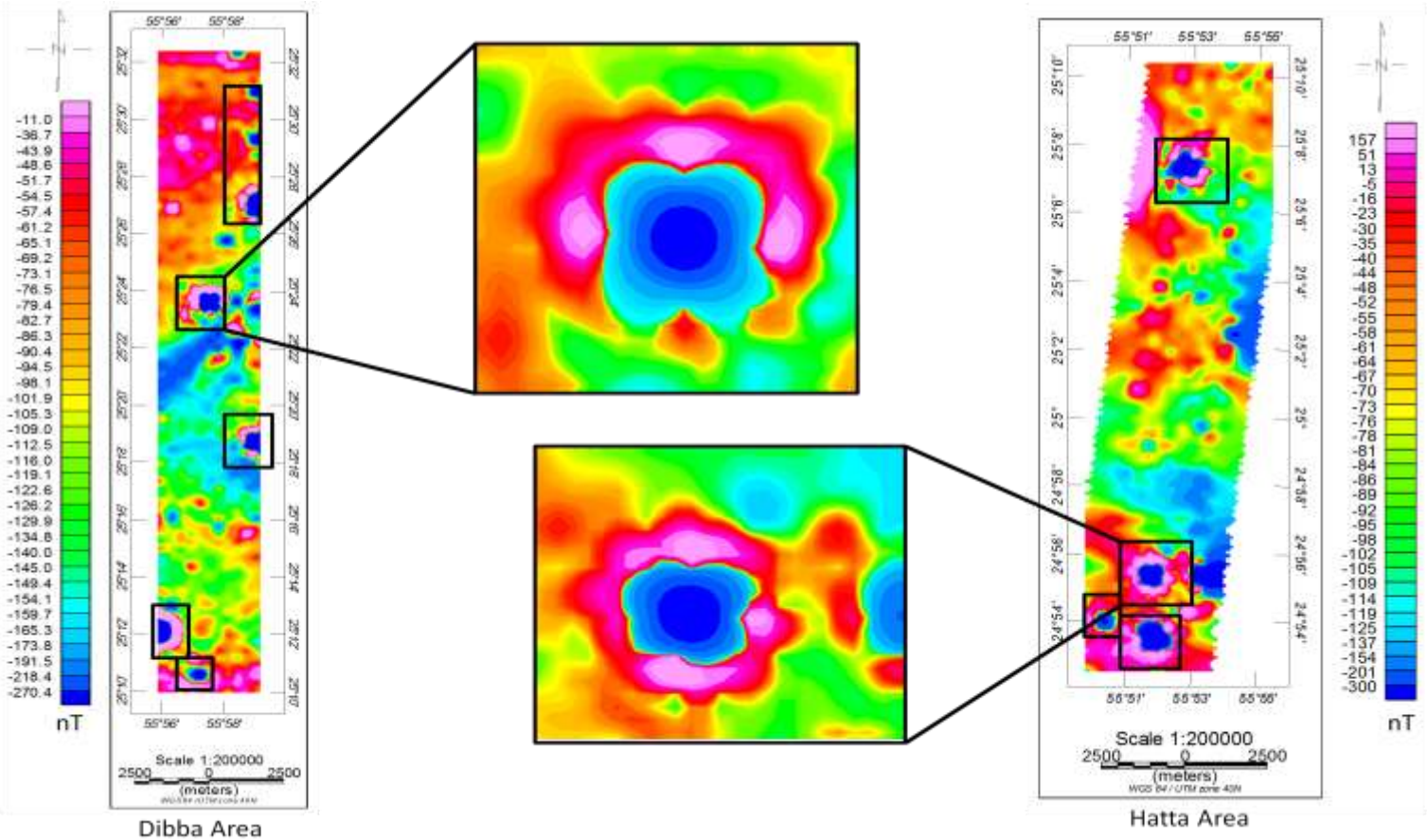

Figure 4.2. Image illustrating circular (ring shape) magnetic anomalies

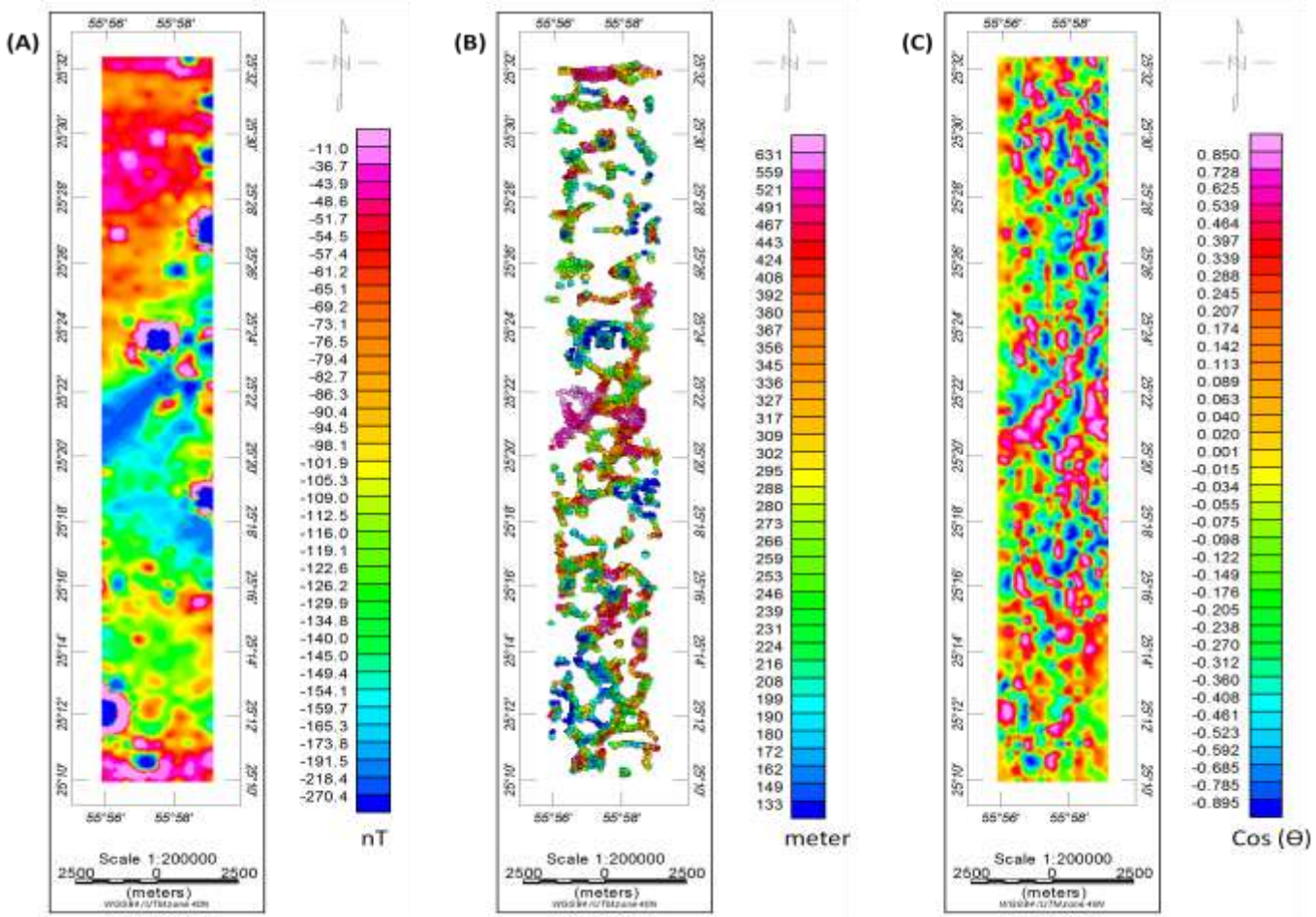

Figure 4.3. A) Residual magnetic anomaly map of the Dibba grid area. B) Euler deconvolution solutions of Dibba grid area C) Theta map of Dibba grid area

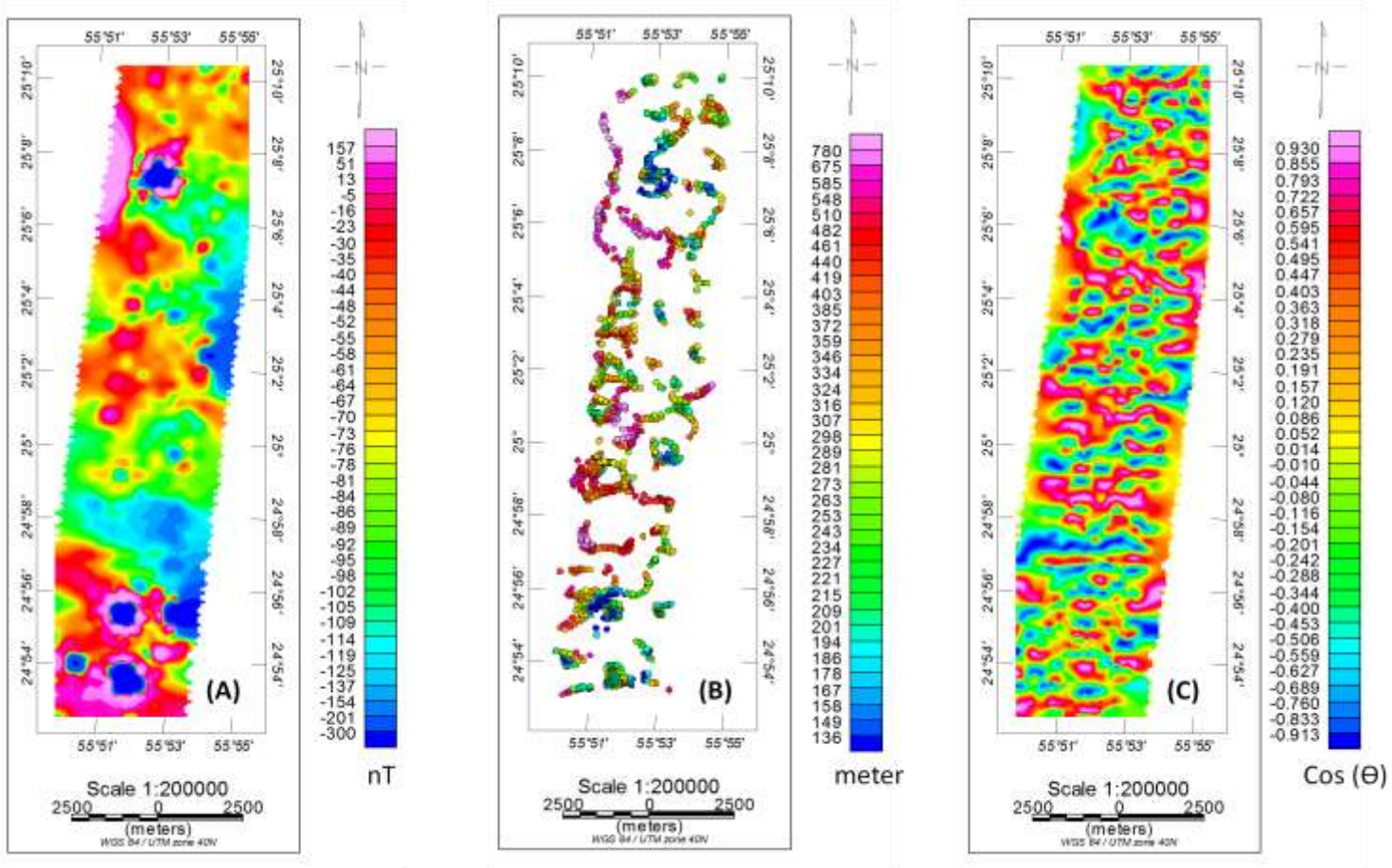

Figure 4.4. A) Regional magnetic map of the Hatta grid area. B) Euler deconvolution solutions of Hatta grid area C) Theta map of Hatta grid area

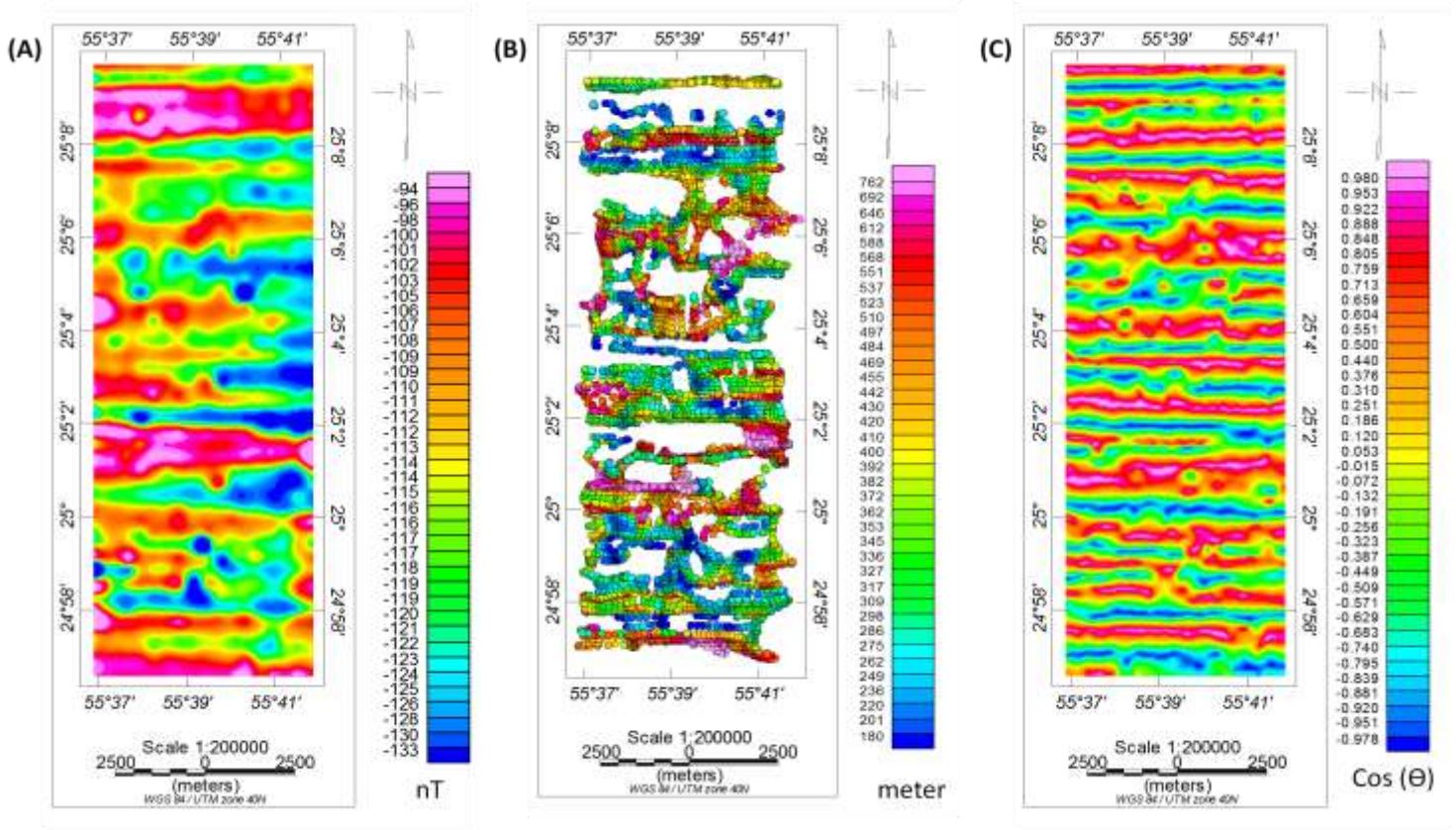

Figure 4.5. A) Regional magnetic map of the Awir grid area. B) Euler deconvolution solutions of Awir grid area C) Theta map of Awir grid area

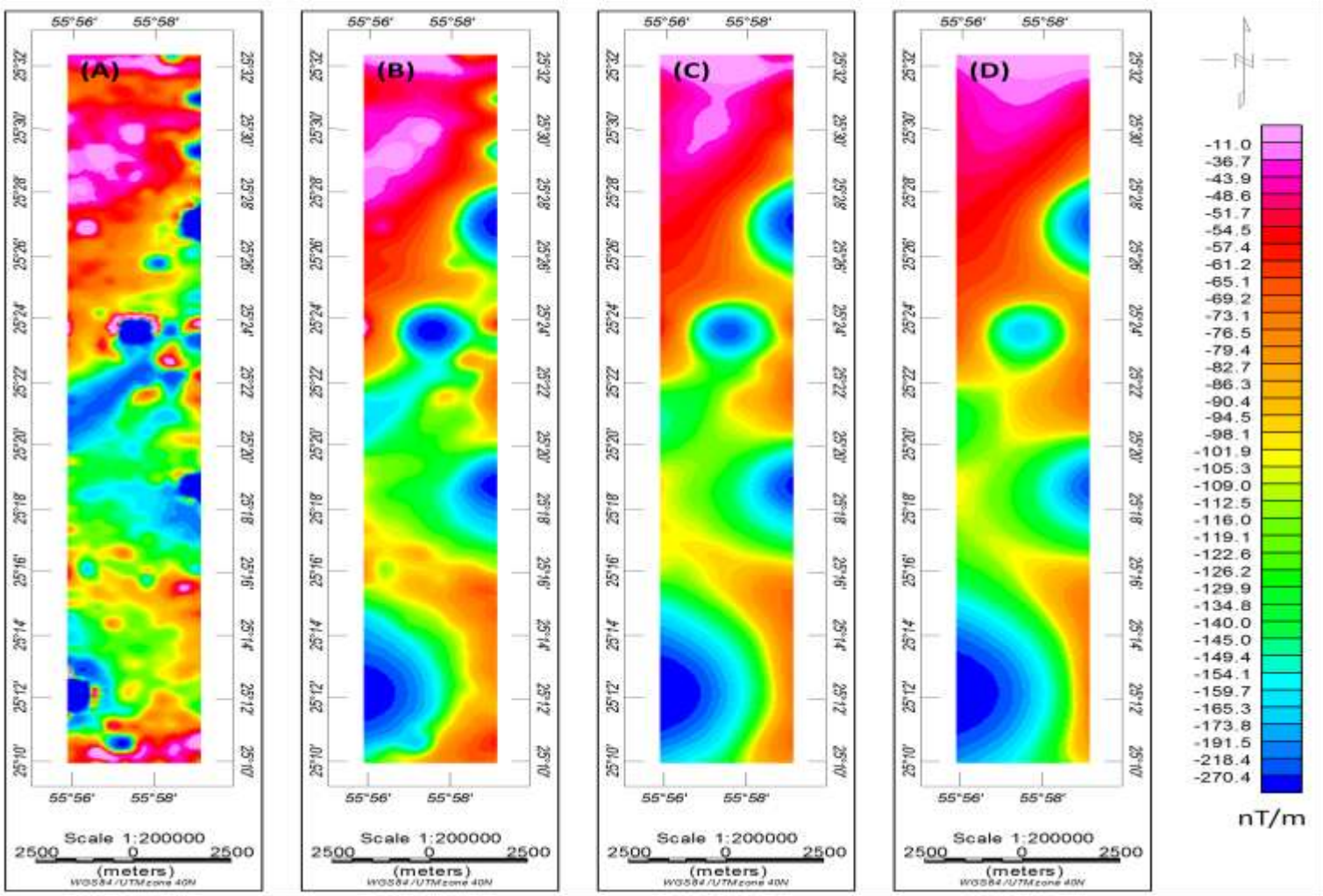

Figure 4.6. Upward continued magnetic anomaly maps of the Dibba grid area at different continuation heights: A) 100 m, 500 m, C) 1000 m and D) 1500 m

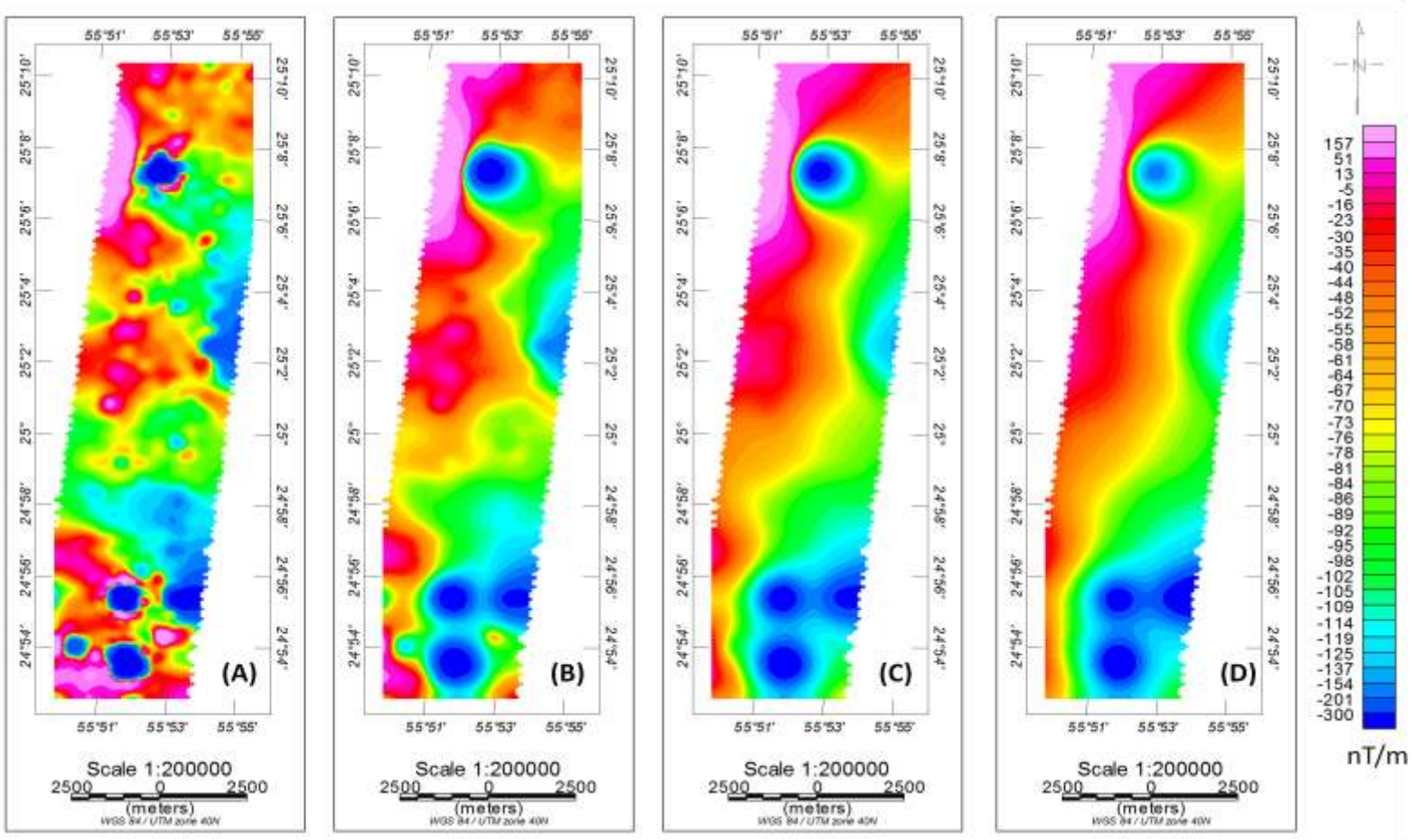

Figure 4.7. Upward continued magnetic anomaly maps of the Hatta grid area at different continuation heights: A) 100 m, B) 500 m, C) 1000 m and D) 1500 m.

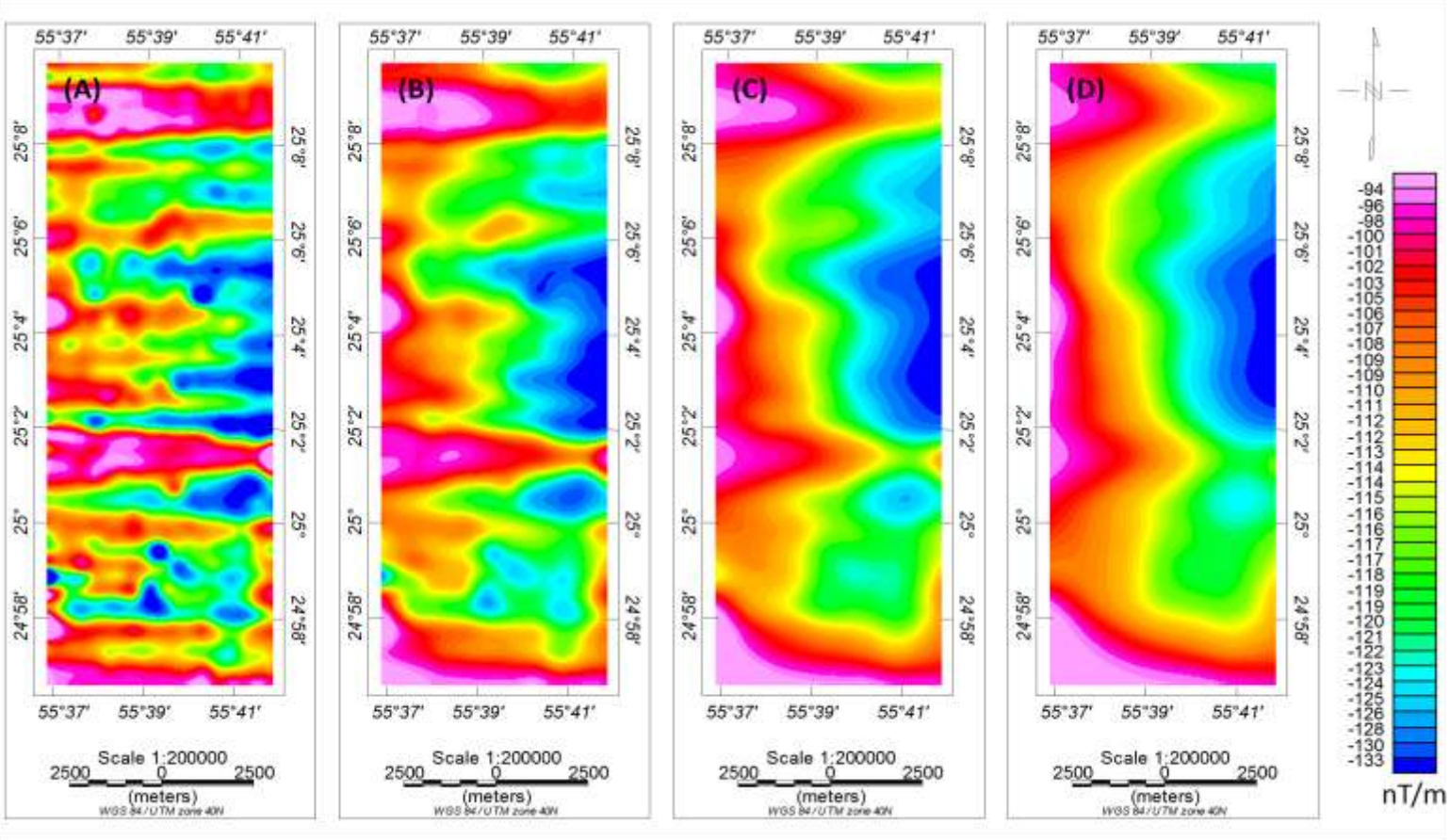

Figure 4.8. Upward continued magnetic anomaly maps of the Awir grid area at different continuation heights: A) 100 m, B) 500 m, C) 1000 m and D) 1500 m

4.1.5. Two-Dimensional Magnetic Modeling. A profile was selected for 2D interactive magnetic modeling from the Dibba and the Hatta grid areas in order to determine the subsurface structure of the fault zones. The profiles are oriented perpendicular to the structures of interest. The models were created using the GM-SYS software and the magnetic field elements used for the modeling include an inclination of 39° 3' and a magnetic declination of 1° 29'. Figures 4.8 and 4.9 show the results from the Dibba and Hatta grid areas respectively.

The model calculated from profile *A-A′* (Dibba grid area, Fig. 4.9) suggests three magnetic units. The top unit is characterized by unconsolidated gravel sediments as observed in the field. A susceptibility value of 0.000032 cgs was used for these unconsolidated sediments. This top unit is modeled to be ~ 600 m thick. The bedrock consists of a weathered zone ~ 600 m deep with lower magnetic susceptibility values within a lower unit of higher magnetization (~ 0.000349 cgs).

Figure 4.10 shows the modeling results along profile *B-B′* from the Hatta grid area. Again, three magnetic units are represented. The shallowest unit has a magnetic susceptibility of 0.000032 cgs and extends to a depth of ~ 1200 meter. The bedrock is modeled with higher magnetic susceptibilities values of 0.002596 cgs. Embedded in the bedrock is a unit with lower magnetic susceptibility values (0.000349 cgs) that extends 500m into the bedrock and is ~ 7 km wide.

4.2. AMT INVESTIGATIONS

AMT surveys were conducted to characterize the extension of the DFZ and HFZ into the gravel plain area. Also AMT investigations have been used to confirm the results of magnetic investigations of the pervious section. AMT data were collected along 123 stations. Profiles D (19 stations) and M (20 stations) (Figure 3.2) were designed to target the DFZ, and profile H (21 stations) was carried out to characterize HFZ. In addition, a grid of 63 CSMAT stations was conducted to characterize the area beneath the thermal anomalies and to determine whether DFZ and HFZ extend into the thermal anomaly area. This section describes the results of the AMT investigations.

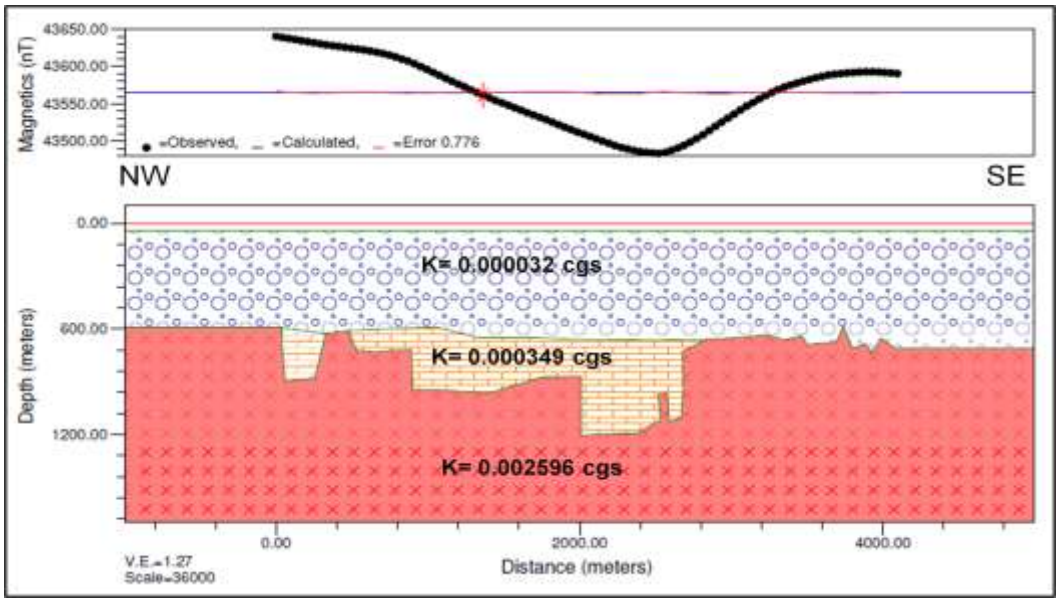

Figure 4.9. Magnetic modeling of profile A-A′from the Hatta grid area (see figure 4.1A for profile location)

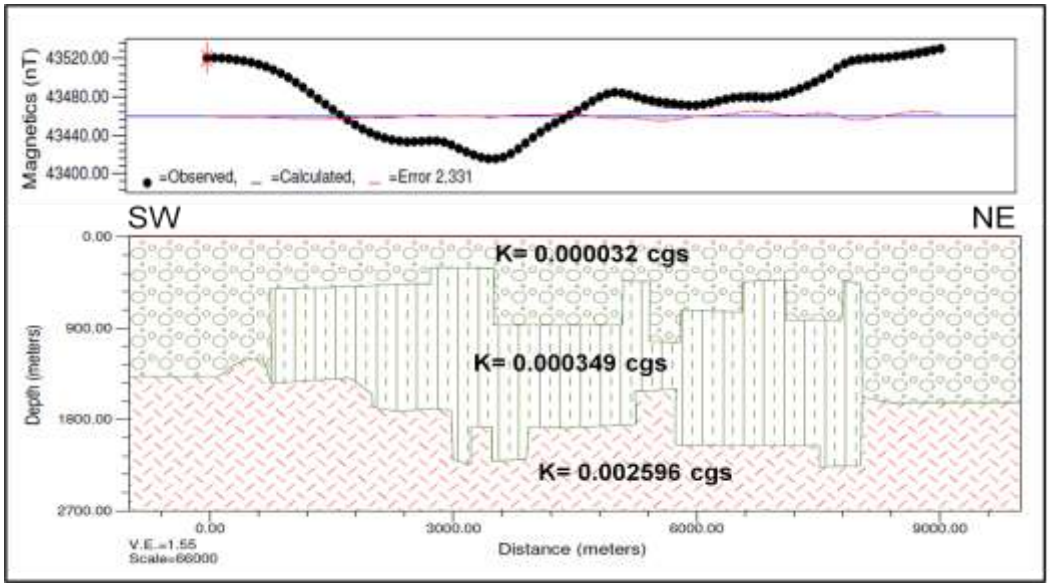

Figure 4.10. Magnetic modeling of profile B-B′from the Hatta grid area (see figure 4.1B for profile location)

4.2.1. Apparent Resistivity Maps. The apparent resistivities from the impedance tensor selected at different frequency ranges were gridded to produce a map of resistivity variations. Figure 4.11A shows the grid of apparent resistivity from the impedance tensor at 200 Hz which represents a deeper depth range (higher frequencies usually result in shallower depths of penetration while lower frequencies result in greater depths of penetration). This figure reveals a conductive linear body trending NE-SW crossing the northwestern part of the grid. Results of the next frequency 5010 Hz (Figure 4.11B) which characterizes the middle depth range shows the same conductive body as was seen on the 200 Hz map. At this frequency (5010 Hz), a resistive structure is observed. This feature has a linear shape trending NW-SE crossing the grid from the lower right corner to the upper left corner. However, this feature is interrupted when it intersects the conductive body. The same apparent resistivity results of frequency 5010 Hz have been repeated at higher frequency 50100 Hz (Figure 4.10C).

4.2.2. Two-Dimensional Inversion. The 2D inversion was performed on the AMT profiles using the WinGLink software package that utilizes Rodi and Mackie (2001) algorithm code. The inversion has been applied on TE mode data, TM mode and both. The disadvantage of this code is that it uses both apparent resistivity and phase data to apply the inversion. Several stations had bad phase data while the resistivity data were perfect at this station, so due to this limitation some stations were deleted from the thermal anomaly area.

The results of profile (D) with 2-D inversion in TM mode (Figure 4.12) show three conductive bodies. The first conductive body (> 50 ohm.m) is located to the SE between stations D1 - D3. The second conductive body (~50 ohm.m) is located at station D05 and it cuts geoelectrical layers from 500 and deeper. The third body (~65 ohm.m) is located to the NW at stations D15 – D19 extending to a depth of 500 m. The area in the middle of the profile is resistive (~ 150 ohm.m) and extends beneath the conductive zone to the NW.

Figure 4.13 shows the results of 2D inversion of profile (B) in the TM mode. Generally this section is characterized by low conductivity since it has a uniform resistivity (20 – 30 ohm.m).

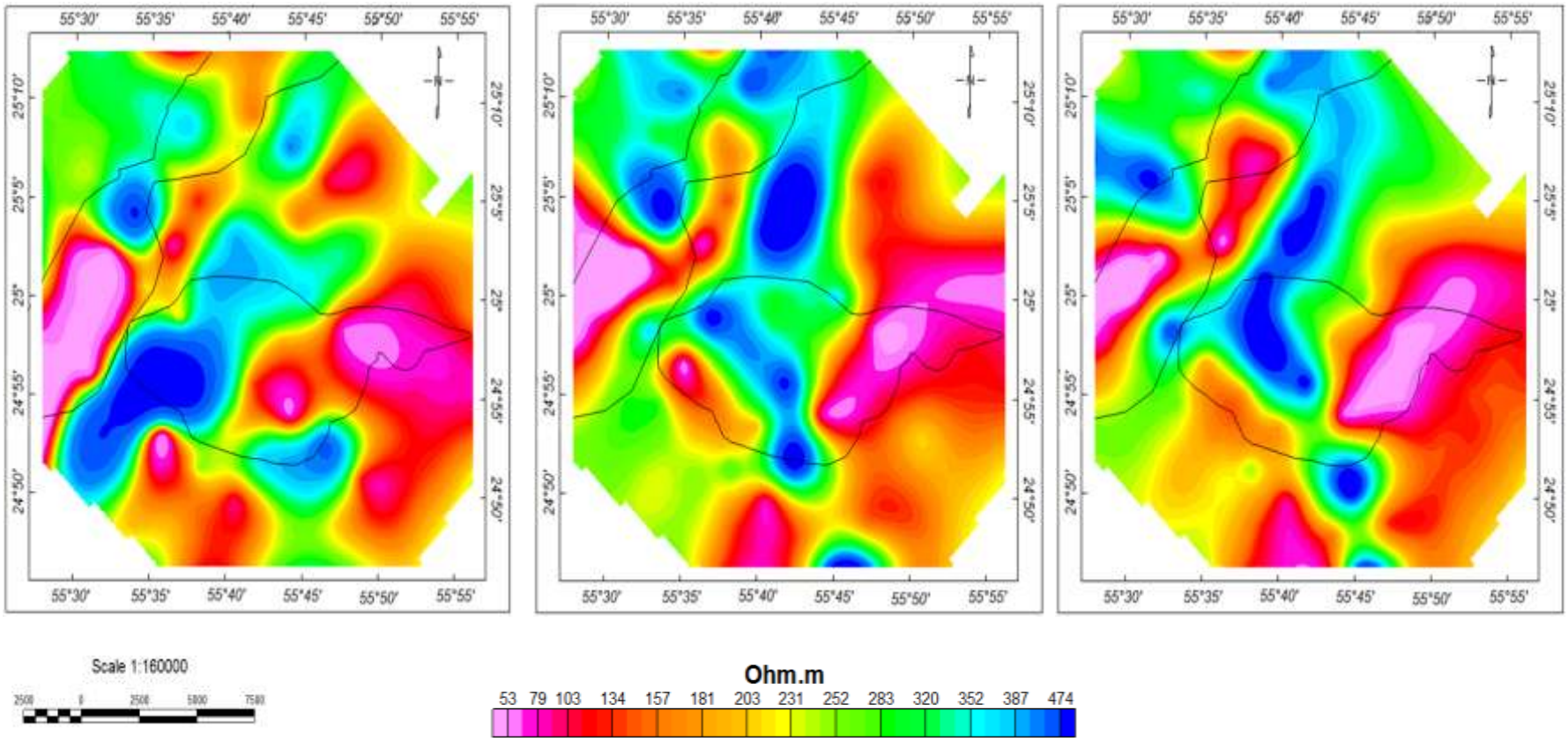

Figure 4.11. 2D grids of apparent resistivity from the impedance tensor determined from selected frequencies A) 200 Hz , B) 5010 Hz, C) 50100 Hz. Black lines delineate the location of the thermal anomalies. Arrows show the conductive body (NE-SW) crossing the area and dashed arrows show another body perpendicular to the conductive body

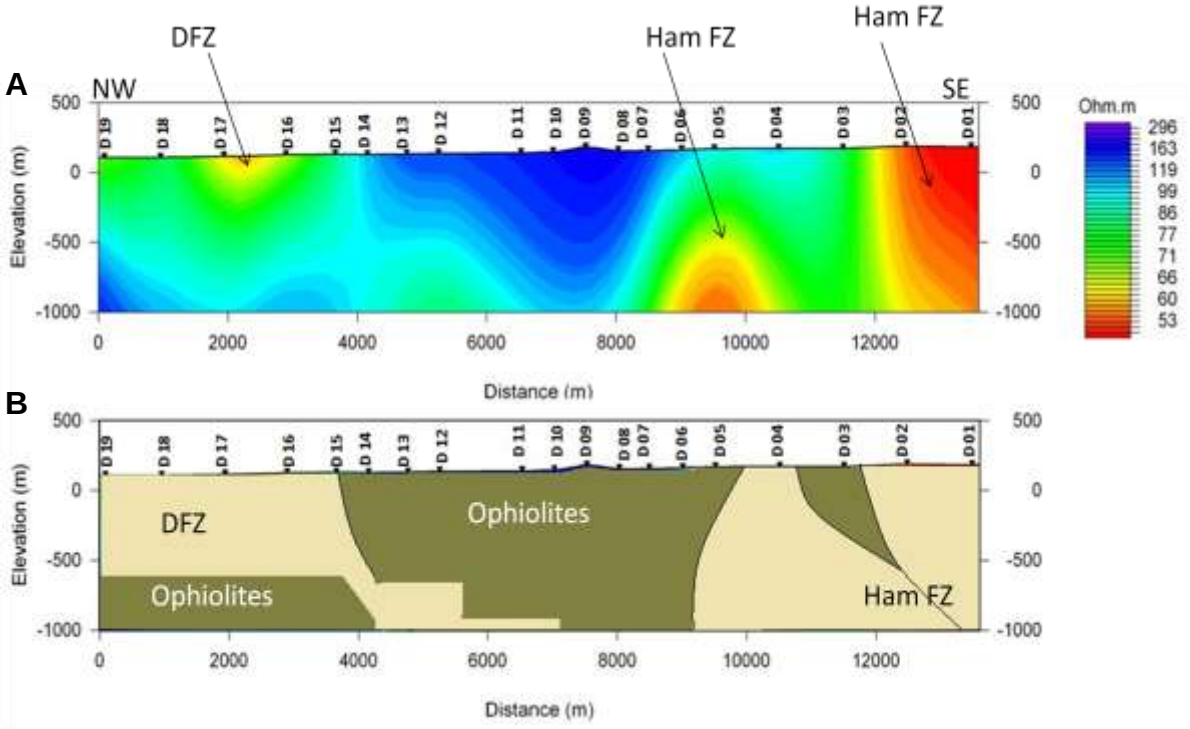

Figure 4.12 A) Two-dimensional inversion resistivity model along profile (D) in TM mode and black arrow showing DFZ (See figure 3.2 for location). B) A model shows the geological representation of the geoelectrical results of profile (D).

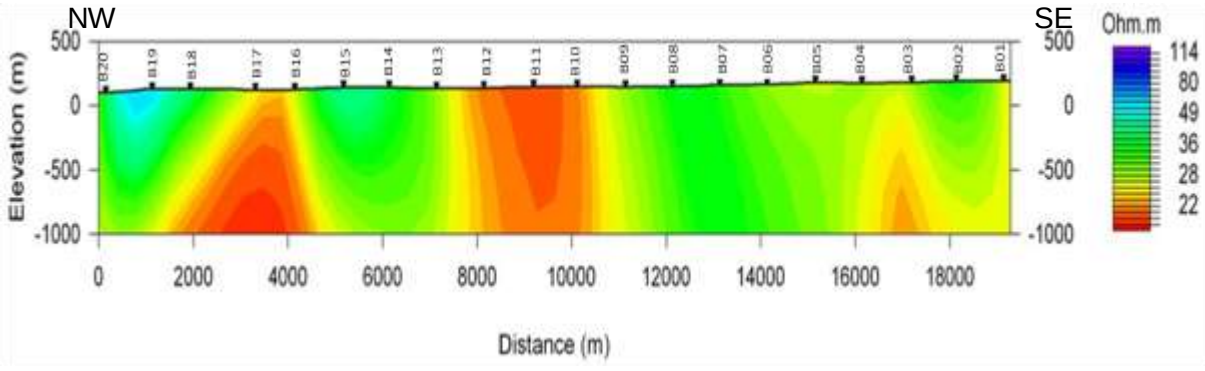

Figure 4.13 Two-dimensional inversion resistivity models along profile (B) in TM mode (See figure 3.2 for location)

Figures 4.14 and 4.15 show the results of the 2D inversion of the AMT data along profiles from the thermal anomaly area. The station spacing here was ~ to 5 km due to the size of the area. These profiles are divided into two groups based on their azimuth.

The first group was inverted in the TM mode and produces the 2D models of the following profiles DI 02, DI 04, DI 06 and DI 07 (see Figure 3.2 for the location). A conductive body (~10 ohm.m) is observed along these profiles from NW and SE directions of the profiles (Figure 4.15).

The second group oriented NE-SW and inverted in TE mode, is represented by five lines HA 02, HA 03, HA 04, HA 05 and HA 09 (see figure 3.2 for the locations). A main geoelectrical conductive body (~ 10 ohm.m) is observed on all profiles. This body is located close to the NE end of the profiles. The conductive body trends SE-NW with slight change in the dimensions along the profiles (Figure 4.14).

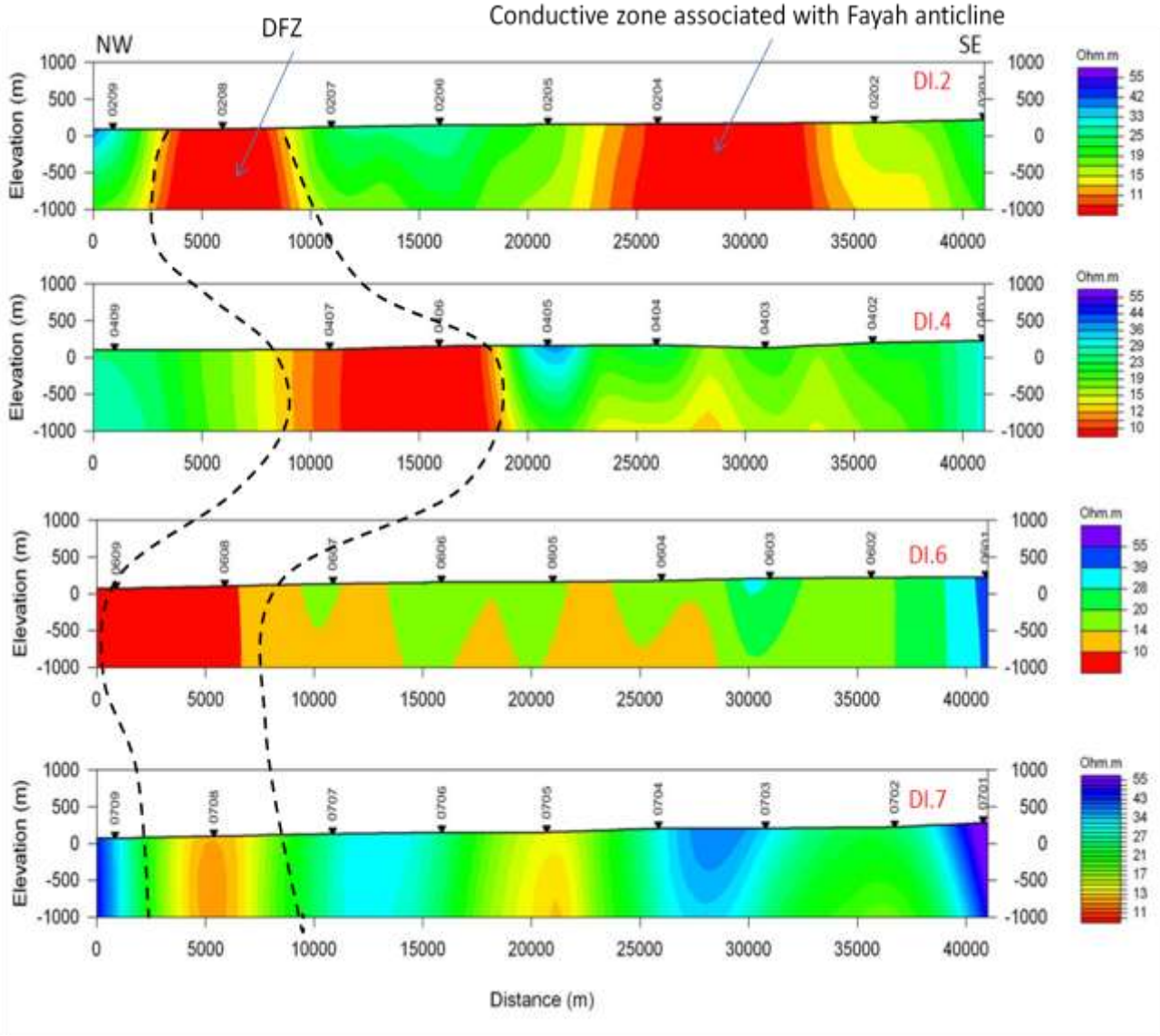

Figure 4.14 Two-dimensional inversion resistivity models of DI profiles in TM mode. Dashed lines show the extension of the conductive body crossing the profiles.

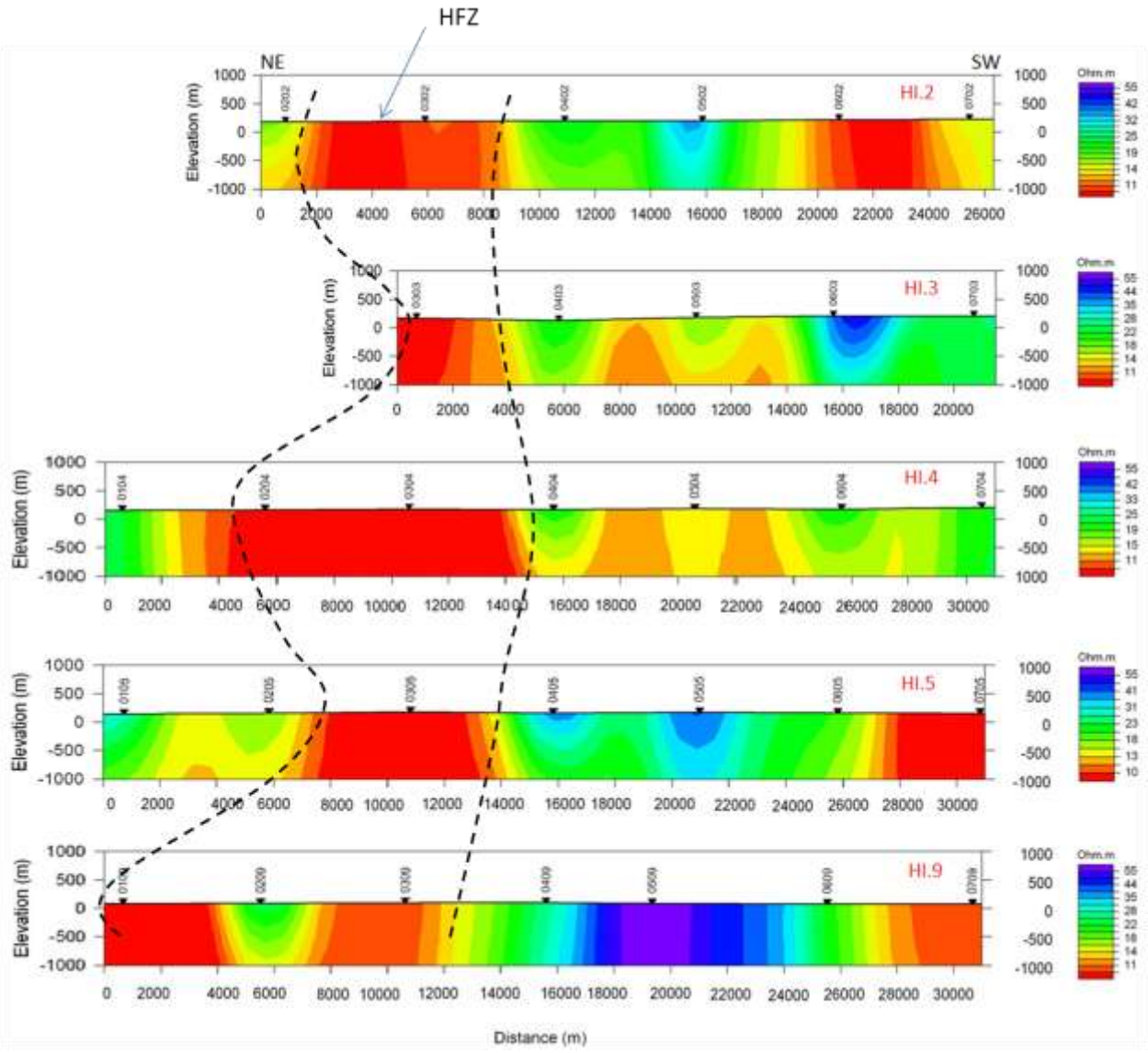

Figure 4.15 Two-dimensional inversion resistivity models of HA profiles in TE mode. Dashed line shows the extension of the conductive body crossing the profiles.

5. DISCUSSIONS

5.1. INVESTIGATING THE EXTENSION OF MAJOR FRACTURE SYSTEMS WITHIN THE GRAVEL PLAIN AREA

Surface thermal anomalies were investigated using MODIS thermal data in the sand dunes area of the northern United Arab Emirates. The cause of the anomalies is suggested to result from soil temperature variation due to cooler groundwater. These anomalies were interpreted as hydrological response to rainfall in the Hajar Mountains which are considered the main recharge areas of the UAE (Ghoneim et al., 2005).

The purpose of this study is to test the hypothesis that thermal anomalies observed on remote sensing images over the deserts of N.UAE are the result of cooler shallow water reservoirs fed by subsurface faults (DFZ & HFZ) extending from the Hajar Mountains into the gravel plains and sand dunes area. To achieve this purpose, geophysical investigations, in particular the magnetic and AMT techniques were used to determine the extent of the DFZ and HFZ. Glennie el al. (1974), Styles et al. (2006) and others have studied the surface geology of DFZ and HFZ in detail where they are exposed in the Hajar Mountains. However, no geologic investigations have addressed the question of the extension of these fault zones beneath the gravel deposits to the west. Nevertheless, geochemical studies by Rizk and Garamoon (2006) suggest that the main structures of the N. UAE (DFZ, HFZ and Ham Fault Zones) feed the aquifers of the central gravel plain, since the chemical composition of groundwater in the Dhaid area (the main agricultural region in the gravel plain area (Figure 5.1)) is similar to the chemical composition of the Hajar Mountains (Recharge Area). Geophysical surveys conducted within the gravel plain area characterized major fracture systems. Magnetic data were conducted along two grids, the Dibba grid (to investigate the DFZ and Ham FZ, and the Hatta grid (Figure 3.2). Also the AMT technique was used to complement the magnetic data.

Fault zones are characterized by fractured rocks which enhance weathering and permit fluid flow (Cook et al., 2003). Hudson et al. (2008) suggest that the magnetic contrast across faults result from tectonic juxtaposition of rocks with different magnetic

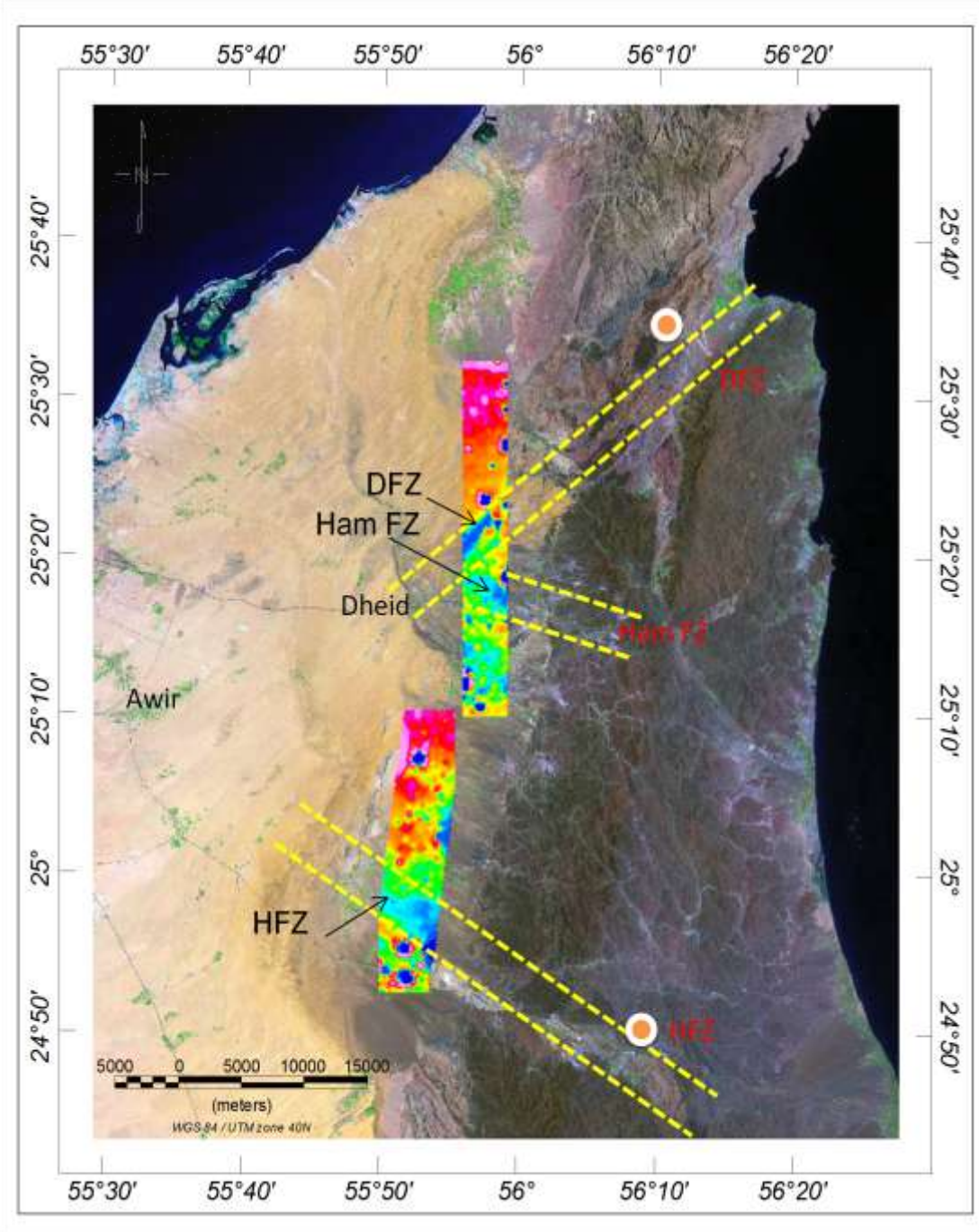

Figure 5.1. Satellite image of the N. UAE showing extension of the DFZ and HFZ (red lines) into the gravel plain area (black arrows) and coincidence of the linear magnetic anomalies along the extensions of the DFZ and HFZ. Orange circles show the location of earthquakes with high magnitude in this region (Dibba earthquake in 2007 with magnitude = 4.5 and Hatta earthquake in 2002 with magnitude = 4.3).

properties, or due to secondary geochemical processes such as mineralization and alteration.

Faults zones can be represented as sharp linear magnetic anomalies or by lower or higher magnetization.

Ground magnetic results of the Dibba grid area revealed two linear low magnetic anomalies coincident with the extension of the DFZ and Ham Fault Zones beneath the Quaternary sediments. These anomalies are described in chapter 4 (Figure 4.1A). The low magnetic values of this anomaly are interpreted to result from the weathered rocks and rock with lower magnetic susceptibility such as allochthonous units that fill the Dibba zone (Section 2.4.1). Similar low magnetic anomalies associated with fault zones have been observed by Yumul and Dimalanta, (1997) and Fujiwara et al., (1999) when they utilized the magnetic method to characterize fault zones within ophiolite units. The first anomaly trending NE-SW is a major magnetic feature and as coincident with the exposed DFZ. Therefore, the location and the trend of the magnetic anomaly suggest the extension of the DFZ to the gravel area. The second anomaly is associated with the fault zone trending NW-SW and crossing the anomaly associated with the Ham FZ (Figure 4.1 A). Application of potential field techniques such as upward continuation and Euler deconvolution suggest that both the DFZ and Ham Fault Zone are not deeply seated since these anomalies are attenuated when the data is upward continued to 600 m (Figure 4.6) and the Euler deconvolution solutions along DFZ suggest depths of ~ 600 m (Figure 4.3B). Tectonically, the DFZ is a fault zone that splays of from a major transform fault called “The Oman or Dibba Line” that crosses the Gulf of Oman and is associated with other major faults along the Zagros such as Zendan. The Oman line is a right-lateral strike-slip fault forming the boundary between the continental collision of the Arabian and Eurasian plates (Robertson et al., 1990a).

The two-dimensional AMT inversion results of profile (D) (See Figure 3.2 for location) shows three conductive (reciprocal of the resistivity) zones (Figure 4.12). These conductive zones (Figure 4.12) are coincident with the magnetic anomalies associated with the DFZ and Ham Fault Zones. Two of the three conductive bodies located at the SE end of profile (D) are coincident with the magnetic anomaly associated with the Ham Fault Zone. The third conductive body is located at the NW end of the profile coincident

with the DFZ. Such vertical conductive anomalies have been observed at several large scale transform fault systems such as the San Andreas Fault (Unsworth and Bedrosian, 2004) and the Tintina strike slip fault, Northern Canada (Ledo et al., 2002). This conductive zone (known as fault zone conductivity) seems to be prevalent although not universal for many continental scale transform faults (Jones, 1998).

Conductivity anomalies along fault zones can result from the presence of fluids within juxtaposition of two units with different conductivities, clay mineralization within the resulting fractures, and precipitation of conductive minerals phases such as serpentine, graphite and metallic minerals (Elektb Group, 1997 and Jones, 1998).

Serpentinites which are mainly composed of serpentine make up the majority of the rock units within the DFZ (Styles et al. 2006). Since serpentinites are characterized by high conductivity (Stesky and Brace, 1973), serpentinite could be the source of high conductive bodies associated with the DFZ and HFZ. However, this explanation is not consistent with the magnetic data. Serpentinites typically are characterized by high magnetization since serpentinites are rich in mafic minerals such as magnesium and iron (Hunt et al., 1995 and Coleman, 1971). The magnetic data suggests rocks/minerals with lower magnetization along the fault zones; hence the high conductivity is not due to the presence of serpentinite. The most logical source for the high conductive anomalies in the AMT data is pore fluids and or presence of clay minerals. The range of the resistivity values obtained from this study (20 – 70 ohm.m) is comparable to the resistivity of clays and freshwater (Palacky, 1987), since salt water resistivity is less than 1 ohm.m.

Profile D shows a block of high resistivity (~ 150 ohm.m) at stations from D06 to D14. Searle, (1988) described three cross sections parallel to the profile D located between Dibba town and the area where profile D was acquired. These sections show a mass of dense ophiolite units outcropping in the middle of the DFZ which are the source of the high resistivity in the middle of profile D (Figure 4.12B). Furthermore, magnetic results of the Dibba grid area show discrete high magnetic anomalies in the middle of the DFZ which are characterized by low magnetization; this high magnetic anomaly is interpreted as due to slivers of ophiolite (high resistivity) within the DFZ. Also 2D inversion results of profile (D) show that the conductive zone associated with the DFZ reaches ~500 m depth within the gravel area similar to the depth estimated from the

upward continuation filter and Euler deconvolution techniques. Thus the AMT results of profile (D) confirm the extension of DFZ into the gravel plain.

The HFZ is ~ 60 km to the south of the DFZ and is characterized by the magnetic results of the Hatta grid area as a linear, low magnetic anomaly trending NW-SE. The DFZ and HFZ have similar geological and structural setting (Nasir and Klemd, 1998), therefore the interpretation of the magnetic anomaly caused by HFZ is similar to the magnetic anomaly caused by DFZ. In addition, Euler deconvolution and upward continuation techniques (Figures 4.4B and 4.7) show that HFZ is also not deeply seated, similar to DFZ.

5.2. INVESTGATING THE EXTENSION OF MAJOR FRACTUE SYSTEMS WITHIN THE THERMAL ANOMALY AREA

Generally magnetic results of the Dibba and Hatta areas suggest that DFZ and HFZ extend beneath the gravel plain sediments into the western part of the survey areas at the border of the desert plain, however these data do not confirm if these fault zones extend into the thermal anomaly areas to the west of the gravel plain. Therefore a magnetic survey was conducted in the Awir area (Green Rectangle, Figure 3.2) to investigate whether the DFZ and HFZ extend into the thermal anomaly. Magnetic results of the Awir area (Figure 4.1 C) did not detect the DFZ & HFZ beneath the thermal anomaly areas possibly due to the presence of the thick sand dunes (~ 50 m) or the absence of Ophiolite Units that are the source rocks. The AMT data is used to determine if the faults extend into the thermal anomalies area.

Apparent resistivities maps were created from select frequencies (40, 5010, 50100 Hz) from the AMT data over the thermal anomalies area as shown in figure. 4.11. These maps show a north east trending conductive anomaly coincident with the trend of the DFZ. This anomaly can be directly superimposed on the thermal anomaly detected in August, 2003 (Ghoneim et al, 2005) (Figure 1.6) which strongly suggests that the thermal anomaly is caused by moisture within the DFZ. This conductive zone extends to depth as observed on the frequency map at 40 Hz.

2D inversion of profiles DI 01 to DI 07 (see figure 3.2 for locations) show a conductive body (10-15 ohm.m) (Figure 4.14) crossing all these profiles at the NW end

which is coincident with the extension of the DFZ. It is difficult to estimate the dimensions of the conductive body since the profile spacing and station spacing is 5 km. Most of the agricultural areas (e.g. Awir, Dhaid) (Figure 5.1) in N. UAE are located along the extension of the DFZ as mapped from remote sensing analyses (Ghoneim, 2008), and geological studies (Glennie et al, 1974, Searle, 1988, and Styles et al. 2006). 2D AMT inversion results along profiles HA 01- HA 09 (Figure 4.15) show a conductive zone associated with the extension of the HFZ. This conductive zone is observed on all the profiles at the NE end of each profile.

5.3. INVESTIGATING THE CAUSE OF THERMAL ANOMALY

The cause of the thermal anomalies can be summarized by posing the following questions:

1. Is it possible that groundwater can flow from the recharge area to the thermal anomalies area (30 to 60 km) within 4 days (8-15 km/day)?
2. How does the groundwater reach the surface of the dunes with average heights of 40-50 m?

Three hypotheses can be postulated to explain the observation. The first is that the groundwater flows through the ophiolite units or gravel porous media for a distance of ~45 km in a few days. We can estimate the groundwater flow velocity in porous media (e.g. gravel) using Darcy's Low (Cook, 2003):

$$V = Q/A \qquad (5.1)$$

$$V = -K(\Delta h/\Delta L) \qquad (5.2)$$

Where V is groundwater velocity, Q is flow rate, A is total cross sectional area of the material, k is hydraulic conductivity, Δh is hydraulic gradient and ΔL is distance of the water flow. Since we do not have sufficient information, it is difficult to provide accurate calculations but the available information is helpful in estimating the velocity of the groundwater within the gravel units. Since the average distance between the Hajar Mountains and thermal anomalies area ΔL is 45 km and the hydraulic head Δh is 100m (Figure 2.6), average hydraulic conductivity K= 15.48 (K K=T/b where T is the

transmissivity = 776 m^2/day (Rizk and Gramoon 2..6) and b is the average thickness of the aquifer 50m), so the velocity of the groundwater is .0344 m/day (Typical rates of groundwater flow are 1-100 m/day (Cook,2003)). At this rate of groundwater flow, recharge events will take ~1.1 million days to reach the thermal anomaly. Therefore this scenario is not feasible and cannot be used to explain the occurrence of the thermal anomalies three days following the rainfall events in the recharge areas.

The second hypothesis postulates groundwater flow through fractured media along the DFZ and HFZ. Several factors control groundwater through fracture zones such as fracture zone aperture, fracture orientation, and in situ rock stresses (Henriken, 2006). In general, Barton et al. (1995) and Caine et al. (1996) suggest that groundwater flow within fractures is enhanced compared to the surrounding area. Thus, the high groundwater flow velocities within fracture zones could possibly explain the thermal anomalies. However, the following studies show the difficulty of getting proposed rate of groundwater flow. Since the clay minerals may result from altered silicate minerals within the fault zones, clogging effect of clays can reduce the permeability of the fracture zones (Olesen et al. 2006). Henriken (2006) documented from well log data that the average flow rate within fractures do not vary significantly from surrounding areas. Therefore, this hypothesis is also not feasible. As noted above, groundwater flow is controlled by several factors, therefore estimating the typical groundwater velocity through fractures is not possible. However, Figure 5.2 show that the typical groundwater velocity through fracture ranges from 0.001 to 100 (m/day). Again such groundwater flow rate cannot explain the observed occurrence thermal anomaly.

The third hypothesis assumes continuity of the aquifer from the recharge area to the discharge areas (Thermal anomalies area) within confined ophiolite fractured units (Figure 5.3). If this is true, then rainfall events in the recharge area will increase the water level resulting in an increase in the potentiometric surface (water pressure surface). Consequently, groundwater levels in the discharge area will rise towards the surface similar to artesian aquifer systems (Tarbuck et al., 2006).

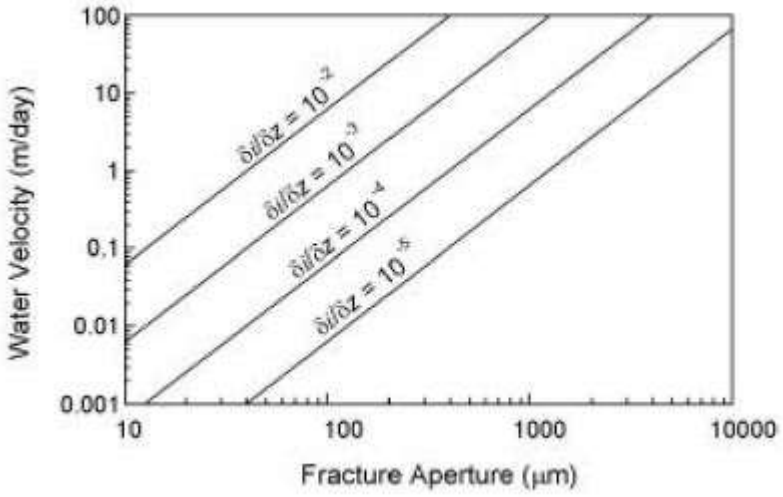

Figure 5.2. Water velocity within fractures as a function of fracture aperture and hydraulic gradient (Cook, 2003)

Association of the thermal anomalies with rainfall events in recharge area confirms the influence of the rainfall on the aquifer pressures.

It is necessary to prove continuity of the aquifers from the recharge area to the discharge area in terms of supporting the third hypothesis. In addition to the geophysical results of this project that show the extension of the fault zone to the sand dunes area, geochemical investigations by Rizk and Garamoon, (2006) in the Dheid Area (Figure 5.1) suggest that aquifers of the gravel plain and sand dunes areas are hydraulically connected to the Hajar mountains aquifers. The Dheid area is located at the border of the sand dunes and gravel plain areas to the SW of the magnetic and AMT survey areas. Geochemical studies report low temperatures (32°*C*), low salinity (<1.5 *mS/cm*) and high Mg and HCO_3 of water samples collected from wells along lineaments associated with the Dibba, Ham, and Hatta Fault zones. Water samples from wells located away from these lineaments show high temperature (39°*C*), high salinity (4.5 to 7.5 *mS/cm*) and high Na and Cl. The source of the low temperature, low salinity, Mg and HCO_3 is water from the Hajar Mountains. Therefore the fault zones such as DFZ connect the aquifer of gravel plain and sand dunes area such as the Dheid aquifers to the Hajar Mountains (recharge

area).

This hypothesis requires the aquifer to be bounded with aquitard layers such as ophiolites. Ophiolite units outcrop in the Hajar Mountains (recharge area) then disappeared in the gravel plain. There is no indication of the extension of these units to the west of the Hajar Mountains except a mass of ophiolite outcrop within the Fayah anticline's core (located within thermal anomaly area) (Figure 5.3 D).

The magnetic and AMT data suggest that the DFZ and HFZ extend into the area where the thermal anomalies were observed through ophiolite layers (Confined) that occur shallower at this area. These fault zones link the recharge area to the thermal anomalies area. Both fault zones have been characterized crossing all profiles of the AMT grid area within the thermal anomalies region, which means that these faults are intersecting at the thermal anomalies area. Fault zones intersection cause deformation that highly fractures the layers. Studies such as (Gartrell, 2004) show that faults intersections areas are known by highly efficient fluid channeling that deposit minerals. Sodsri (1992) support that this area is highly fractured and these fractures reach the surface. He provides a schematic cross section (based on the seismic data) of the structural setting of the N. UAE from Oman Mountains in the east to the Gulf in the west (Figure 5.4). This section (see figure 5.3 for location) provides insights into the subsurface layers of the Marghum area. The Marghum area is located parallel to the thermal anomalies area separated by a few kilometers to the south of the Ajarib outcrop (Figure 5.3), which suggests that both areas have a similar structural setting.

The Malaih outcrop (named by Glennie et al. (1974)) and locally known as Ajarib (Figure 5.2) (Lat: 25° 1' 18.986" N Lon: 55° 43' 52.472" E). This outcrop can be barely seen in the middle of the sand dunes (Figure 5.2 A) and it is located on the area parallel to the fracture zone characterized by Sodsri, (1992). Ajarib is an anticline composed mainly of limestone. Field investigations showed that it is highly fractured and some of these fractures are filled with calcite, providing supporting evidence for the cause of the thermal anomalies.

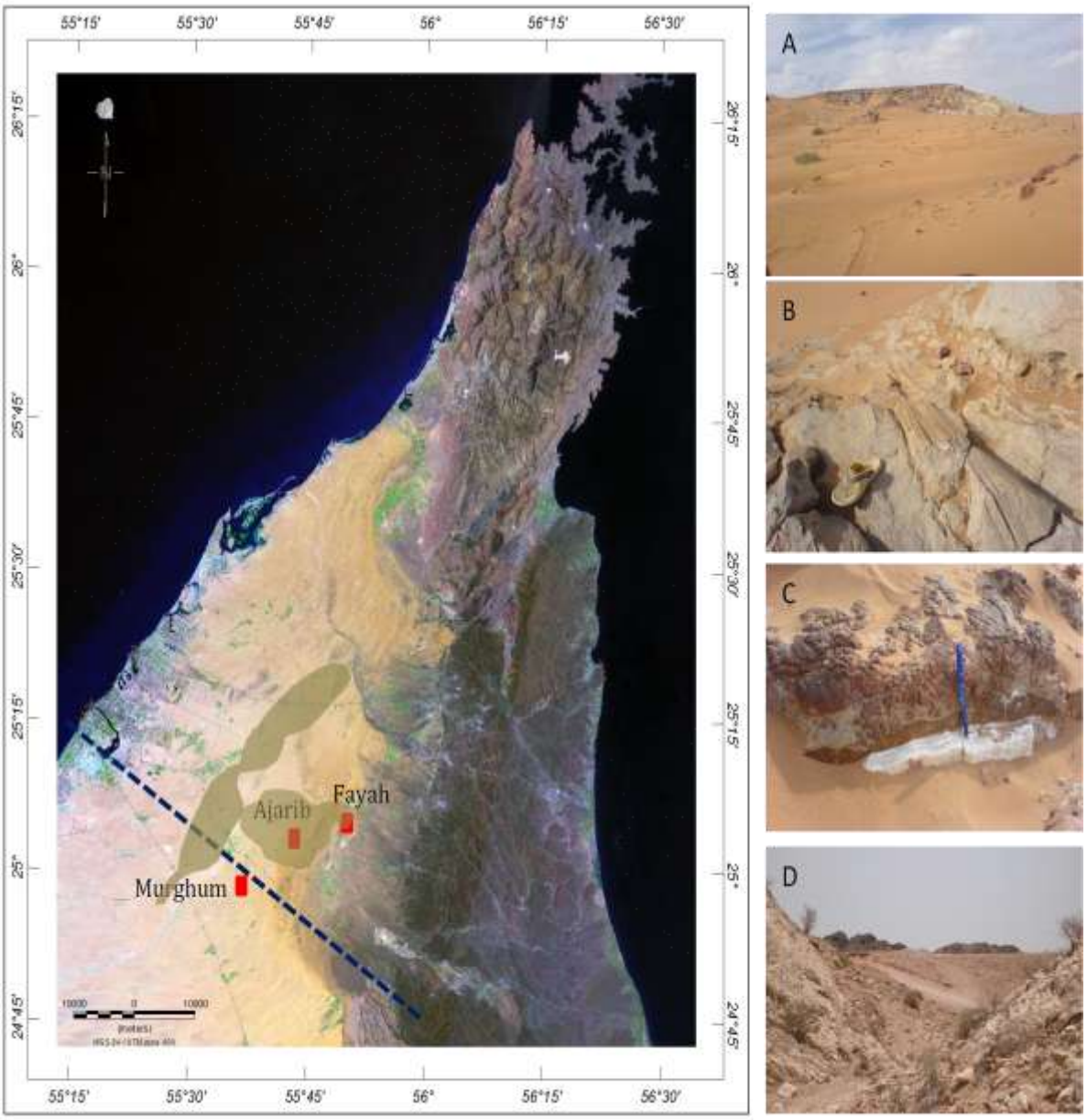

Figure 5.3. Satellite image of the N. UAE illustrating locations of Ajarib, Fayah and the location of cross section made by (Sodsri, 1992) and the shaded areas are the location of the thermal anomalies (Ghoneim et al., 2005). A) Image shows Ajarib outcrop, B) Image shows the fractures within Ajarib outcrop, C) Image shows fractures filled with calcite; D) Image shows the ophiolite mass within Fayah. Dashed line represents the location of the cross section shown in Figure 5.4.

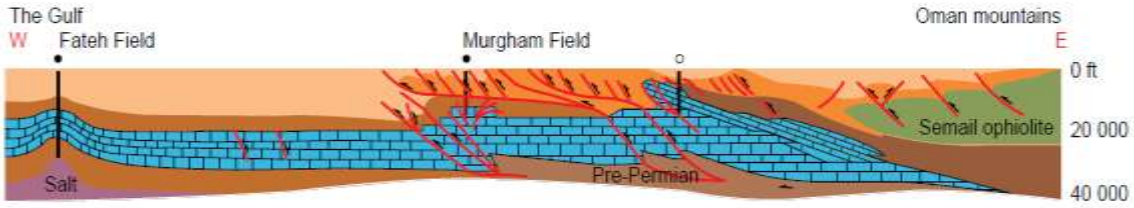

Figure 5.4. Cross section of the N. UAE showing the structural setting from Oman Mountains to the Gulf, from (Sodsri, 1992)

Ajarib outcrop, which is not mentioned in any geosciences studies except (Glennie et al,. 1974) by Malaih, is characterized by fractures filled with calcite (Figure 5.3 C). This provides evidence of paleohydrology (Wallin and Peterman, 1999) or groundwater occurrence at the surface. Additionally, the density of the fractures within the Ajarib indicates that the area is highly fractured. Based on the information obtained from on site observation of Ajarib outcrop and the cross section produced by Sodsri (1992), we conclude that the area is highly deformed by faulting. In addition, calcite deposition indicates that these faults channel the groundwater to the surface. Anecdotal evidence from farmers of the surrounding agricultural areas (Awir and Li Hibab) suggest a transient rise in the water table associated with rainfall events in the recharge area followed by a rapid drop (~ 2 weeks) of water levels. During the rainfall and based on the amount of the rain the water table should rise for at least several weeks to approximately several months during rainfall season based on farmers observations. Therefore, we suggest that this rapid fluctuation is due to the fracture network beneath the thermal anomalies area where we expect the DFZ and HFZ to intersect.

5.4. CONCEPTUAL MODEL

Figure 5.5 shows the conceptual model of the area before and after rainfall events when the thermal anomalies occur. Basically the water table level in the dry season in the recharge area is low (Figure 5.5A) but increases during rainfall events, increasing the height of the potentiometric surface and the pressure on the aquifer beneath the anomaly

area. The crystalline rocks (Ophiolite) are not permeable but due to the fracture network beneath the anomaly area resulting from the intersection of the DFZ and HFZ, the groundwater rises to the surface through the fractures resulting in the cooler temperatures observed in the TIR images.

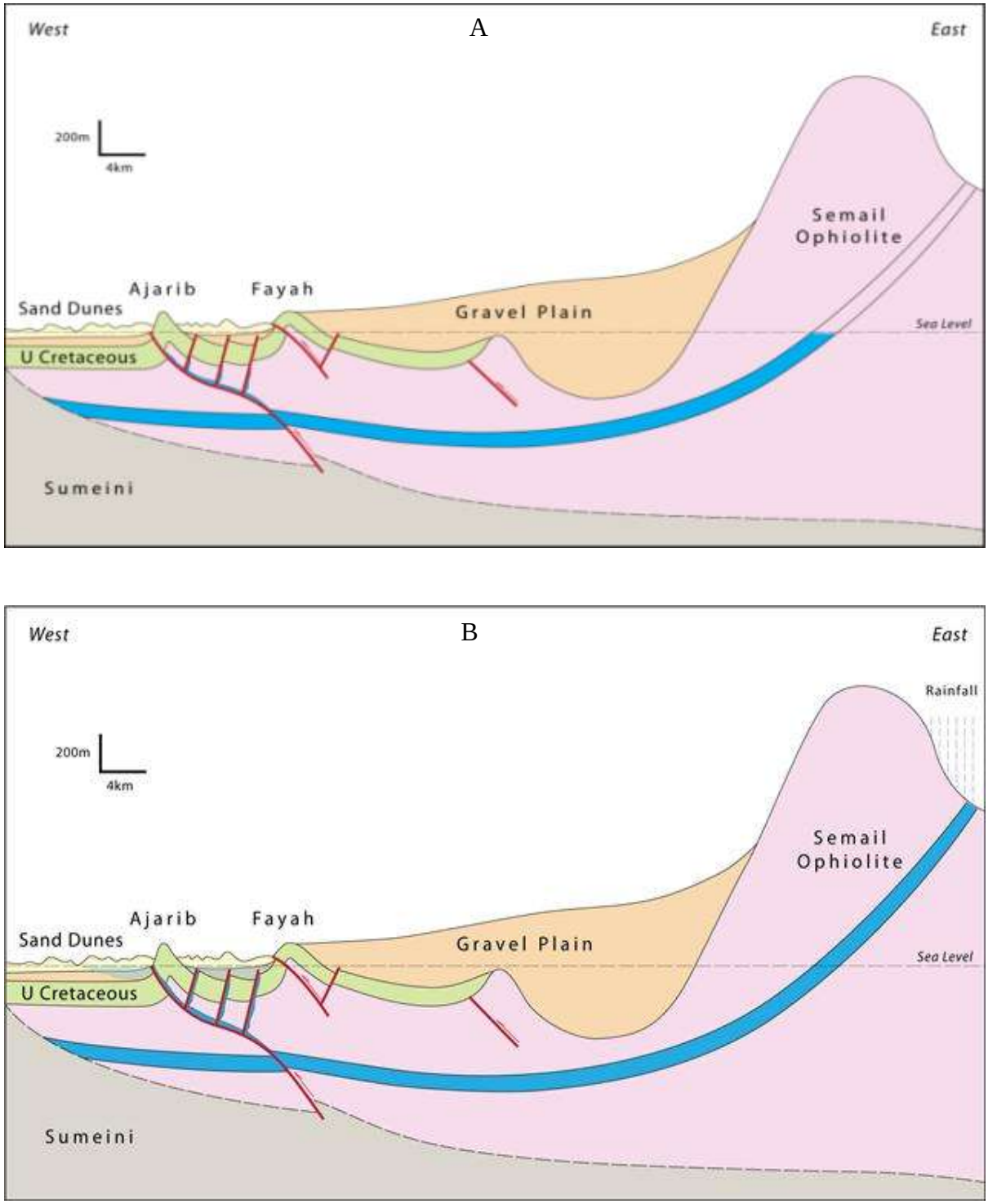

Figure 5.5. Conceptual model shows A) Groundwater level at arid seasons and B) the influence of the rainfall on the groundwater level beneath the study area

6. CONCLUSIONS AND RECOMMENDATIONS

6.1. CONCLUSIONS

Magnetic and a hybrid magnetotelluric technique were used to determine the extension of the DFZ and HFZ into the desert plains of the northern UAE in order to explain the source of thermal anomalies observed after rainfall events in the recharge areas in the mountains. Magnetic results suggest the extension of DFZ and HFZ beneath the gravel plain sediments into the thermal anomaly area. Magnetic data within the gravel plain area suggest that both the DFZ and HFZ are characterized by low magnetic anomalies. The low magnetic anomalies result from weathering and alteration of ophiolites that characterize the geology of the study area.

Magnetic field techniques and filters such as upward continuation, Euler deconvolution and 2D magnetic modeling show that the source of the anomalies of both the DFZ and HFZ is not deeply seated (<1000 m) suggesting that they splay off the major transforms faults within the region.

Magnetic results of the Al Awir area (thermal anomaly area) failed to detect both the DFZ and HFZ beneath the thermal anomaly areas possibly due to the presence of the thick sand dunes (~ 50 m) or the absence of the ophiolite layers that are the main magnetic source rocks in the region.

The DFZ and HFZ are characterized by conductive anomalies on the AMT profiles. The conductive signature suggests the presence of fluids within the weathered fault zones. This interpretation is supported by the magnetic models and field observations of calcite precipitation within the fractures. The AMT show both the DFZ and HFZ extending into the thermal anomaly area.

The area of the thermal anomalies is highly fractured due to the intersection of the DFZ and HFZ. These fractures control and change the hydrological setting of the area, since they channel the groundwater from aquifers bounded by crystalline units (Ophiolite) to the surface of the thermal anomalies area, similar to artesian water conditions.

Rainfall events in the Hajar Mountains (recharge area) increase the pressure on the confined aquifers within the fractured ophiolite units that cause transient rise in the

water table level and raising the groundwater to shallower depths through the fractures resulting in the transient thermal anomalies. The thermal anomaly sensed by satellite images in 2003 matches the location of the DFZ characterized by AMT data within thermal anomalies area.

We conclude that the thermal anomalies are caused by the rainfall events in the recharge area since both areas are connected by DFZ and HFZ.

6.2. RECOMMENDATIONS AND FUTURE WORKS

The main limitation of this study is the shortage in the well log and water table monitoring. Therefore, it is highly recommended to include well information in the future studies to obtain aquifer parameters.

Higher resolution magnetic and AMT survey should be conducted to characterize DFZ and HFZ more precisely. Repeating AMT profiles within thermal anomalies area with smaller station spacing will help to understand how these DFZ and HFZ control the hydrology of the area. Groundwater flow models will help to determine transport of groundwater from mountains to discharge areas. Also, more detailed groundwater geochemistry can also help delineate and characterize the faults.

Fault zones have the capability to carry groundwater, therefore in arid regions the fractured zone areas have groundwater potential more than other areas, so locating these fault zones in the N. UAE will lead the to establish the agricultural areas along these zones.

The thermal anomaly area which is underlain by intersection of the DFZ and HFZ represents a potential source of groundwater that needs further investigation and could potentially serve as a major aquifer.

The seismicity of the N. UAE suggests that several earthquake events occurred in the last decade along the DFZ, HFZ and Ham fault zone trends. Most significant events were located on the trend of DFZ and HFZ (Figure 5.1). The location of these activities signifies that these fault zones are active. Therefore, locating these buried fault zones may help in earthquake mitigation studies. Also, it will help the decision makers to avoid these structures in urban planning.

APPENDICES

Appendix A: Acquisition Parameters

Table A.1 Acquisitions parameters of the Hattamagnetic survey

PARAMETER	DETAIL
Acquisition Parameters	
Survey Name	Hatta
Survey Type	Ground Magnetic Survey
Survey Starting Date	15-SEP-05 7:37:10PM
Survey Ending Date	05-OCT-05 3:54:10PM
Magnetic Inclination	39° 3'
Magnetic Declination	1° 29'
Elevation Datum	Sea Level
Coordinate Zone	Universal Transverse Mercator (UTM) 40N in meter
Survey Size	32.5 x 5 km
Survey Area	162 500 000 m
Line Spacing	500m
Reading Spacing	500m
Number of Readings	715
Number of Lines	66
Upper Left Corner Coordinate	386198E 2784433N
Upper Right Corner Coordinate	391200E 2784431N
Lower Left Corner Coordinate	381961E 2751930N
Lower Right Corner Coordinate	386974E 2751930N
Acquisition Direction	Bidirectional along x- axis
Starting Point	381961E 2751930N
Sensor's Distance to the Ground	800 cm
Acquisition Instruments	
Magnetometer	G-858 Magnetometer by Geometrics
Global Position System (GPS)	Handheld Receiver - GPSMAP 60CSx by Garmin
Acquisition Software	
MagMap 2000	Field Processing and Download the Data from Magnetometer
MapSource	Survey Design and Upload/Download the Coordinates

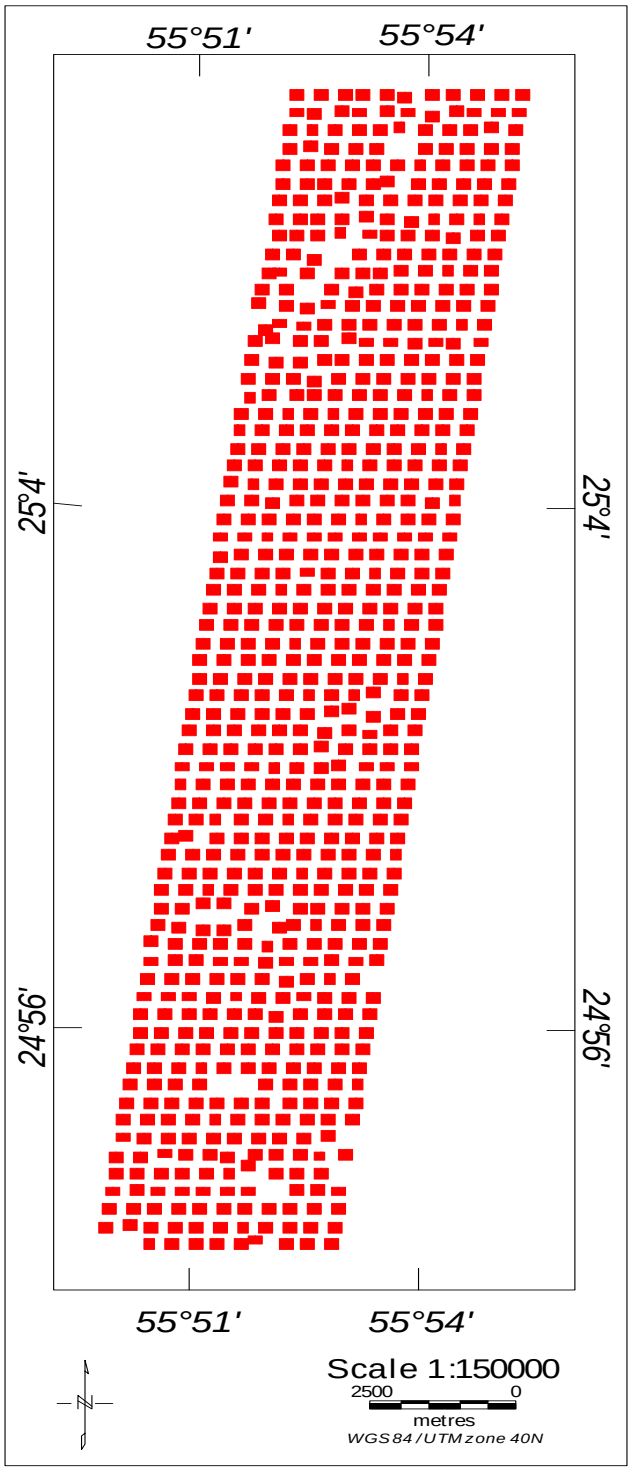

Figure A.1 Magnetic measuring points location of Hatta grid

Table A.2 Acquisitions parameters of the Dibbamagnetic survey

PARAMETER	DETAIL
Acquisition Parameters	
Survey Name	Dibba
Survey Type	Ground Magnetic Survey
Survey Starting Date	07-OCT-05 1:02:22PM
Survey Ending Date	02-NOV-05 3:32:00PM
Magnetic Inclination	39° 3'
Magnetic Declination	1° 29'
Elevation Datum	Sea Level
Coordinate Zone	Universal Transverse Mercator (UTM) 40N in meter
Survey Size	41 x 5 km
Survey Area	205 000 000 m^2
Line Spacing	500m
Reading Spacing	500m
Number of Readings	901
Number of Lines	83
Upper Left Corner Coordinate	392467E 2824934N
Upper Right Corner Coordinate	397464E 2824934N
Lower Left Corner Coordinate	392463E 2783932N
Lower Right Corner Coordinate	397463E 2783930N
Acquisition Direction	Bidirectional along x- axis
Starting Point	392463E 2783932N
Sensor's Distance to the Ground	800 cm
	800 cm
Acquisition Instruments	
Magnetometer	G-858 Magnetometer by Geometrics
Global Position System (GPS)	Handheld Receiver - GPSMAP 60CSx by Garmin
Acquisition Software	
MagMap 2000	Field Processing and Download the Data from Magnetometer
MapSource	Survey Design and Upload/Download the Coordinates

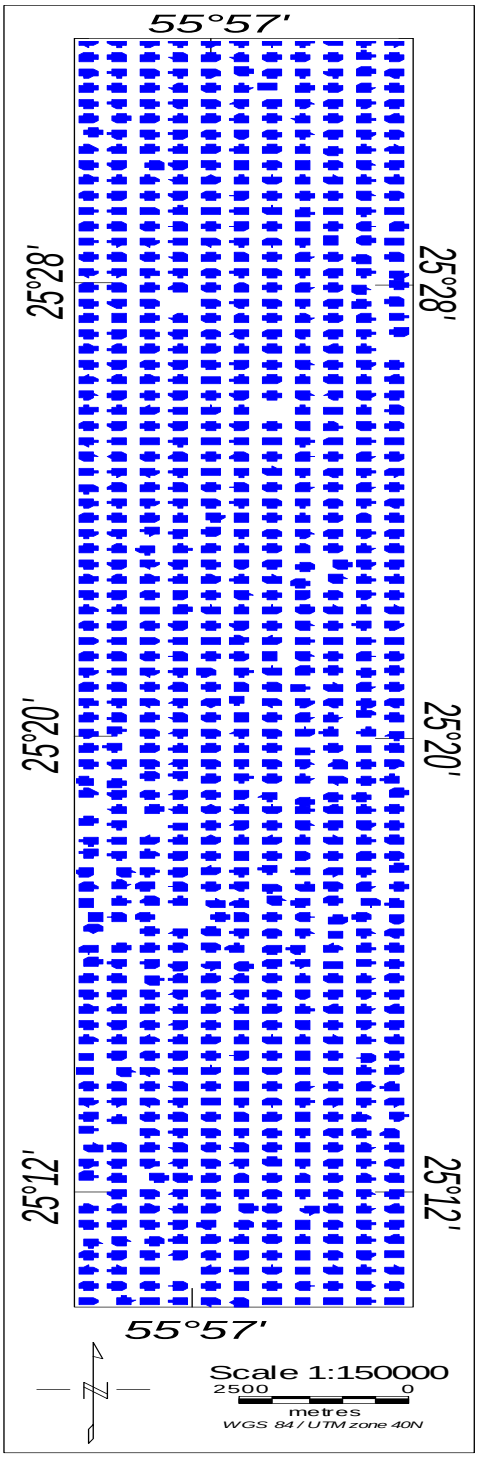

Figure A.2 Magnetic measuring points location of Dibba grid

Table A.3 Acquisitions parameters of the Awirmagnetic survey

PARAMETER	DETAIL
Acquisition Parameters	
Survey Name	Awir
Survey Type	Ground Magnetic Survey
Survey Starting Date	17-MAY-06 4:53:43PM
Survey Ending Date	05-JUN-06 2:49:54PM
Magnetic Inclination	39° 6'
Magnetic Declination	1° 31'
Elevation Datum	Sea Level
Coordinate Zone	Universal Transverse Mercator (UTM) 40N in meter
Survey Size	24 x 8 km
Survey Area	129 000 000 m^2
Line Spacing	500m
Reading Spacing	500m
Number of Readings	829
Number of Lines	49
Upper Left Corner Coordinate	360382E 2783498N
Upper Right Corner Coordinate	368380E 2783501N
Lower Left Corner Coordinate	360378E 2759498N
Lower Right Corner Coordinate	368383E 2759499N
Acquisition Direction	Bidirectional along x- axis
Starting Point	360382E 2783498N
Sensor's Distance to the Ground	800 cm
Acquisition Instruments	
Magnetometer	G-858 Magnetometer by Geometrics
Global Position System (GPS)	Handheld Receiver - GPSMAP 60CSx by Garmin
Acquisition Software	
MagMap 2000	Field Processing and Download the Data from Magnetometer
MapSource	Survey Design and Upload/Download the Coordinates

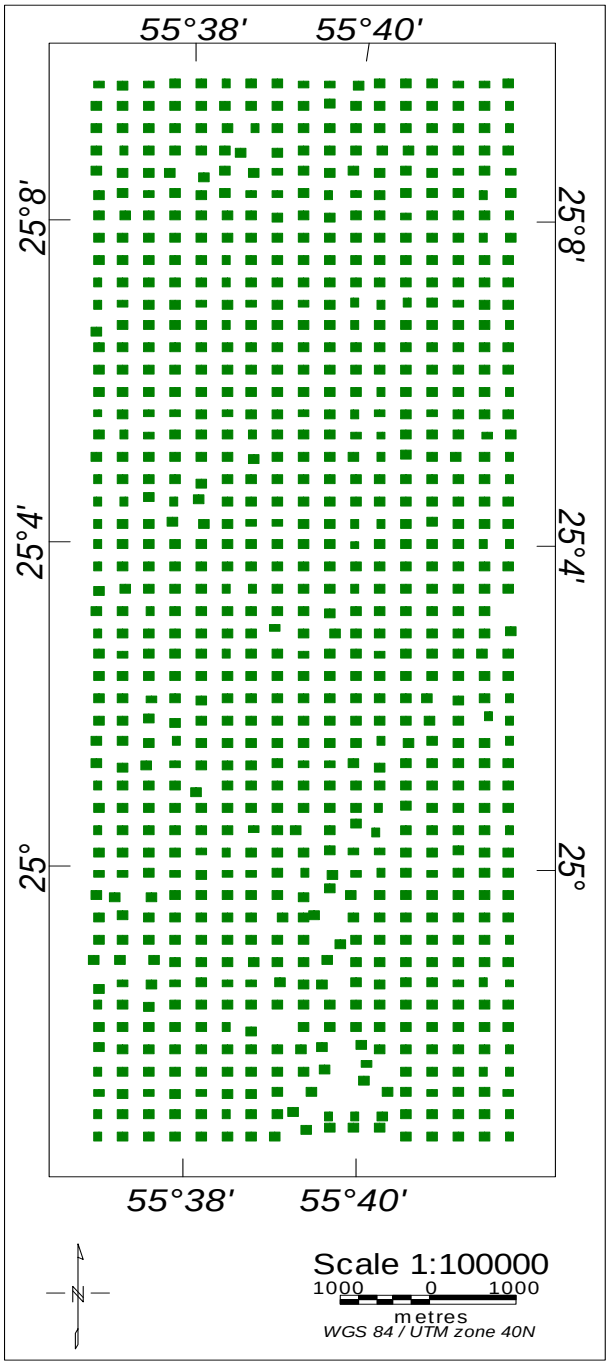

Figure A.3 Magnetic measuring points location of Awir grid

Table A.4 Acquisitions parameters of the Dibba profile (D), CSAMT survey

Acquisition Parameters	Details
Survey Name	**Dibba (Profile)**
Survey Type	Control Source Audiomagnetotelluric
Survey Starting Date	29-APR-07 6:06:30AM
Survey Ending Date	06-MAY-07 11:31:56PM
Elevation Datum	Sea Level
Coordinate Zone	Universal Transverse Mercator (UTM) 40N in meter
Number of Profiles	1
Profile's Length	12500 m
Number of Sounding/ Profile	19
Sounding Spacing	500 - 1000 m
Starting Point	399692E 2798000N
Ending Point	387214E 2802877N
Electrode Spacing in Each Direction	50 m
Distance from Receiver to Transmitter	250m

Table A.5 Acquisitions parameters of the Bahayis profile (B), CSAMT survey

Acquisition Parameters	Details
Survey Name	**Bahayis (Profile)**
Survey Type	Control Source Audiomagnetotelluric
Survey Starting Date	12-MAY-07 5:45:12AM
Survey Ending Date	16-MAY-07 10:23:56PM
Elevation Datum	Sea Level
Coordinate Zone	Universal Transverse Mercator (UTM) 40N in meter
Number of Profiles	1
Profile's Length	20000 m
Number of Sounding/ Profile	21
Sounding Spacing	1000 m
Starting Point	397293E 2780710N
Ending Point	381421E 2791122N
Electrode Spacing in Each Direction	50 m
Distance from Receiver to Transmitter	250m

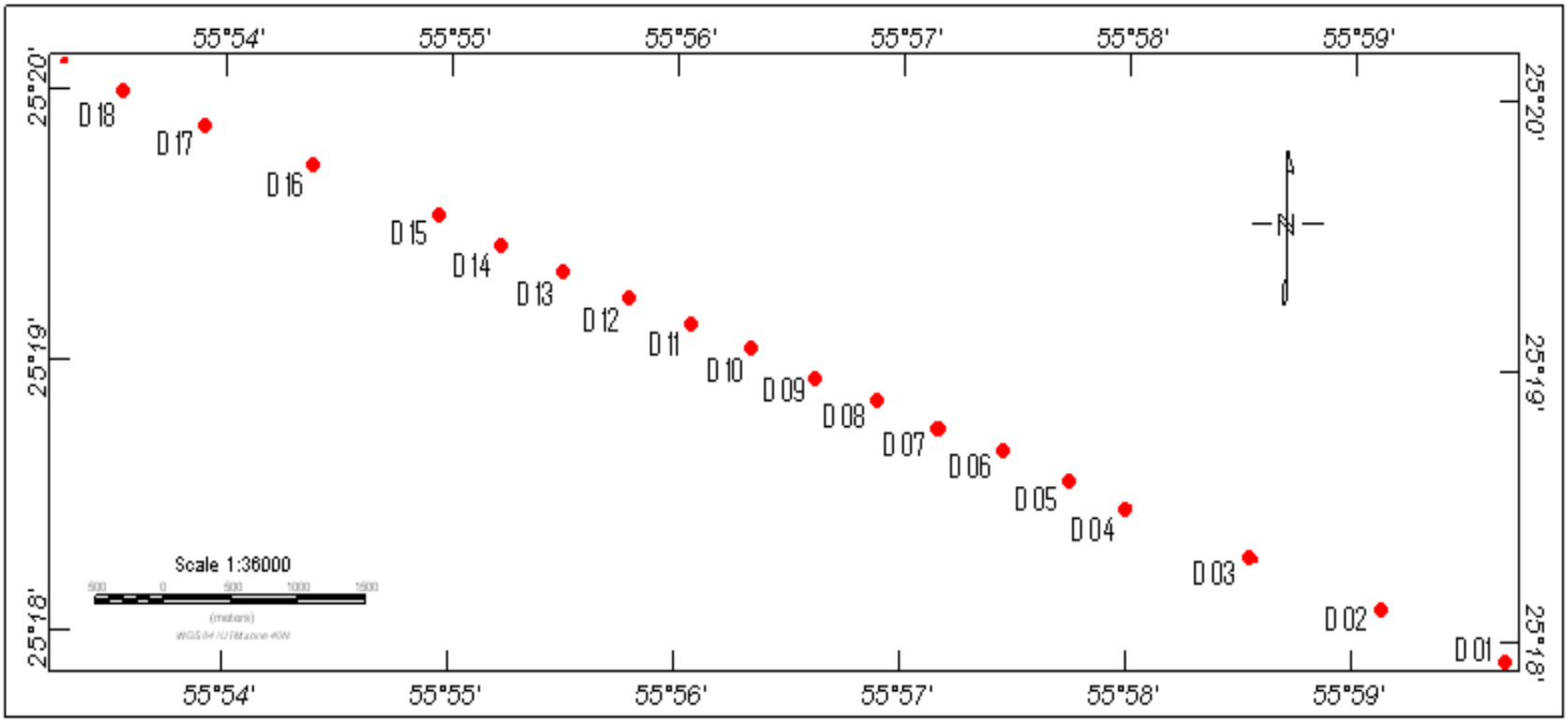

Figure A.4 Measuring points of the Dibba profile (D), CSAMT survey

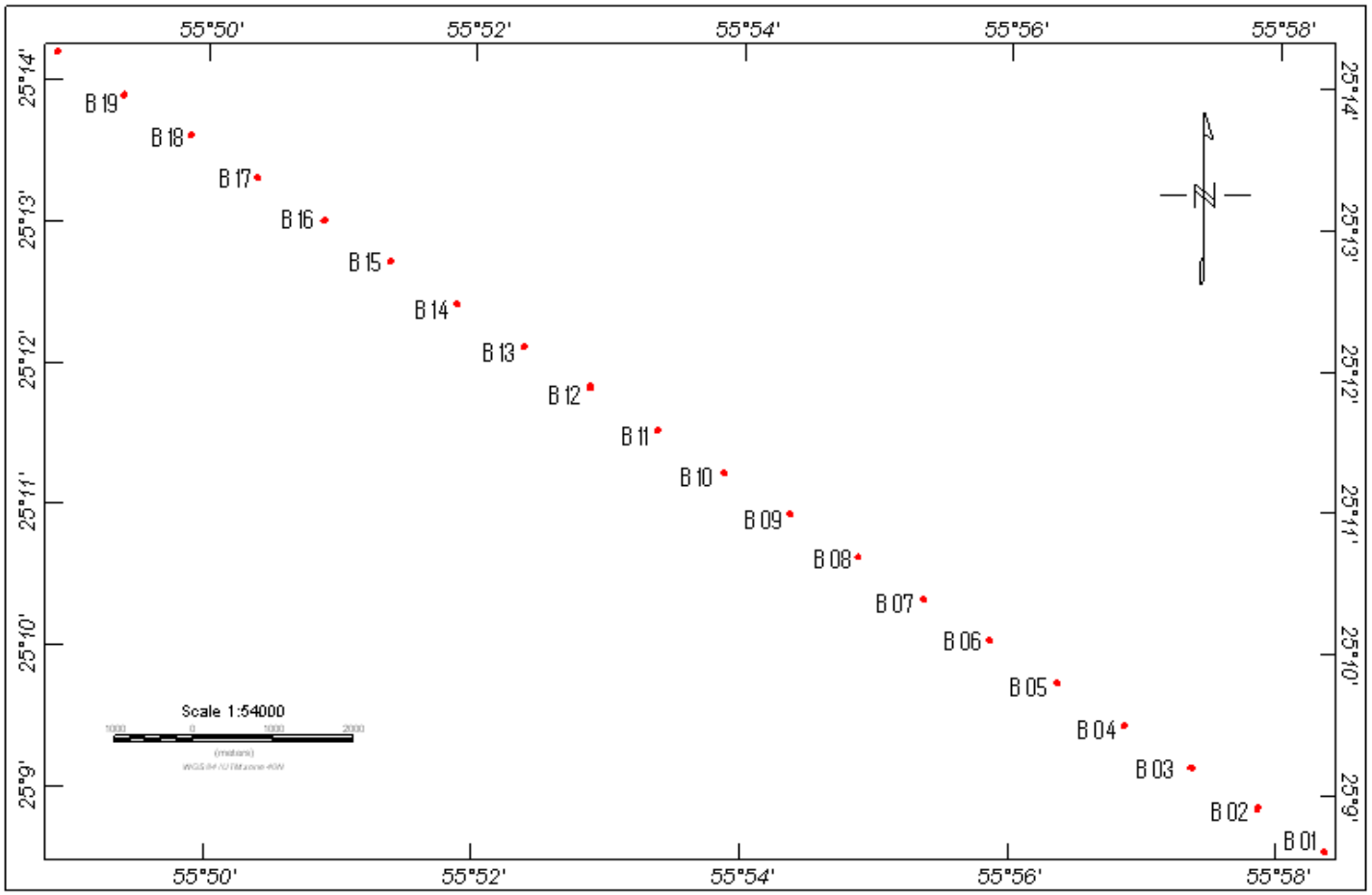

Figure A.5 Measuring points of the Bahayis profile (B), CSAMT survey

Table A.5 Acquisitions parameters of the Bahayis profile (B), CSAMT survey

Acquisition Parameters	Details
Survey Name	**Bahayis (Profile)**
Survey Type	Control Source Audiomagnetotelluric
Survey Starting Date	12-MAY-07 5:45:12AM
Survey Ending Date	16-MAY-07 10:23:56PM
Elevation Datum	Sea Level
Coordinate Zone	Universal Transverse Mercator (UTM) 40N in meter
Number of Profiles	1
Profile's Length	20000 m
Number of Sounding/ Profile	21
Sounding Spacing	1000 m
Starting Point	397293E 2780710N
Ending Point	381421E 2791122N
Electrode Spacing in Each Direction	50 m
Distance from Receiver to Transmitter	250m

Table A.6 Acquisitions parameters of the Hatta profile (H), CSAMT survey

Acquisition Parameters	Details
Survey Name	**Hatta (Profile)**
Survey Type	Control Source Audiomagnetotelluric
Survey Starting Date	28-APR-07 11:13:29AM
Survey Ending Date	26-APR-07 6:20:12AM
Elevation Datum	Sea Level
Coordinate Zone	Universal Transverse Mercator (UTM) 40N in meter
Number of Profiles	1
Profile's Length	15000 m
Number of Sounding/ Profile	21
Sounding Spacing	500-1000 m
Starting Point	388012E 2766131N
Ending Point	378988E 2754123N
Electrode Spacing in Each Direction	50 m
Distance from Receiver to Transmitter	250m

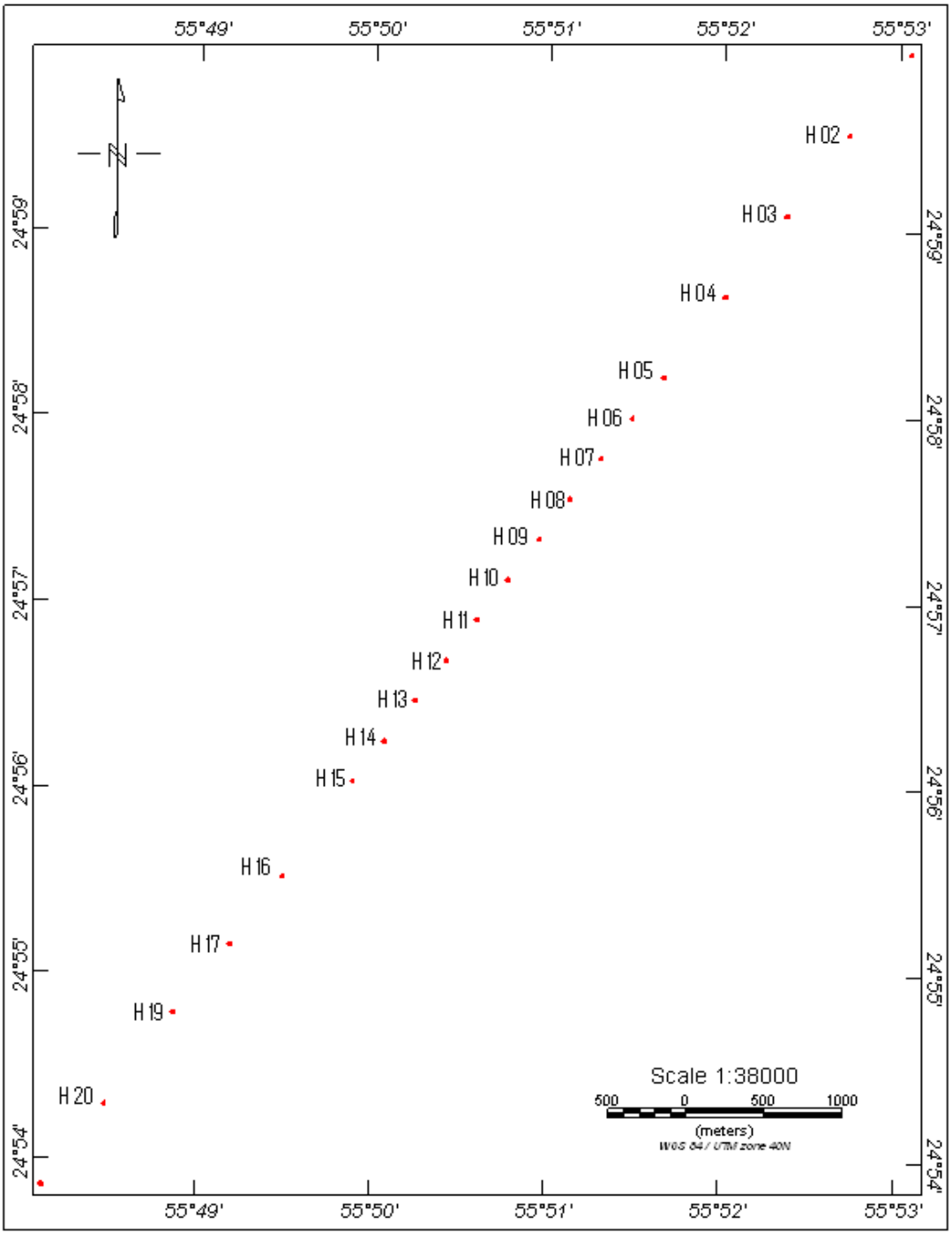

Figure A.6 Measuring points of the Hatta profile (H), CSAMT survey

Table A.7 Acquisitions parameters of the thermal anomaliesarea, CSAMT survey

Acquisition Parameters	Details
Survey Name	**Thermal Anomalies Area**
Survey Type	Control Source Audiomagnetotelluric
Survey Starting Date	26-MAR-07 8:18:31AM
Survey Ending Date	16-APR-07 11:37:01AM
Elevation Datum	Sea Level
Coordinate Zone	Universal Transverse Mercator (UTM) 40N in meter
Survey Size	40 x 30 km
Survey Area	120 000 000 00 m
Number of Profiles	7
Number of Sounding/ Profile	9
Line Spacing	5 km
Sounding Spacing	5 km
Starting Point	392309E 2764713N
Ending Point	342147E 2764651N
Electrode Spacing in Each Direction	50 m
Distance from Receiver to Transmitter	250m

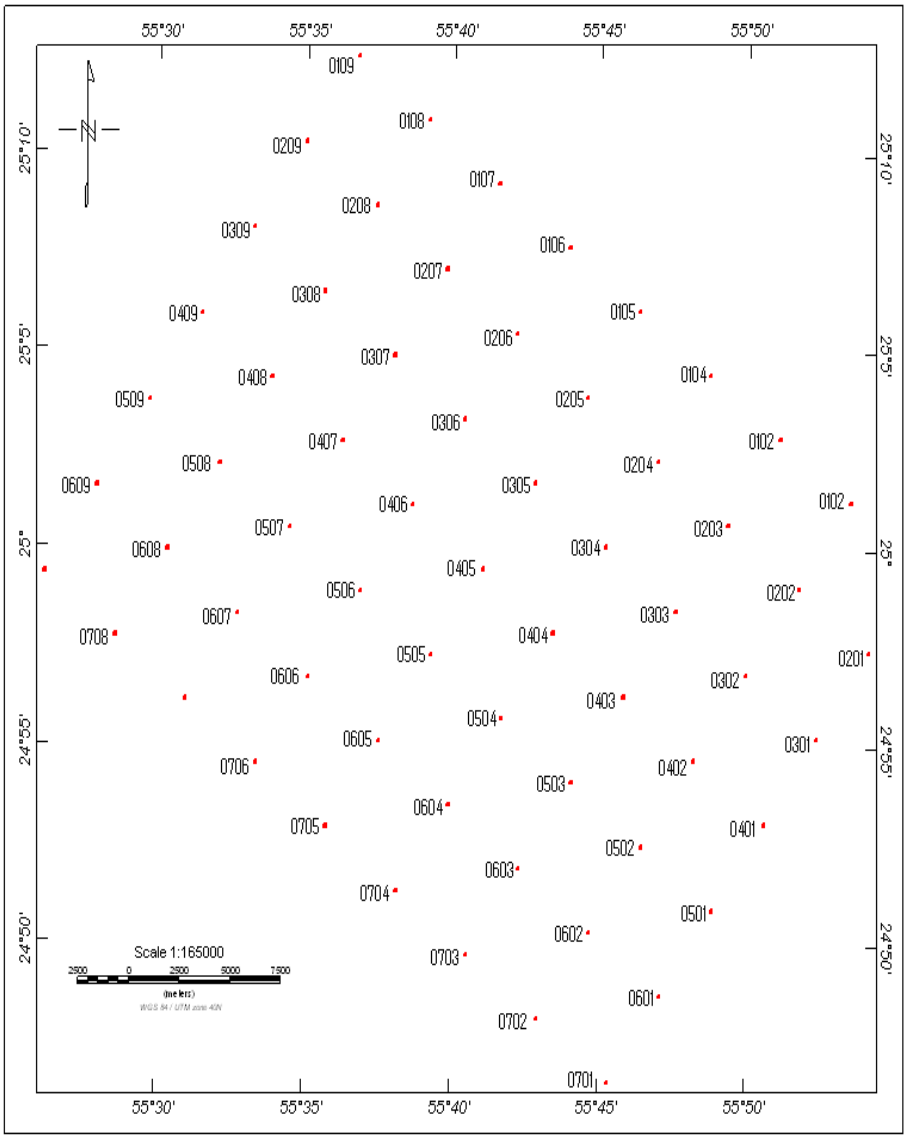

Figure A.7 CSAMT measuring points location of thermal anomalies area

Figure A.8 Images of the field work, A) Magnetic survey, B) Transmitter (CSAMT Survey) C) Magnetometer coil (CSAMT Survey) D) Electrode (CSAMT Survey) E) Operating console (CSAMT) F) General layout during the operation.

Appendix B: Dataset (Sounding Curves)

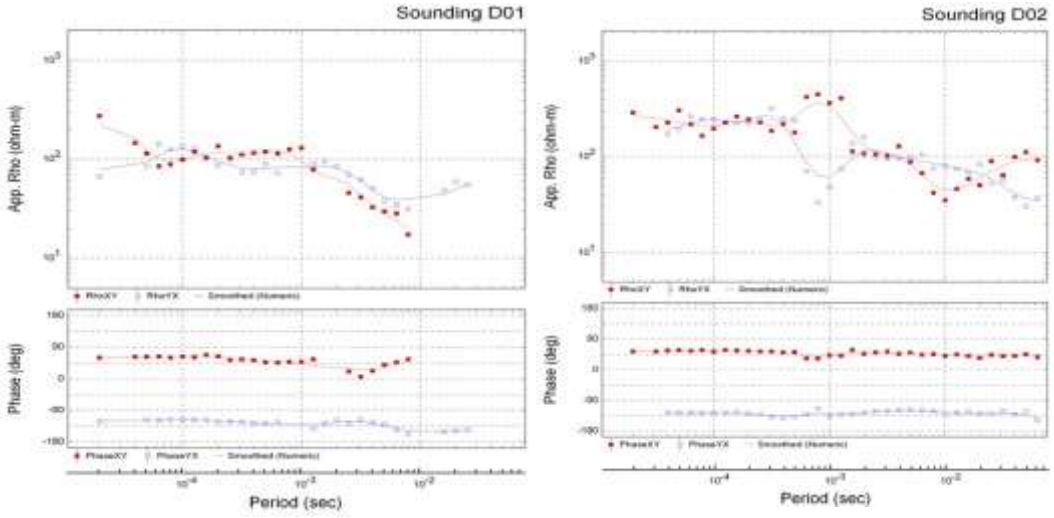
Sounding D01
App. Rho (ohm-m)
Phase (deg)
Period (sec)

Sounding D02
App. Rho (ohm-m)
Phase (deg)
Period (sec)

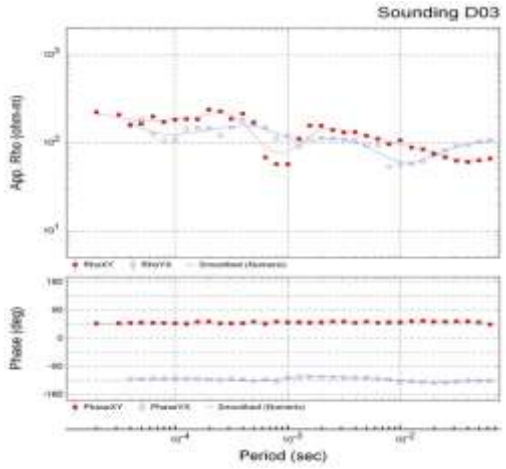
Sounding D03
App. Rho (ohm-m)
Phase (deg)
Period (sec)

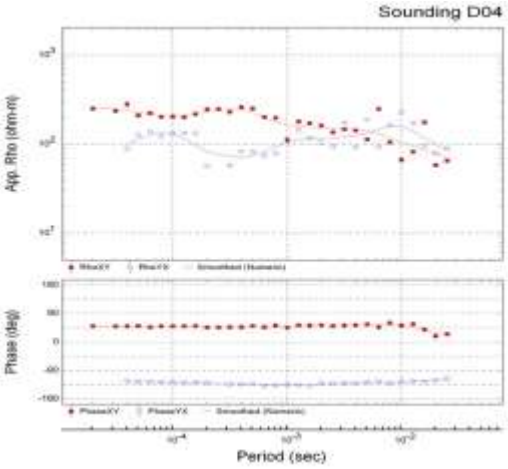
Sounding D04
App. Rho (ohm-m)
Phase (deg)
Period (sec)

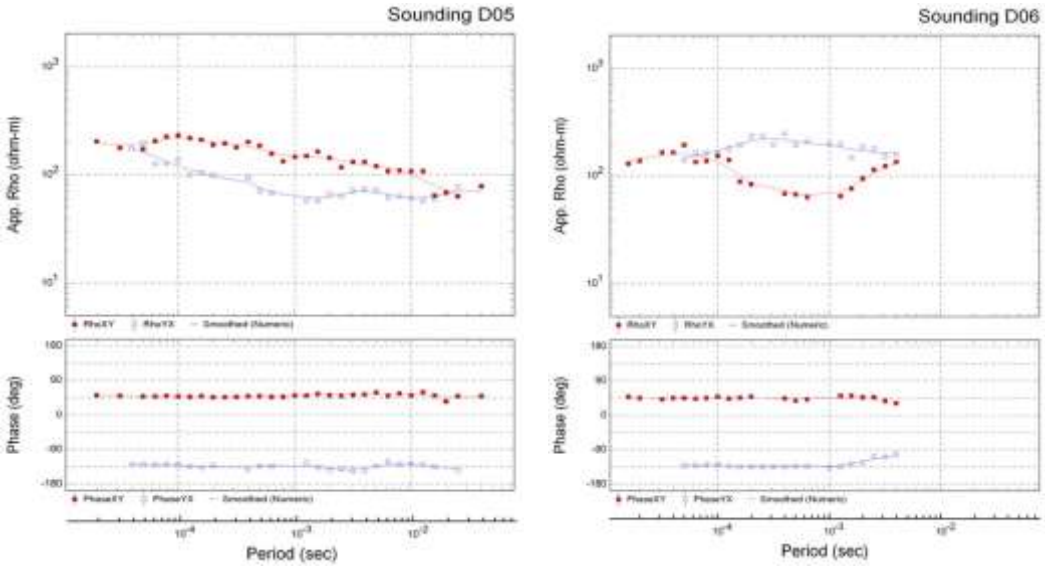
Sounding D05
App. Rho (ohm-mi)
Phase (deg)
Period (sec)

Sounding D06
App. Rho (ohm-mi)
Phase (deg)
Period (sec)

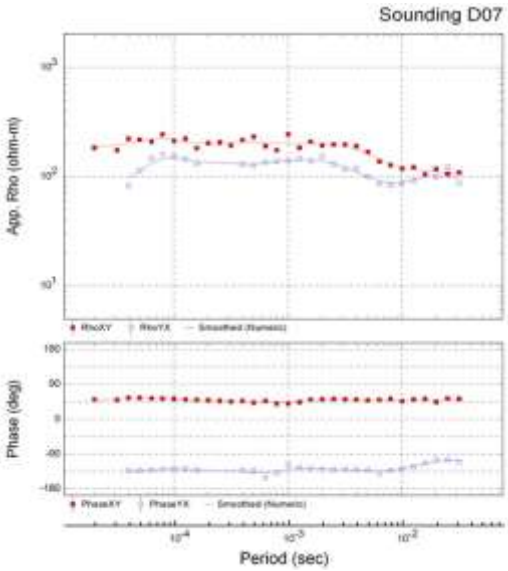
Sounding D07
App. Rho (ohm-mi)
Phase (deg)
Period (sec)

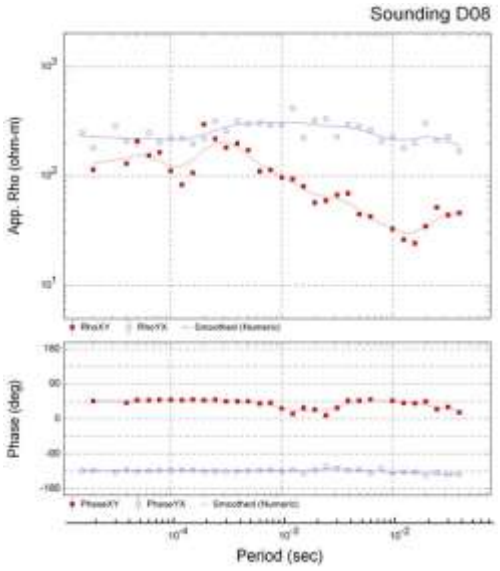
Sounding D08
App. Rho (ohm-mi)
Phase (deg)
Period (sec)

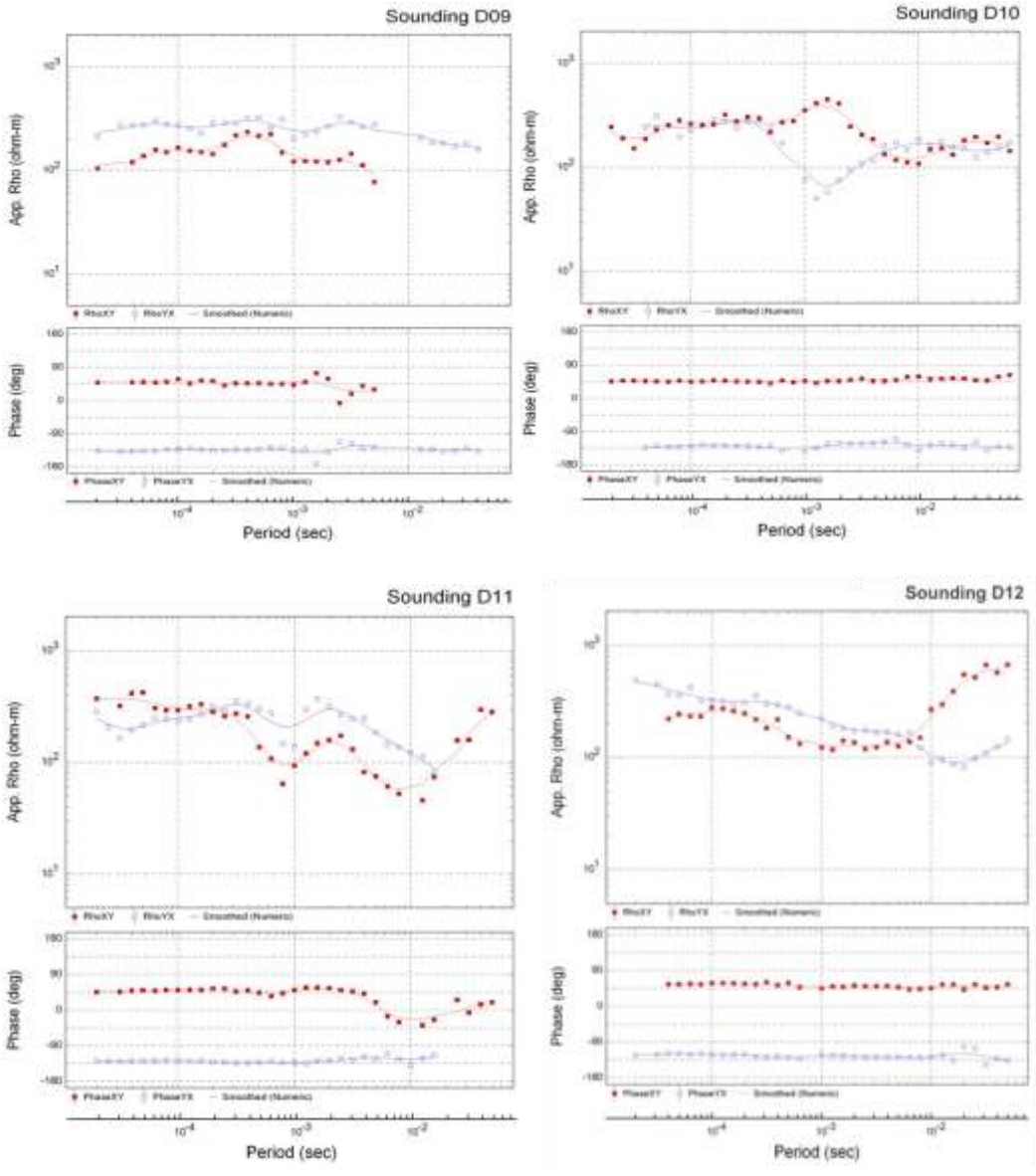
Sounding D09
Sounding D10
Sounding D11
Sounding D12
App. Rho (ohm-m)
Phase (deg)
Period (sec)

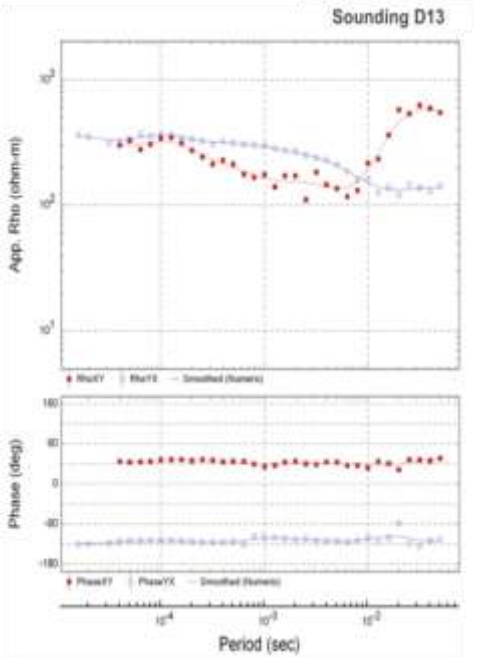
Sounding D13
App. Rho (ohm-m)
Phase (deg)
Period (sec)

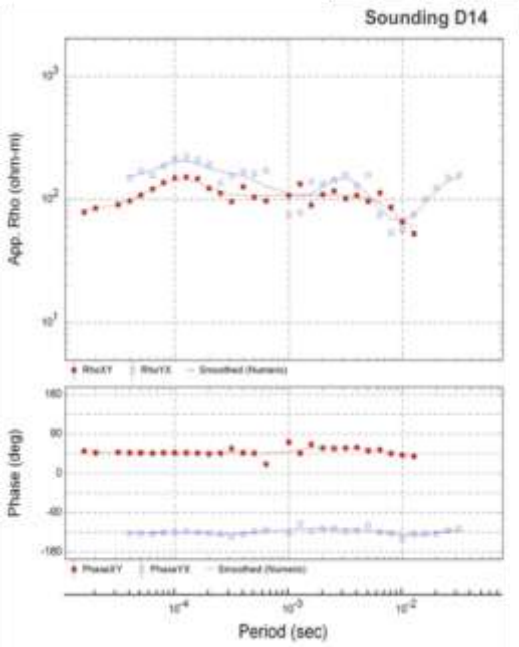
Sounding D14
App. Rho (ohm-m)
Phase (deg)
Period (sec)

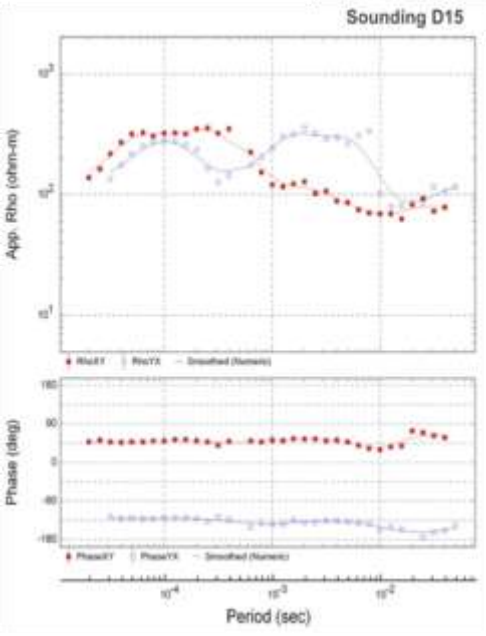
Sounding D15
App. Rho (ohm-m)
Phase (deg)
Period (sec)

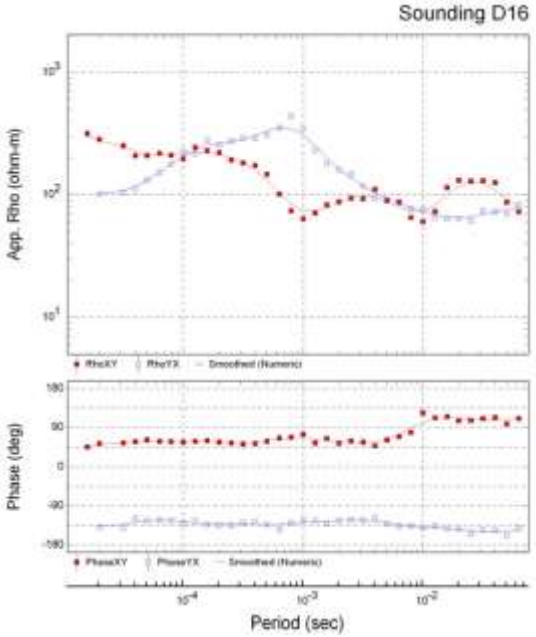
Sounding D16
App. Rho (ohm-m)
Phase (deg)
Period (sec)

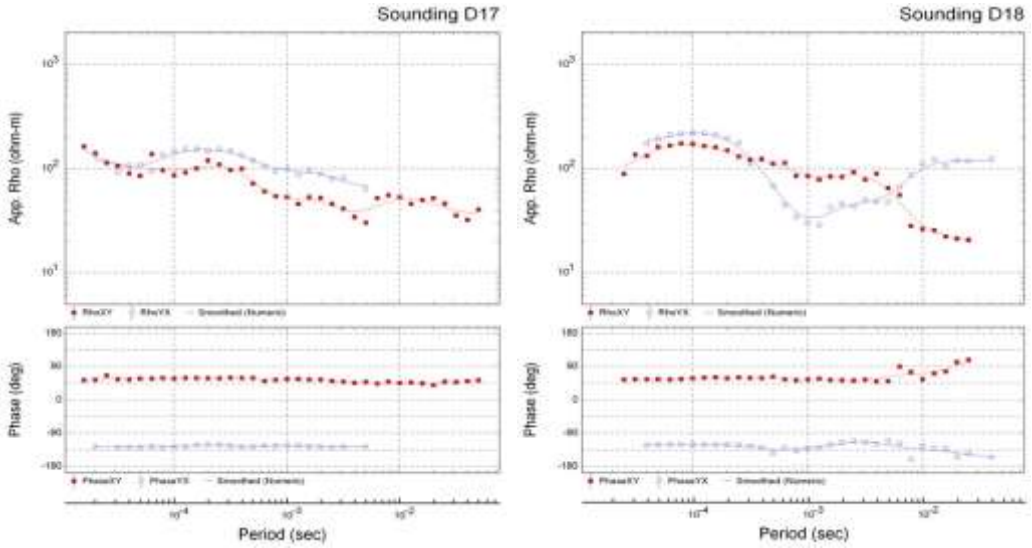
Sounding D17
Sounding D18
App. Rho (ohm-m)
Phase (deg)
Period (sec)

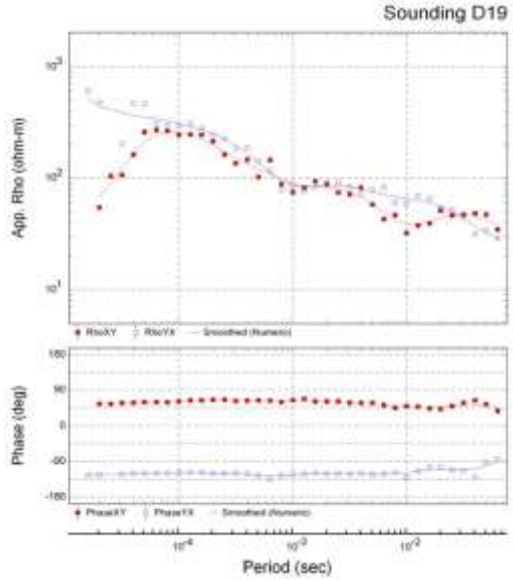
Sounding D19
App. Rho (ohm-m)
Phase (deg)
Period (sec)

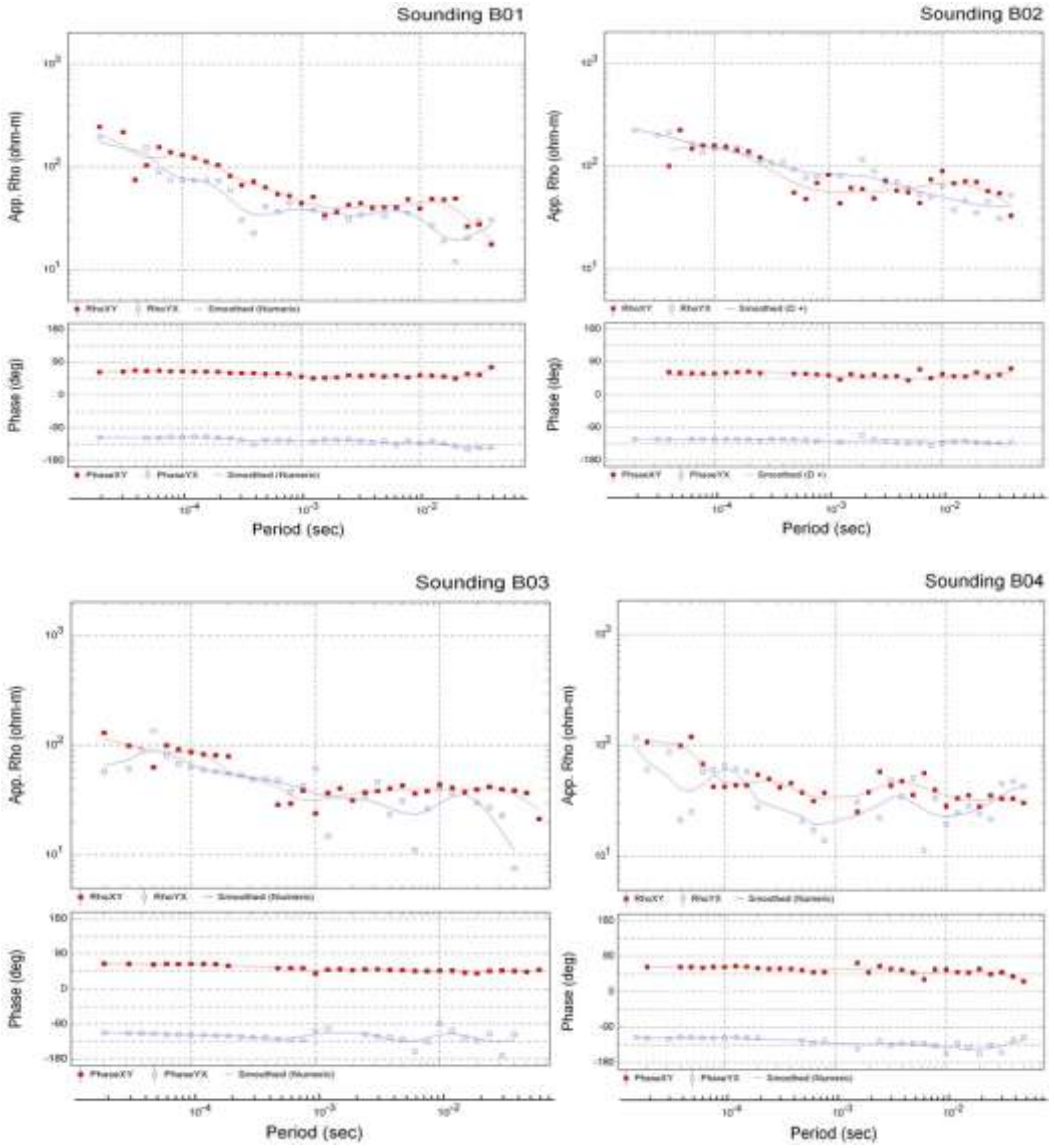
Sounding B01
Sounding B02
Sounding B03
Sounding B04
App. Rho (ohm-m)
Phase (deg)
Period (sec)

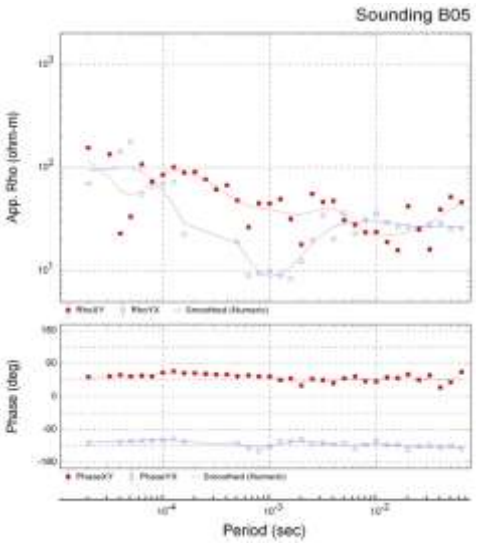
Sounding B05
App. Rho (ohm-m)
Phase (deg)
Period (sec)

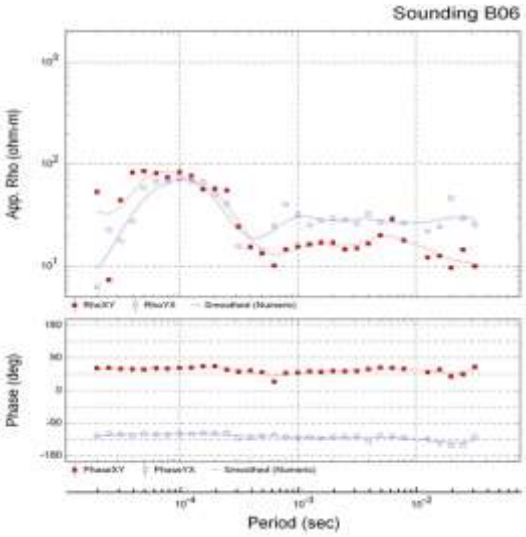
Sounding B06
App. Rho (ohm-m)
Phase (deg)
Period (sec)

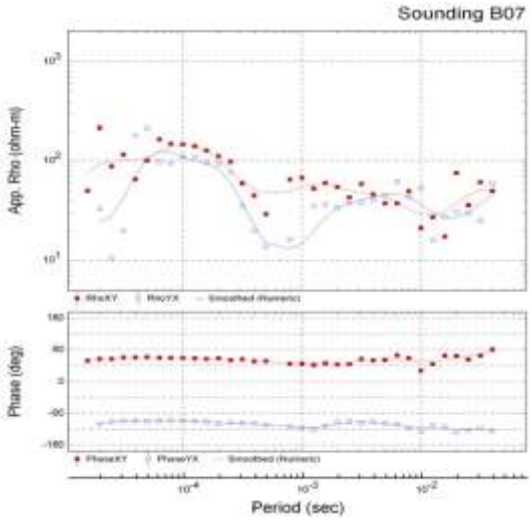
Sounding B07
App. Rho (ohm-m)
Phase (deg)
Period (sec)

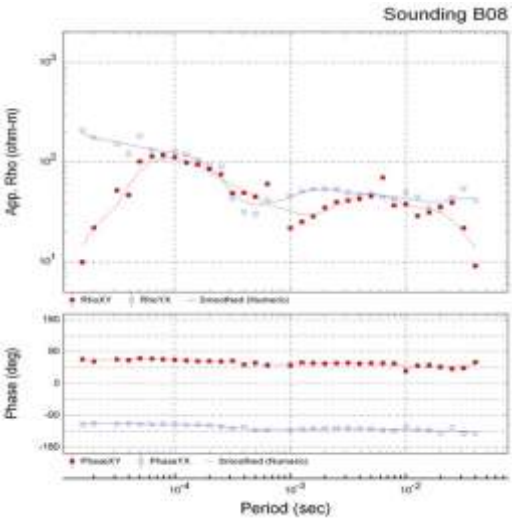
Sounding B08
App. Rho (ohm-m)
Phase (deg)
Period (sec)

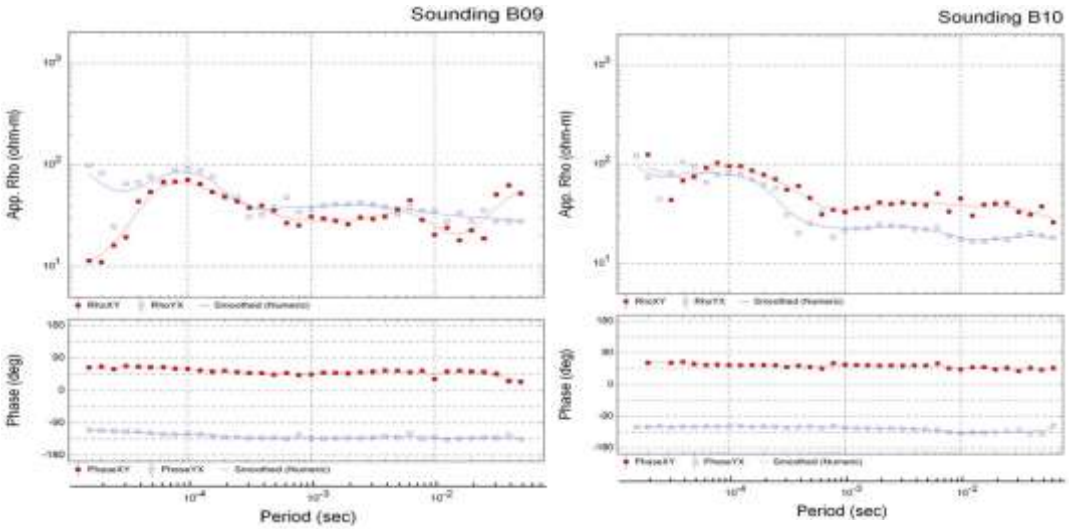
Sounding B09
App. Rho (ohm-m)
Phase (deg)
Period (sec)

Sounding B10
App. Rho (ohm-m)
Phase (deg)
Period (sec)

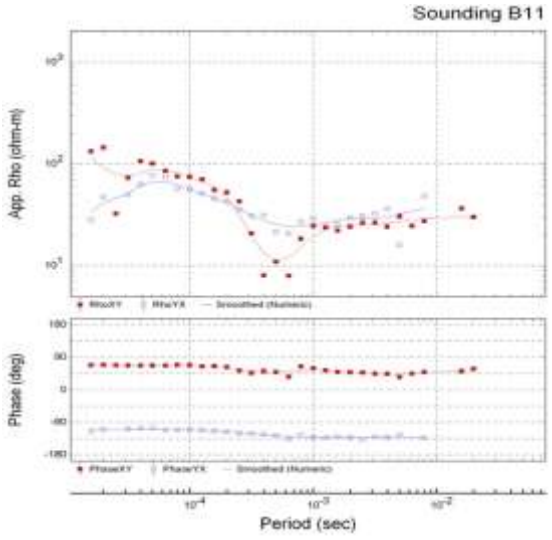
Sounding B11
App. Rho (ohm-m)
Phase (deg)
Period (sec)

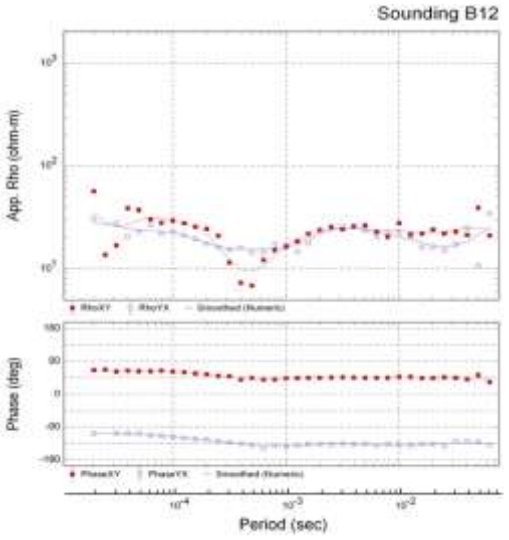
Sounding B12
App. Rho (ohm-m)
Phase (deg)
Period (sec)

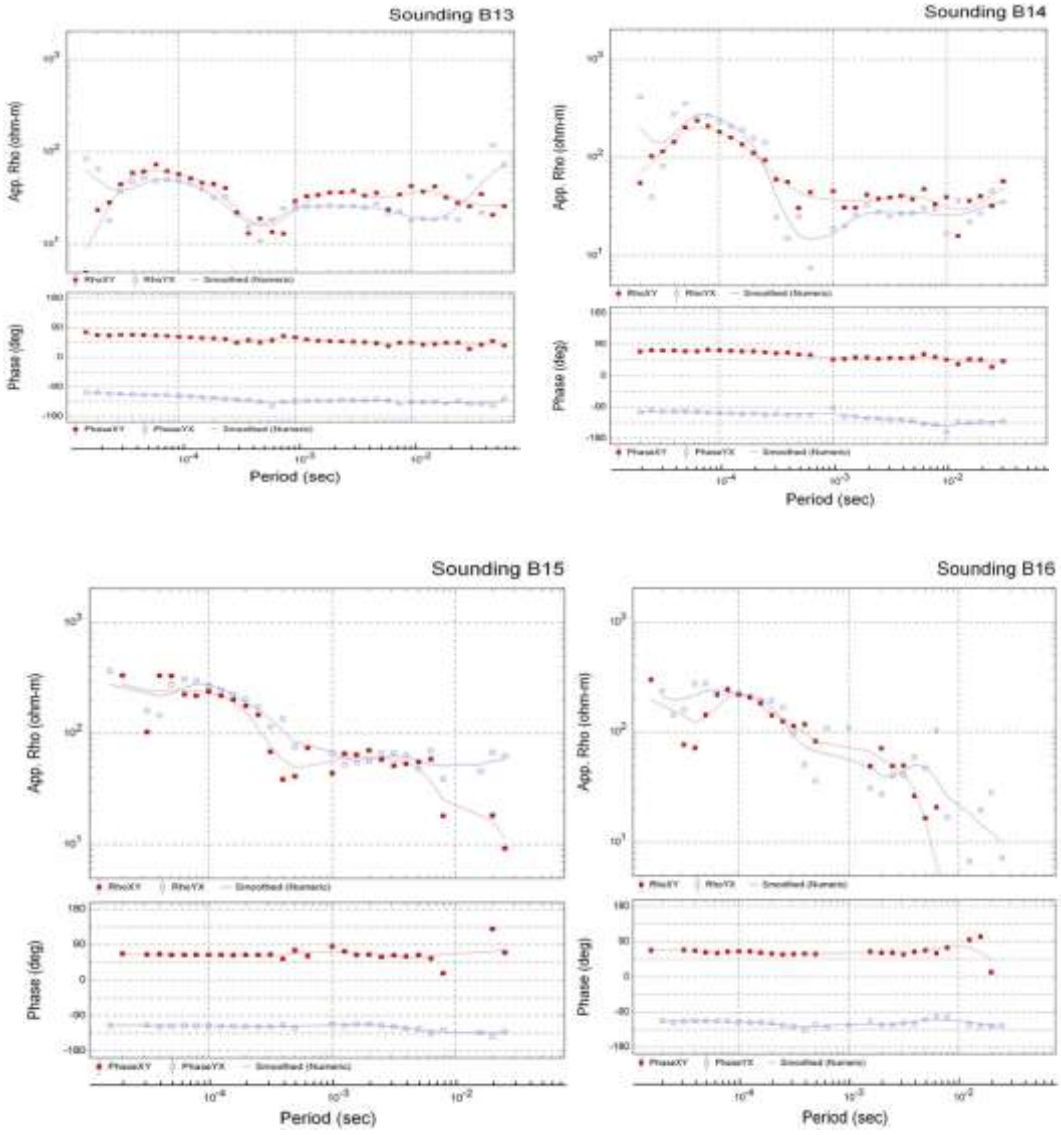
Sounding B13
App. Rho (ohm-m)
Phase (deg)
Period (sec)
Sounding B14
App. Rho (ohm-m)
Phase (deg)
Period (sec)
Sounding B15
App. Rho (ohm-m)
Phase (deg)
Period (sec)
Sounding B16
App. Rho (ohm-m)
Phase (deg)
Period (sec)

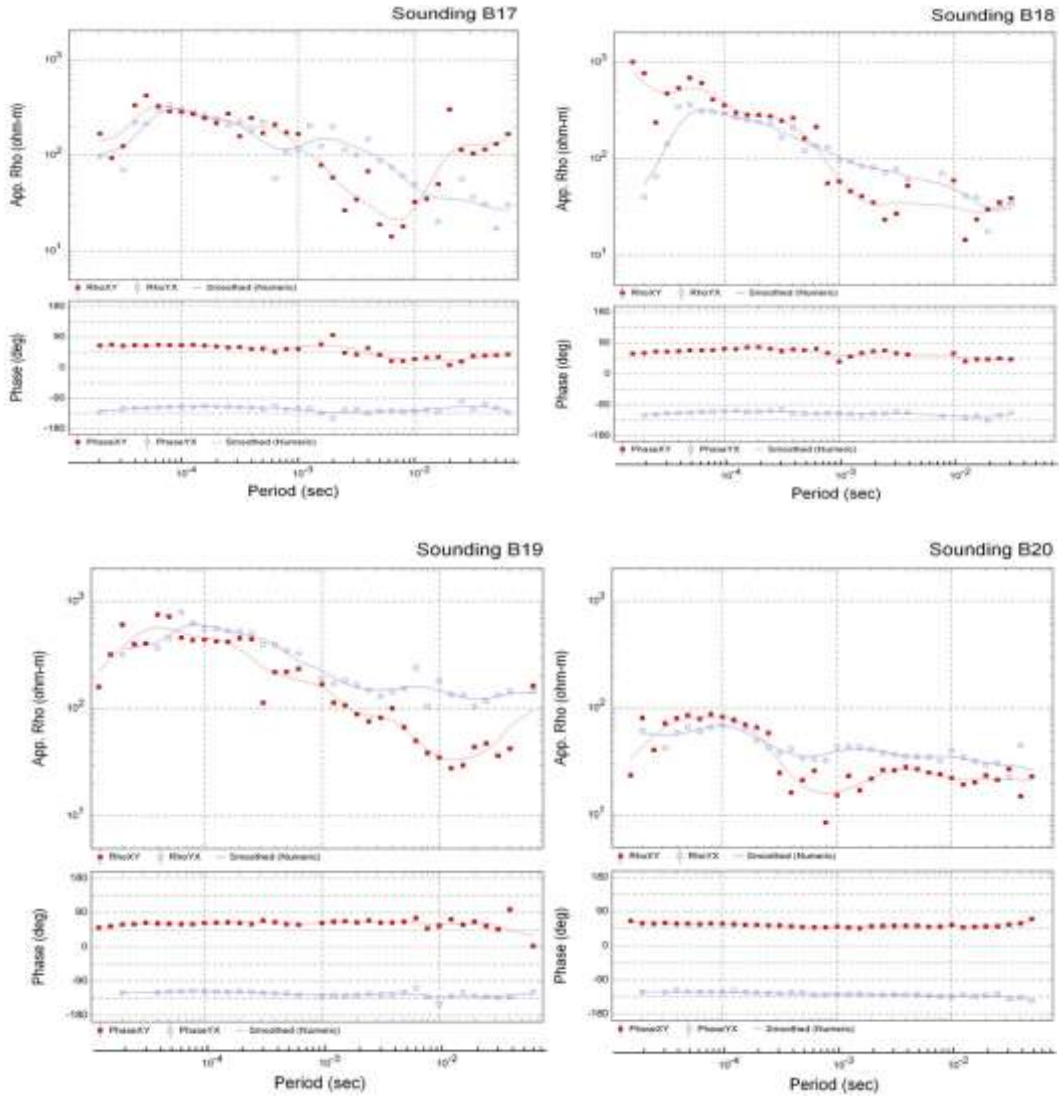
Sounding B17
App. Rho (ohm-m)
Phase (deg)
Period (sec)
Sounding B18
App. Rho (ohm-m)
Phase (deg)
Period (sec)
Sounding B19
App. Rho (ohm-m)
Phase (deg)
Period (sec)
Sounding B20
App. Rho (ohm-m)
Phase (deg)
Period (sec)

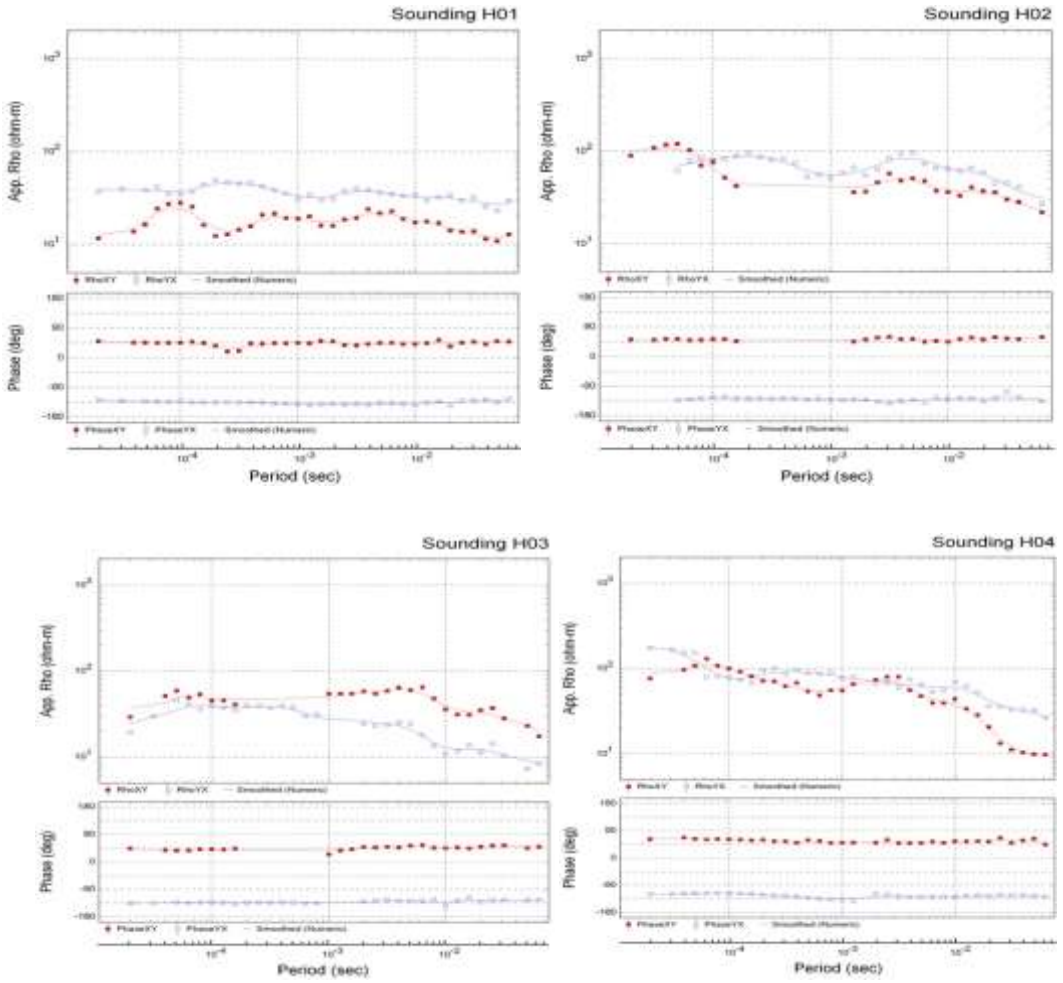
Sounding H01
Sounding H02
Sounding H03
Sounding H04
App. Rho (ohm-m)
Phase (deg)
Period (sec)

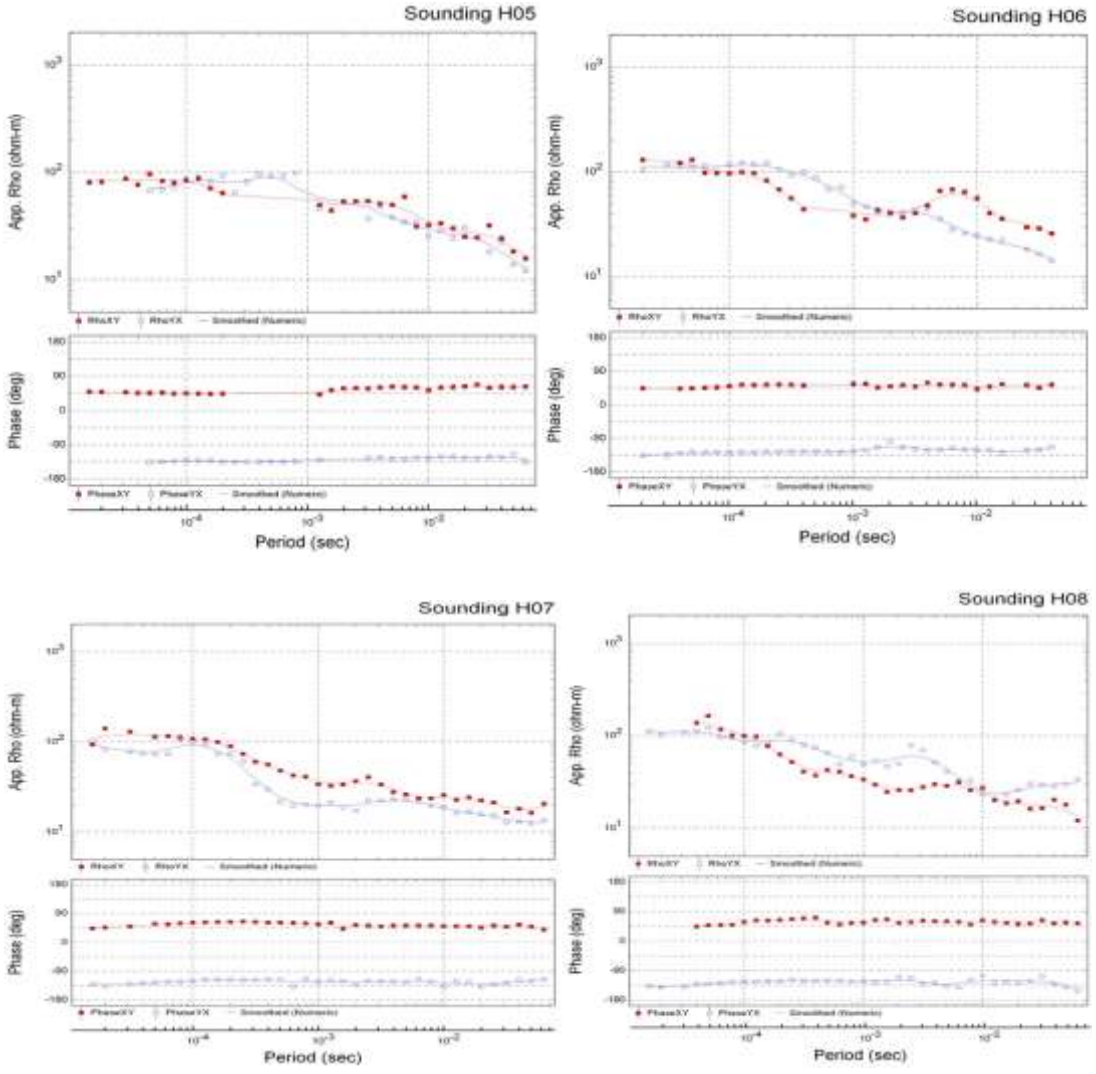
Sounding H05
App. Rho (ohm-m)
Phase (deg)
Period (sec)
Sounding H06
App. Rho (ohm-m)
Phase (deg)
Period (sec)
Sounding H07
App. Rho (ohm-m)
Phase (deg)
Period (sec)
Sounding H08
App. Rho (ohm-m)
Phase (deg)
Period (sec)

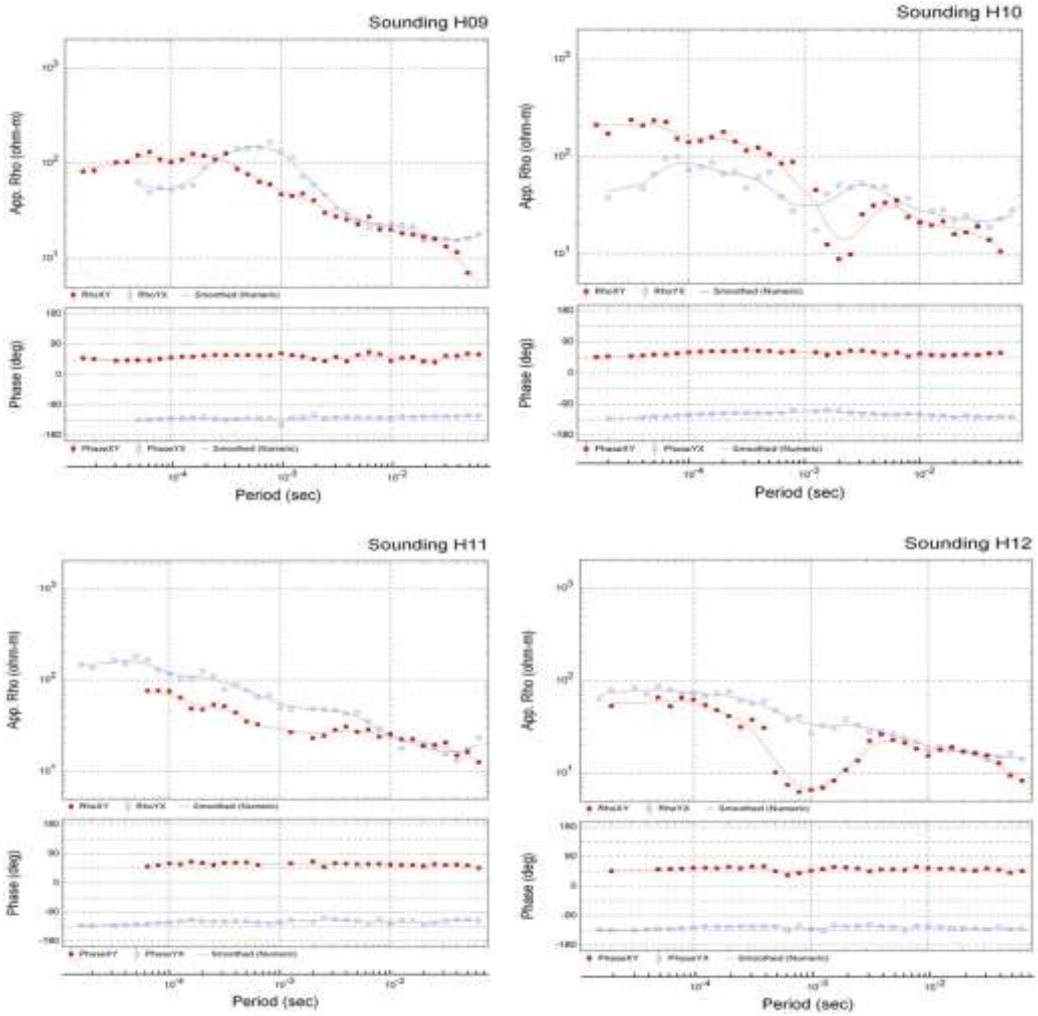
Sounding H09
Sounding H10
Sounding H11
Sounding H12
App. Rho (ohm-m)
Phase (deg)
Period (sec)

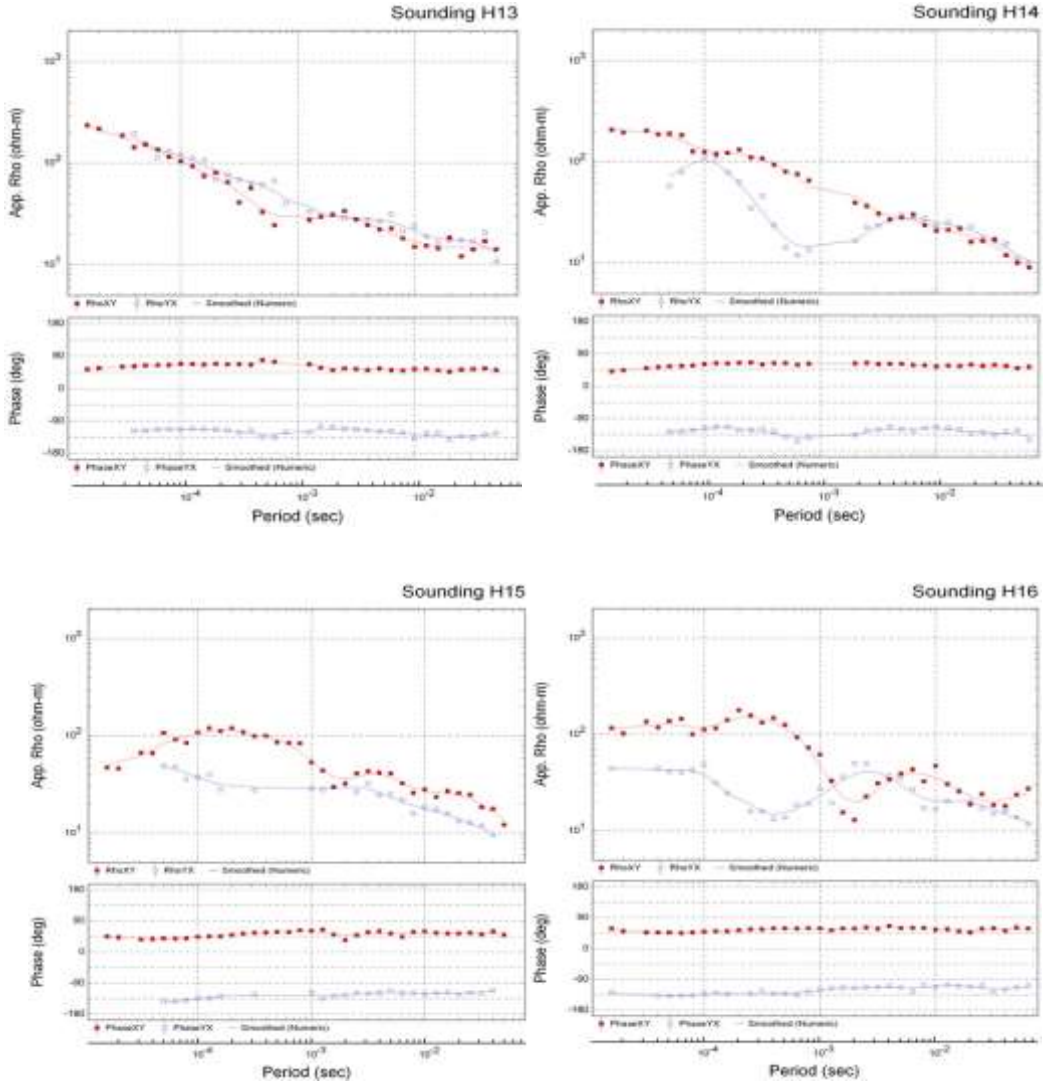
Sounding H13
Sounding H14
Sounding H15
Sounding H16
App. Rho (ohm-m)
Phase (deg)
Period (sec)

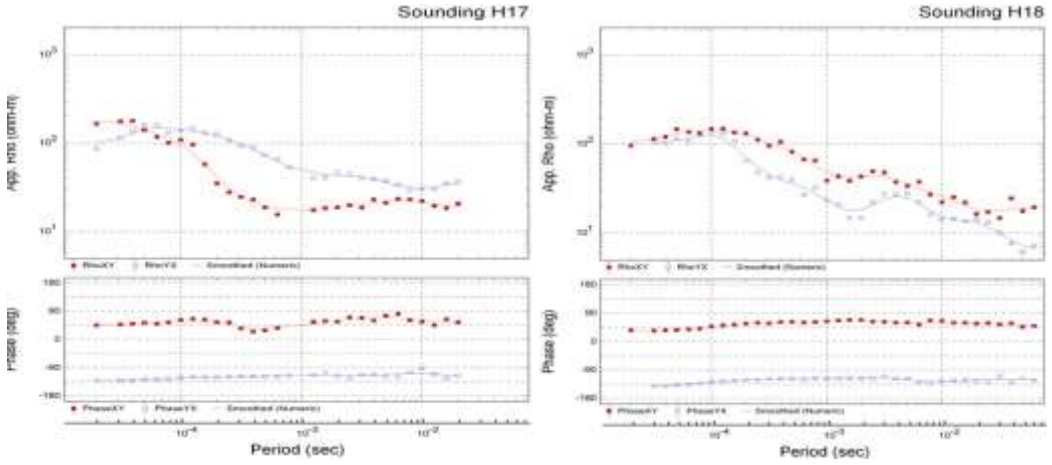
Sounding H17
Sounding H18
Period (sec)
Period (sec)

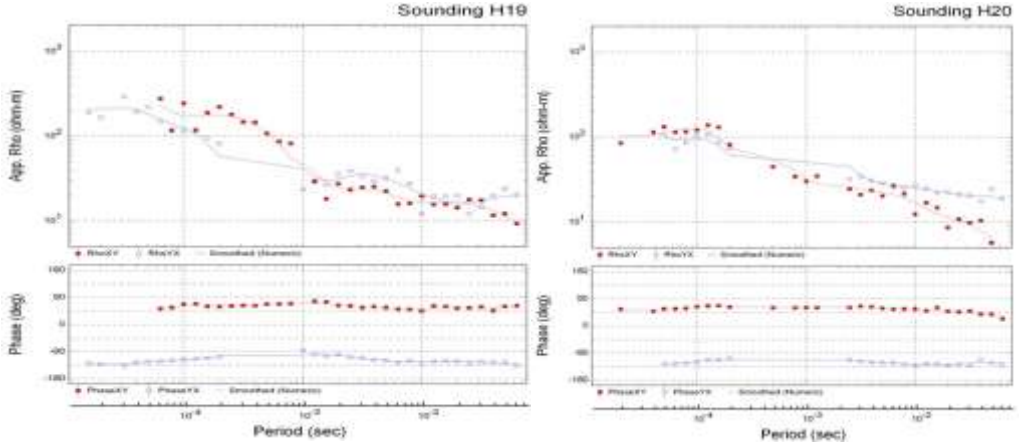
Sounding H19
Sounding H20
Period (sec)
Period (sec)

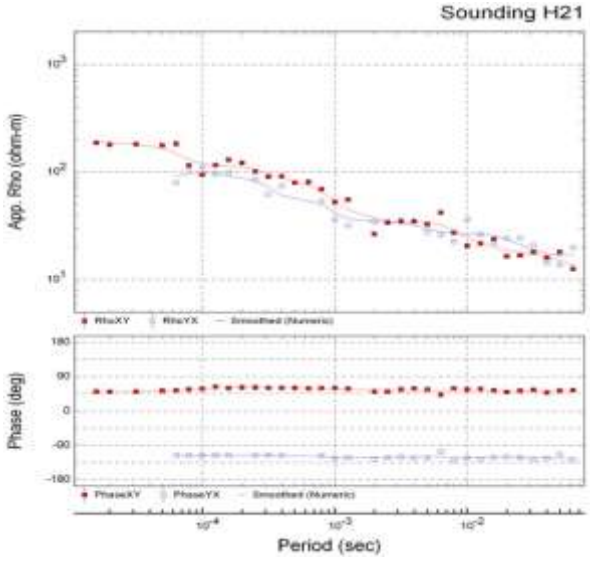
Sounding H21
App. Rho (ohm-m)
RhoXY
RhoYX
Smoothed (Numeric)
Phase (deg)
PhaseXY
PhaseYX
Smoothed (Numeric)
Period (sec)

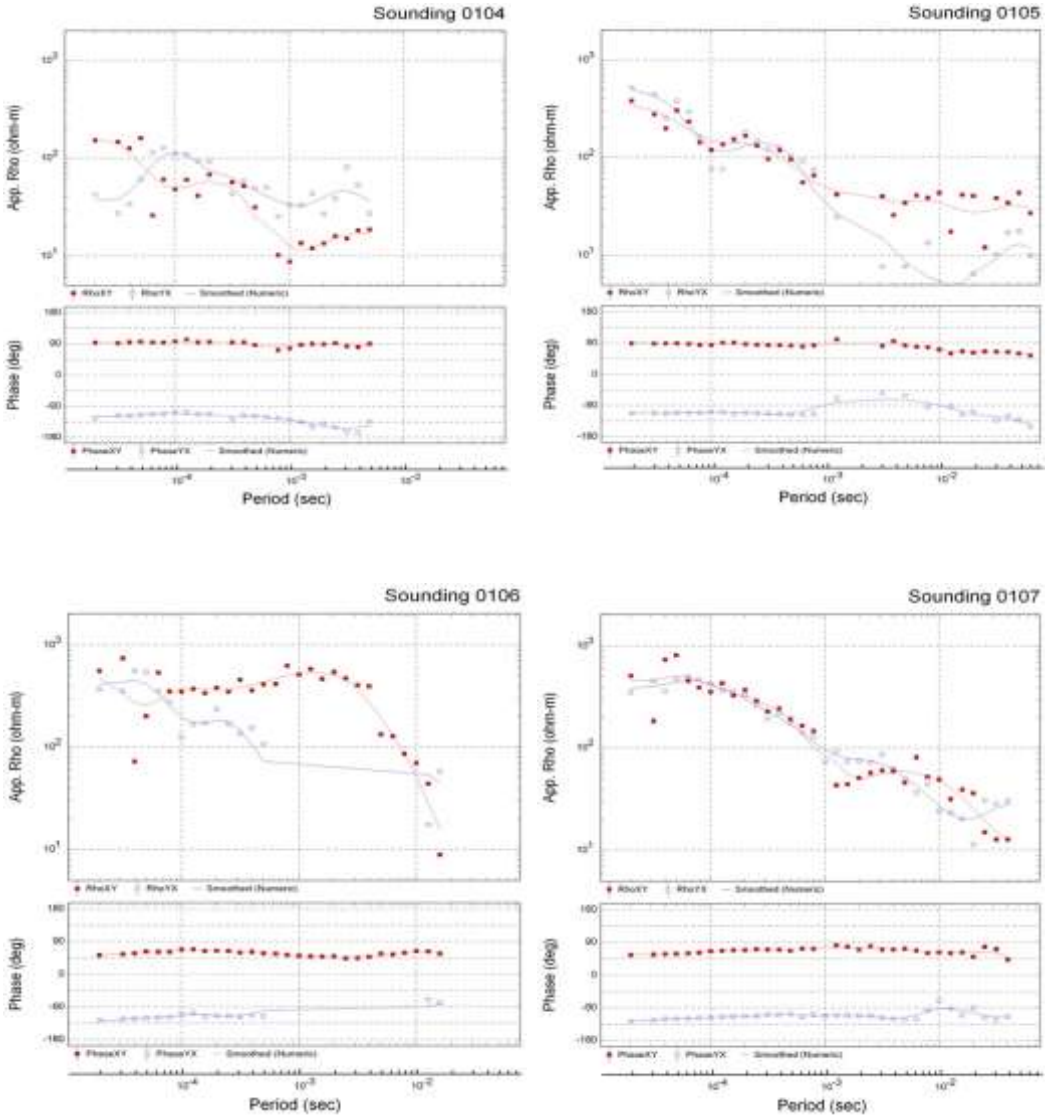
Sounding 0104
Sounding 0105
Sounding 0106
Sounding 0107
App. Rho (ohm-m)
Phase (deg)
Period (sec)

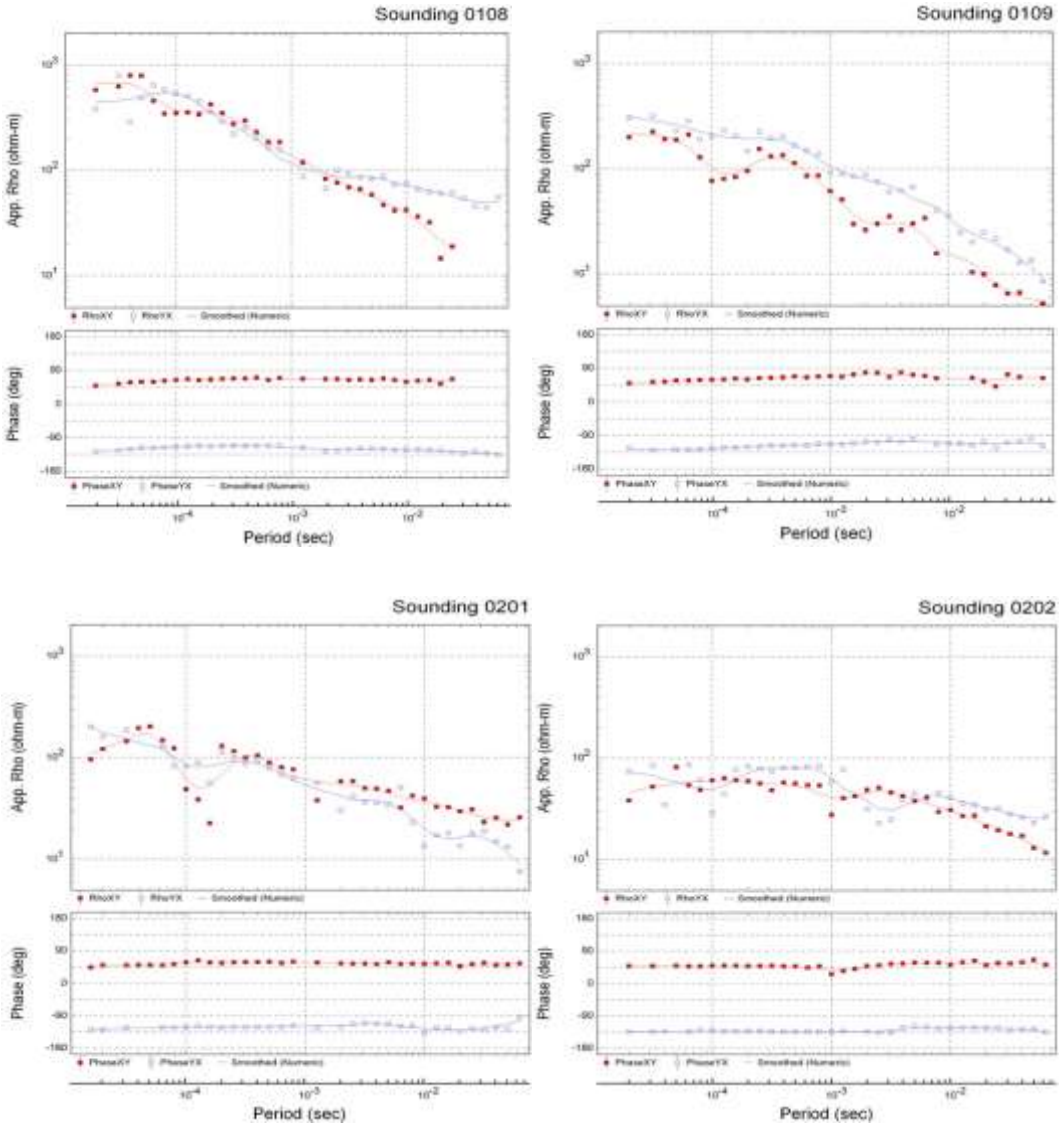
Sounding 0108
Sounding 0109
Sounding 0201
Sounding 0202
App. Rho (ohm-m)
Phase (deg)
Period (sec)

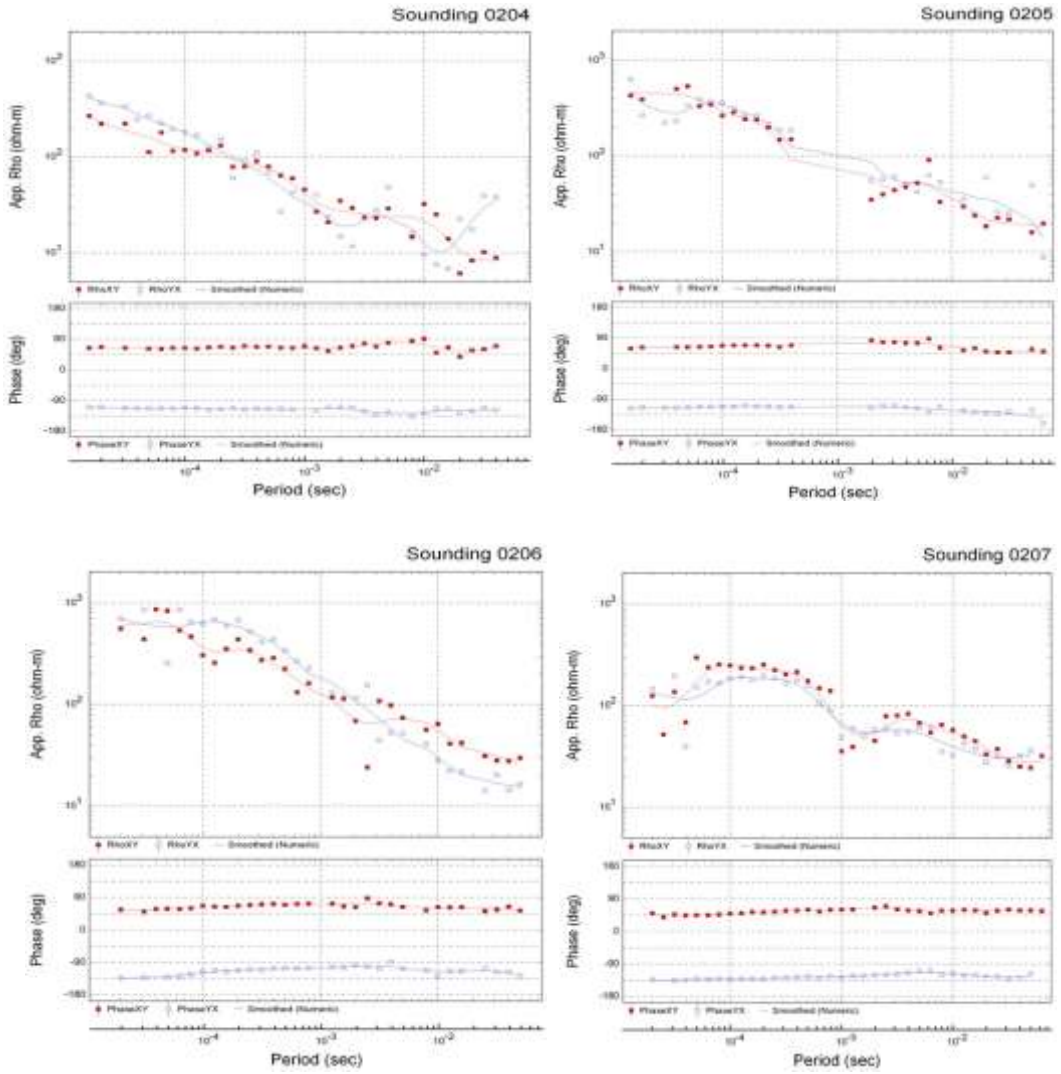
Sounding 0204
App. Rho (ohm-m)
Phase (deg)
Period (sec)
Sounding 0205
App. Rho (ohm-m)
Phase (deg)
Period (sec)
Sounding 0206
App. Rho (ohm-m)
Phase (deg)
Period (sec)
Sounding 0207
App. Rho (ohm-m)
Phase (deg)
Period (sec)

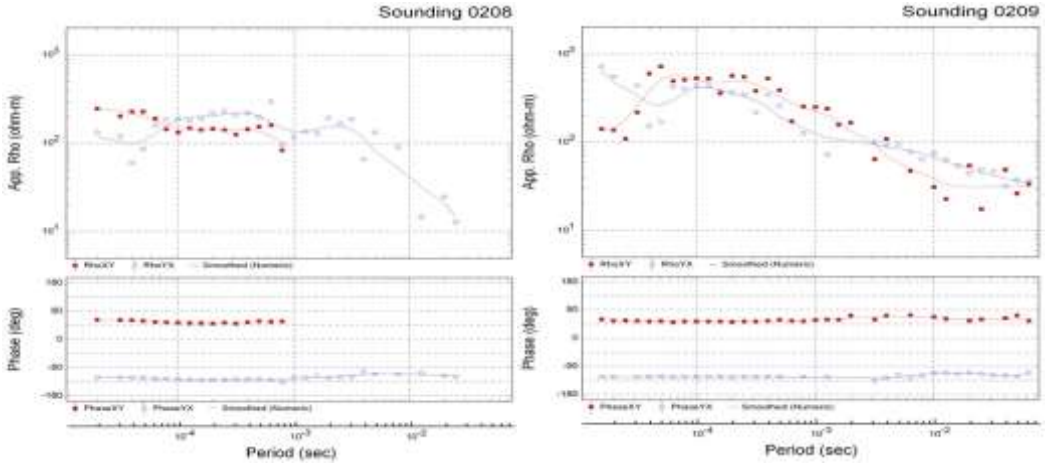
Sounding 0208
Sounding 0209
Sounding 0302
Sounding 0303
App. Rho (ohm-m)
Phase (deg)
Period (sec)

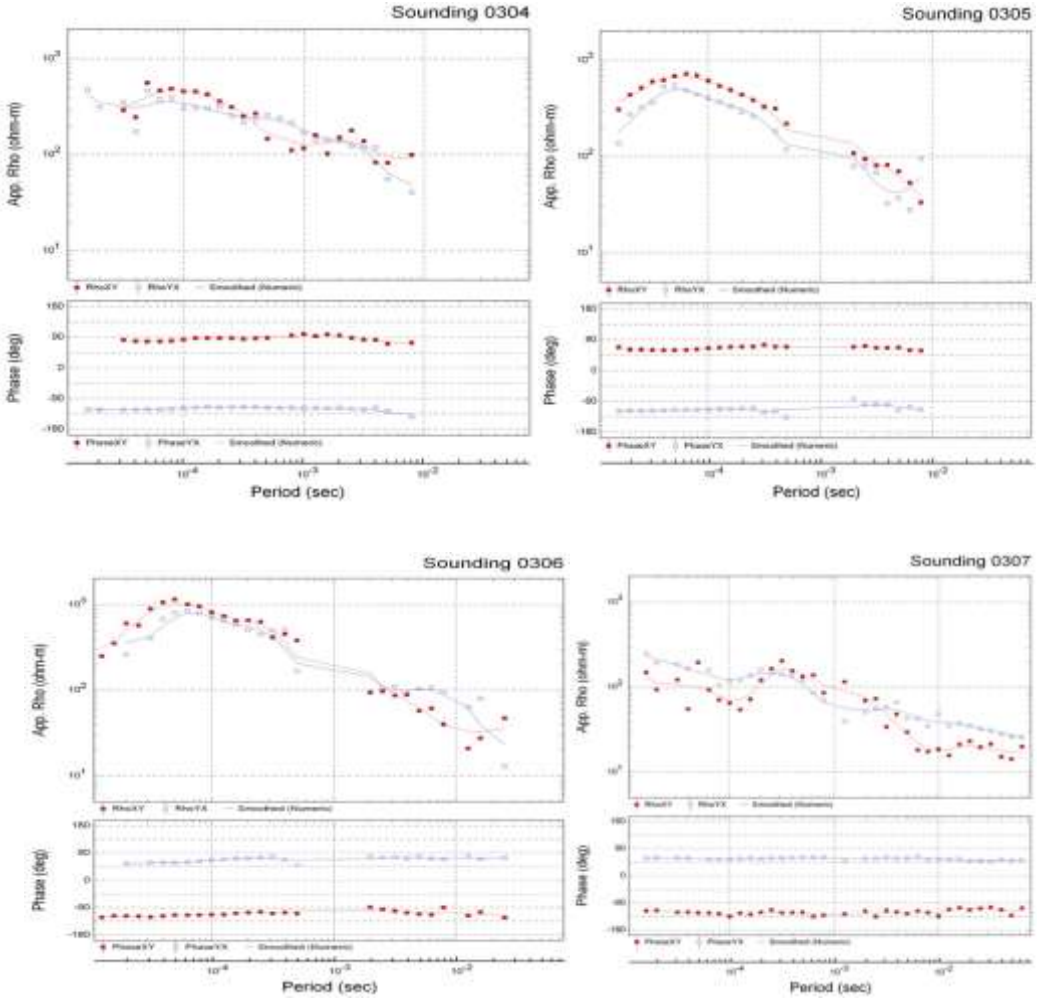
Sounding 0304
Sounding 0305
Sounding 0306
Sounding 0307
App. Rho (ohm-m)
Phase (deg)
Period (sec)

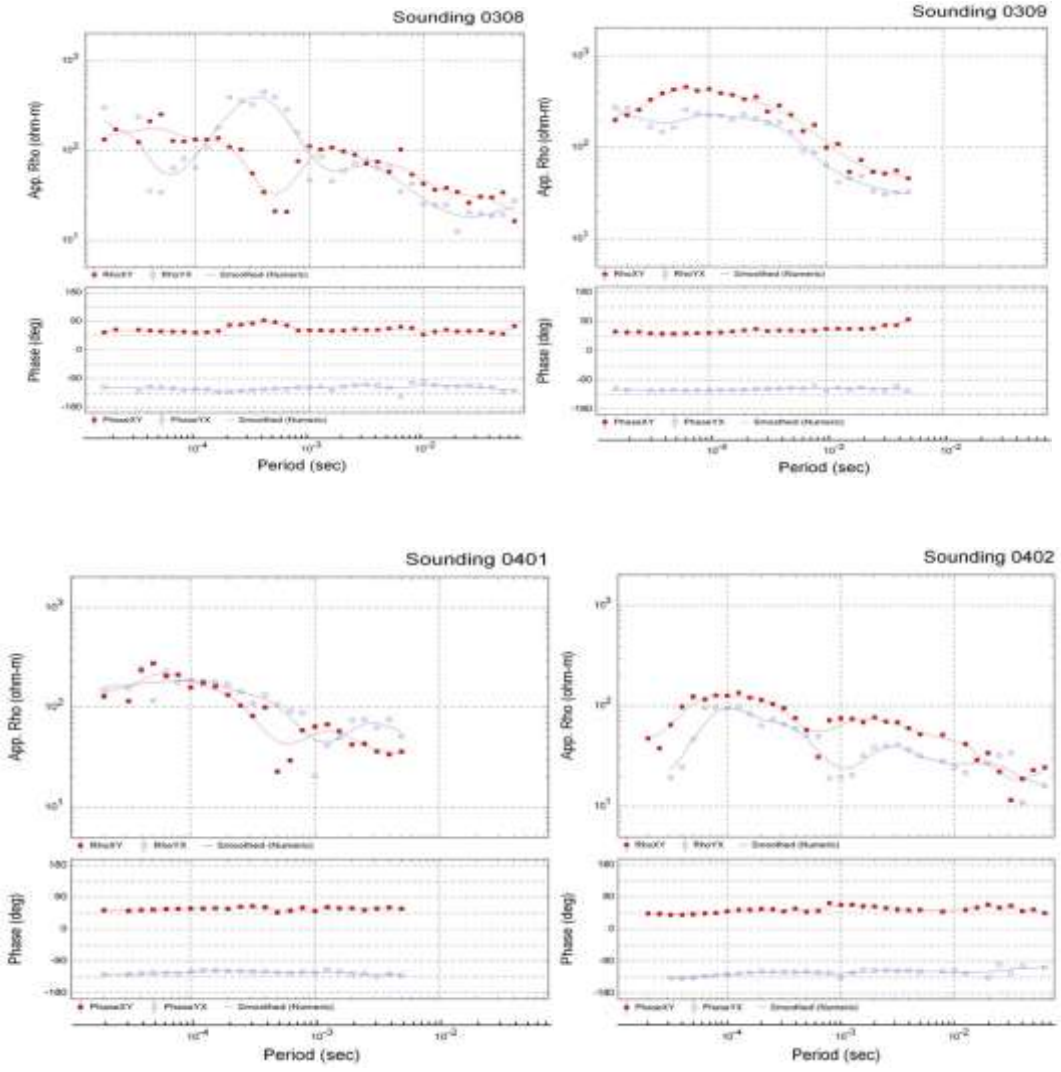
Sounding 0308
Sounding 0309
Sounding 0401
Sounding 0402
App. Rho (ohm-m)
Phase (deg)
Period (sec)

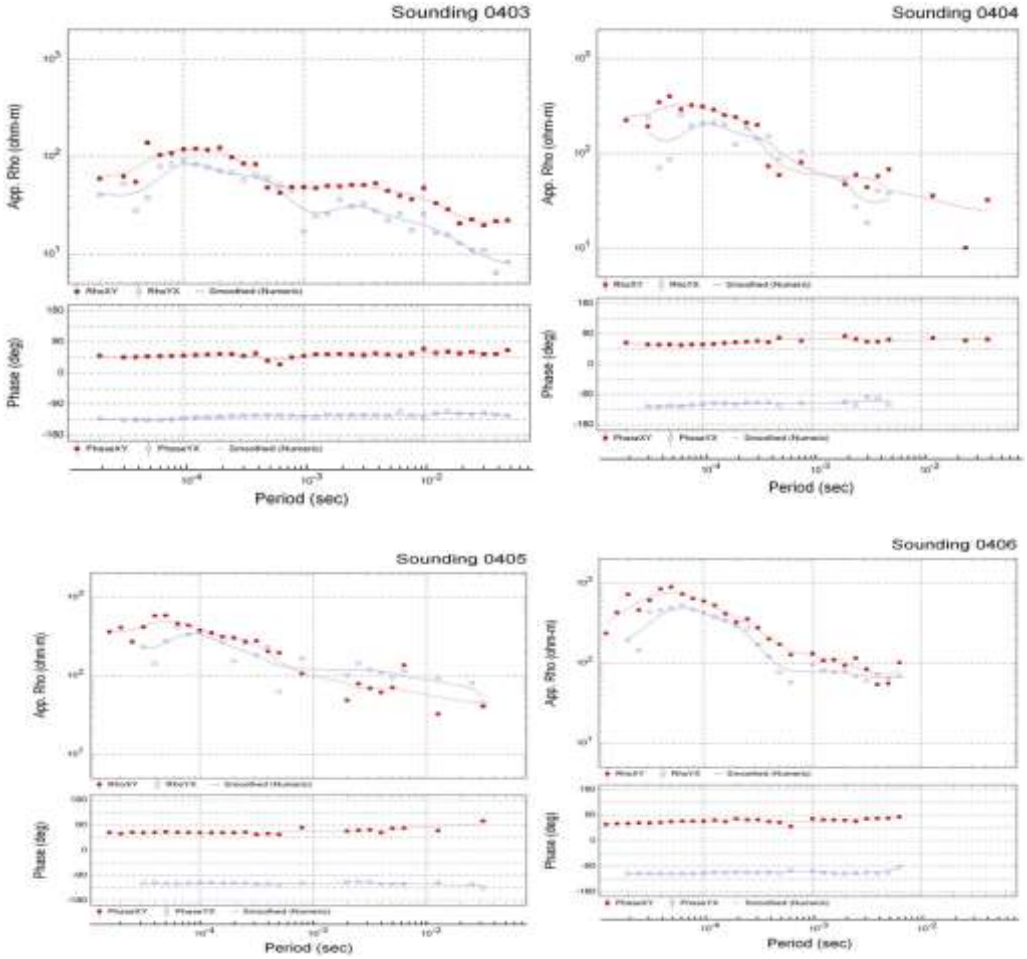
Sounding 0403
Sounding 0404
Sounding 0405
Sounding 0406
App. Rho (ohm-m)
Phase (deg)
Period (sec)

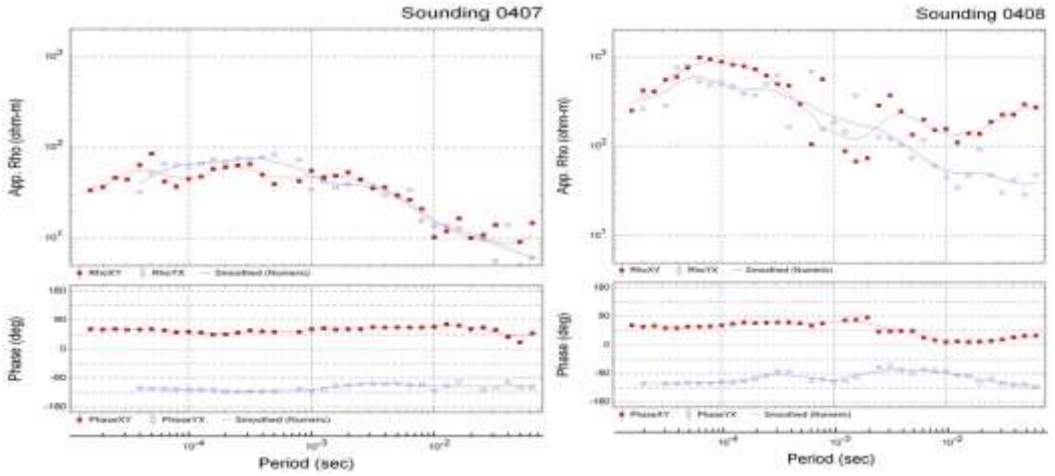
Sounding 0407
App. Rho (ohm-m)
Phase (deg)
Period (sec)

Sounding 0408
App. Rho (ohm-m)
Phase (deg)
Period (sec)

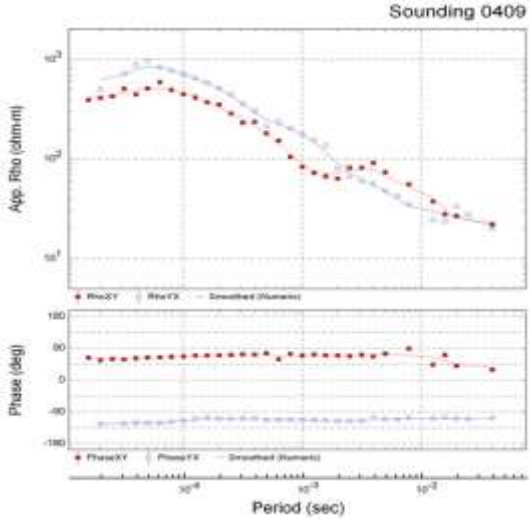
Sounding 0409
App. Rho (ohm-m)
Phase (deg)
Period (sec)

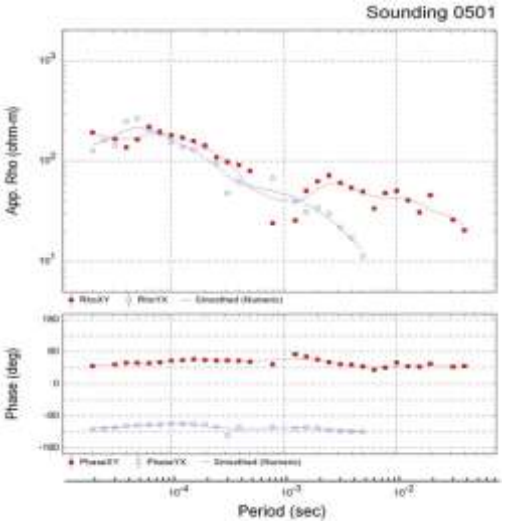
Sounding 0501
App. Rho (ohm-m)
Phase (deg)
Period (sec)

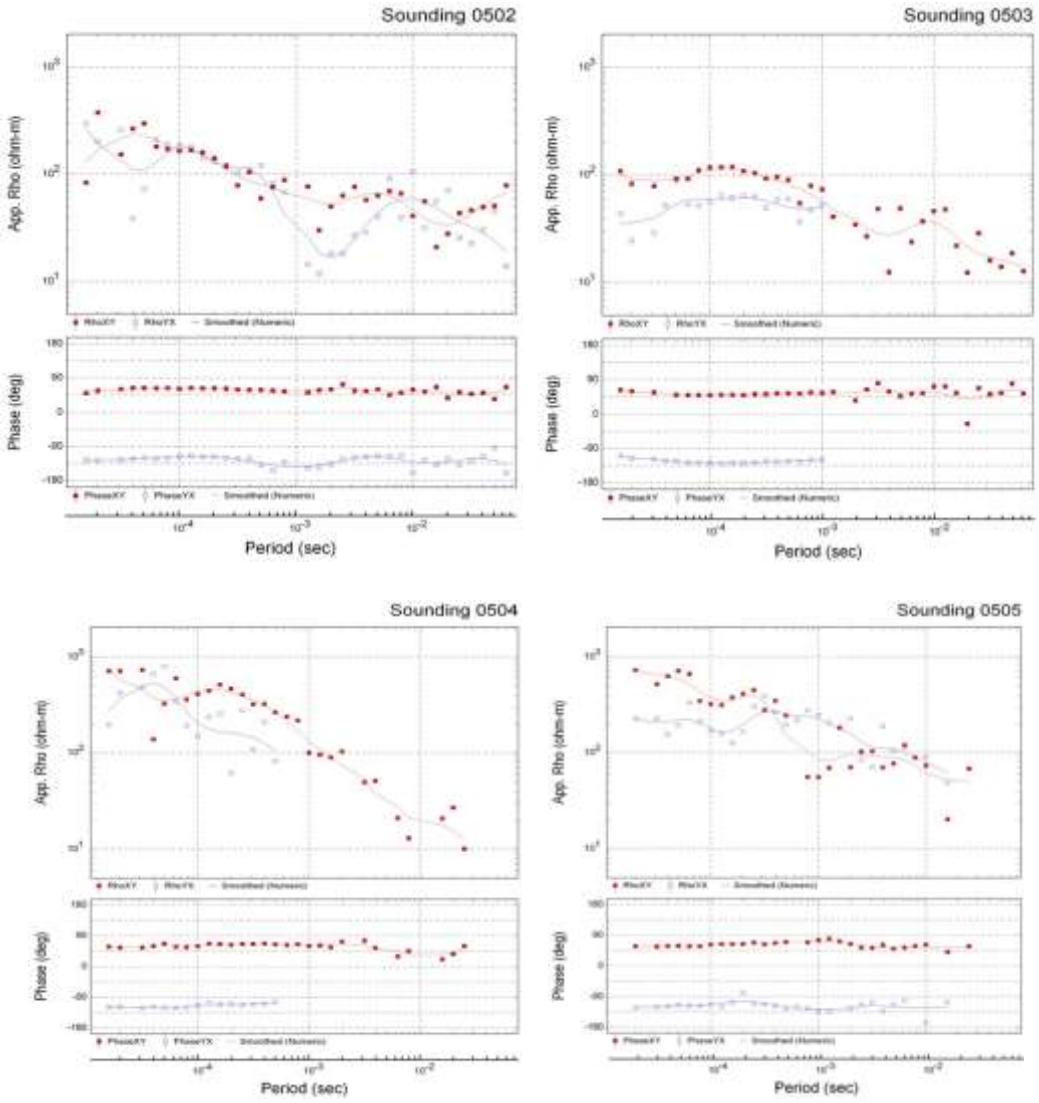
Sounding 0502
Sounding 0503
Sounding 0504
Sounding 0505
App. Rho (ohm-m)
Phase (deg)
Period (sec)

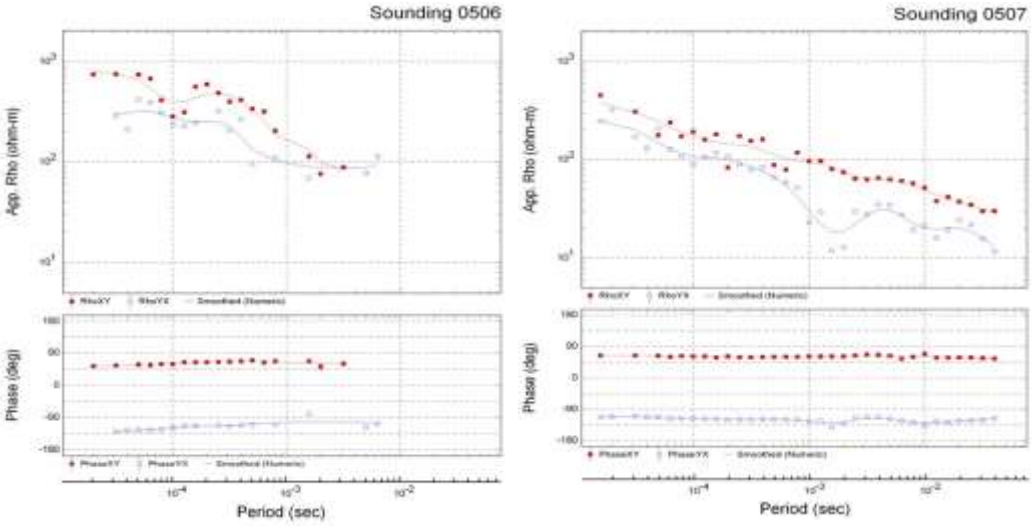
Sounding 0506
App. Rho (ohm-m)
Phase (deg)
Period (sec)

Sounding 0507
App. Rho (ohm-m)
Phase (deg)
Period (sec)

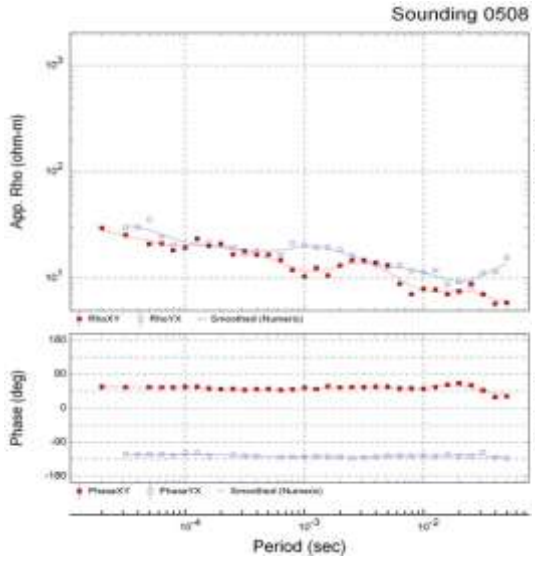
Sounding 0508
App. Rho (ohm-m)
Phase (deg)
Period (sec)

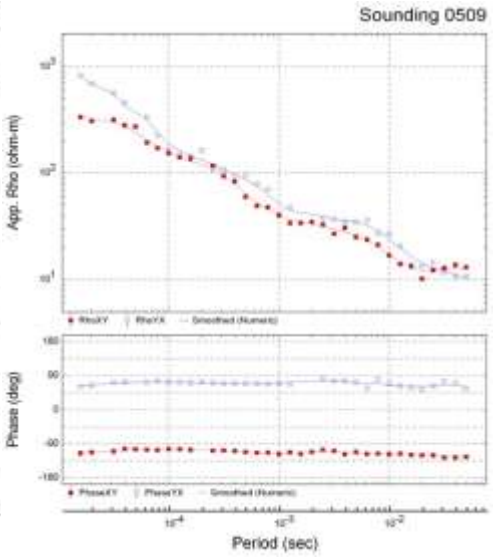
Sounding 0509
App. Rho (ohm-m)
Phase (deg)
Period (sec)

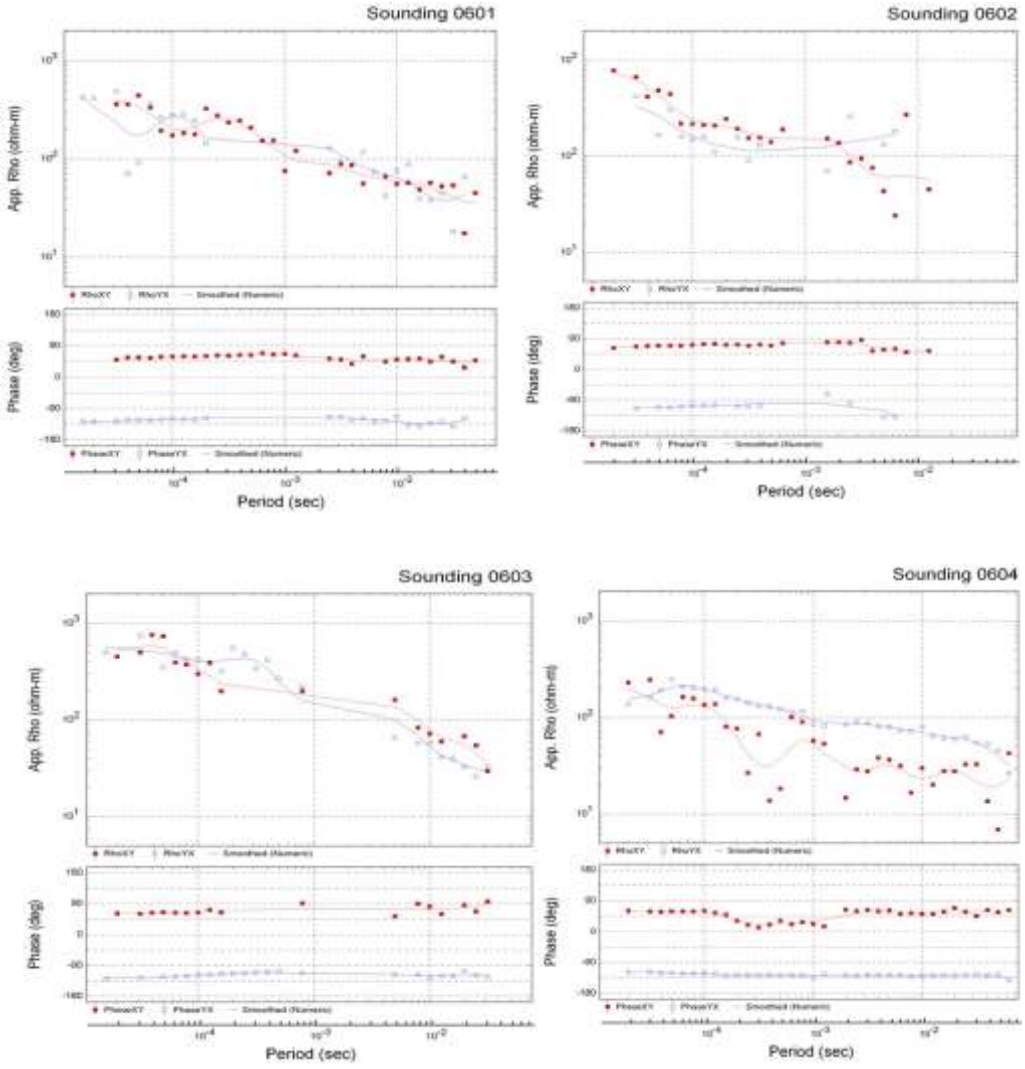
Sounding 0601
Sounding 0602
Sounding 0603
Sounding 0604
App. Rho (ohm-m)
Phase (deg)
Period (sec)

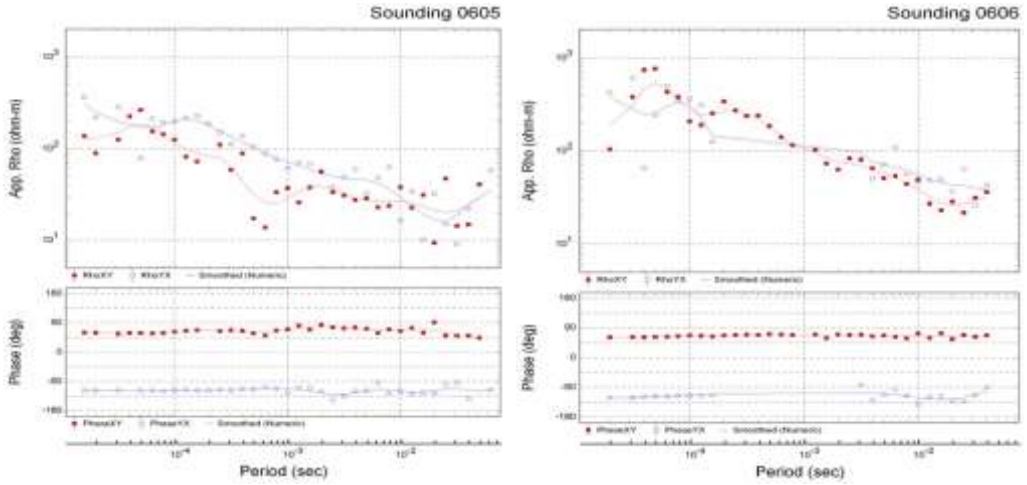
Sounding 0605
App. Rho (ohm-m)
Phase (deg)
Period (sec)

Sounding 0606
App. Rho (ohm-m)
Phase (deg)
Period (sec)

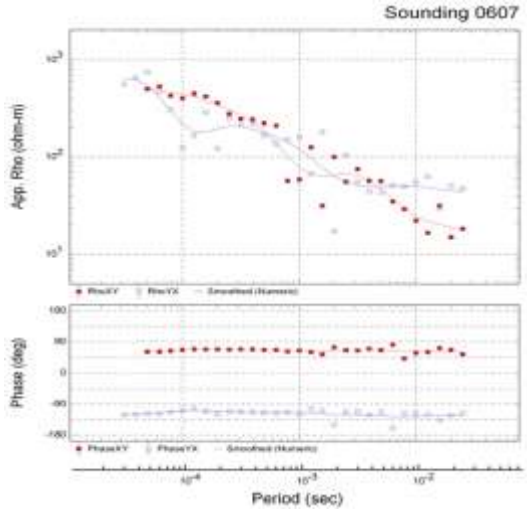
Sounding 0607
App. Rho (ohm-m)
Phase (deg)
Period (sec)

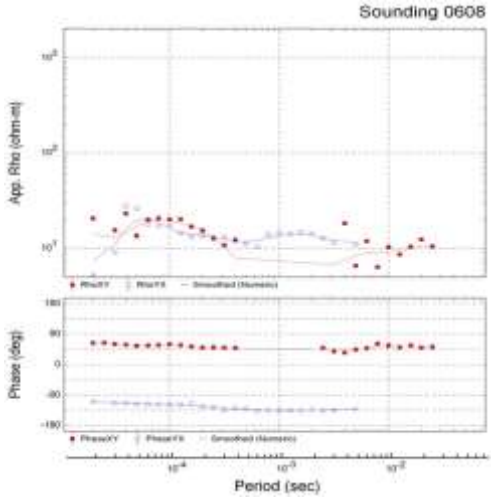
Sounding 0608
App. Rho (ohm-m)
Phase (deg)
Period (sec)

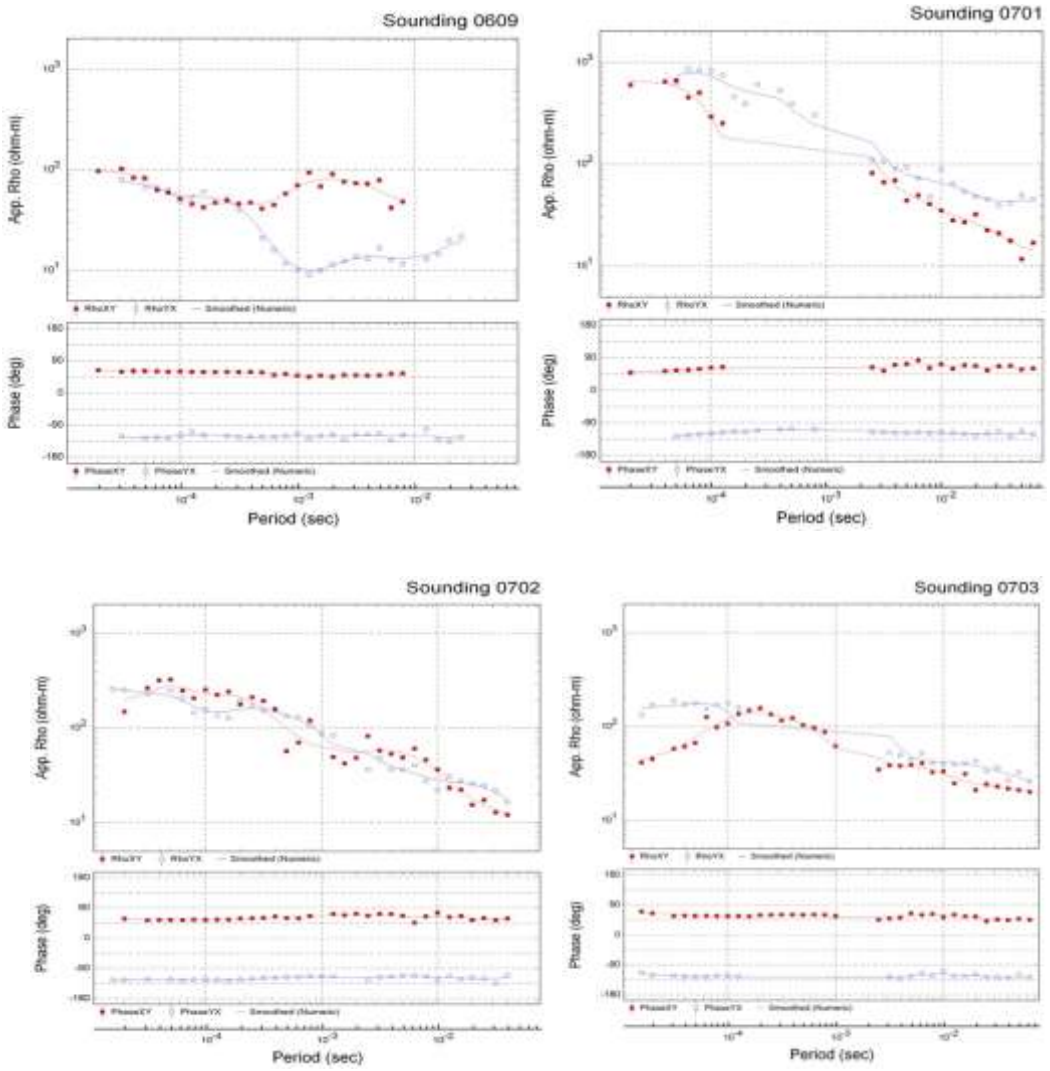
Sounding 0609
Sounding 0701
Sounding 0702
Sounding 0703
App. Rho (ohm-m)
Phase (deg)
Period (sec)

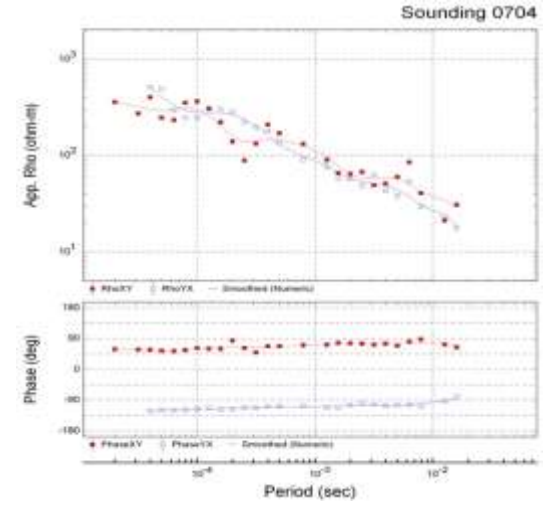
Sounding 0704
App. Rho (ohm-m)
Phase (deg)
Period (sec)

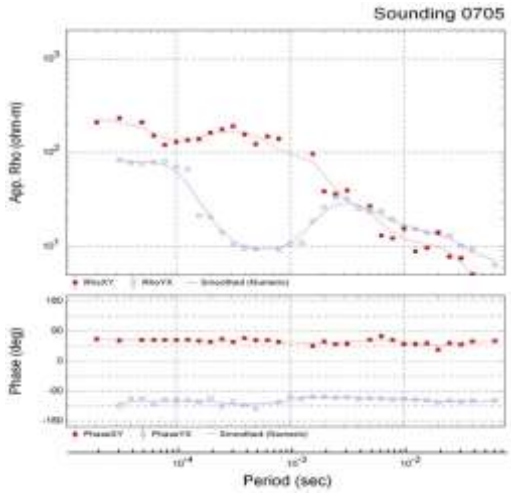
Sounding 0705
App. Rho (ohm-m)
Phase (deg)
Period (sec)

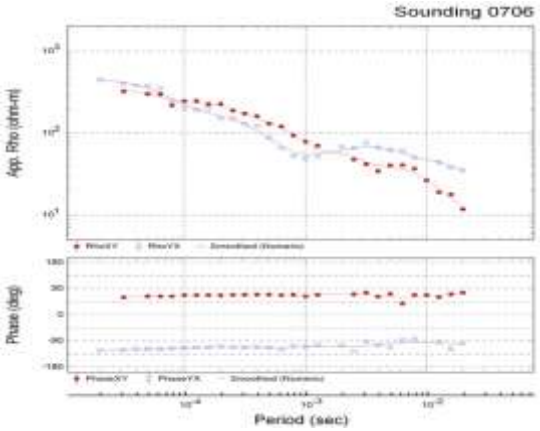
Sounding 0706
App. Rho (ohm-m)
Phase (deg)
Period (sec)

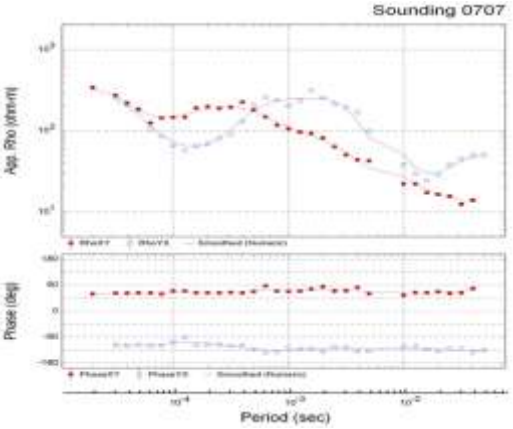
Sounding 0707
App. Rho (ohm-m)
Phase (deg)
Period (sec)

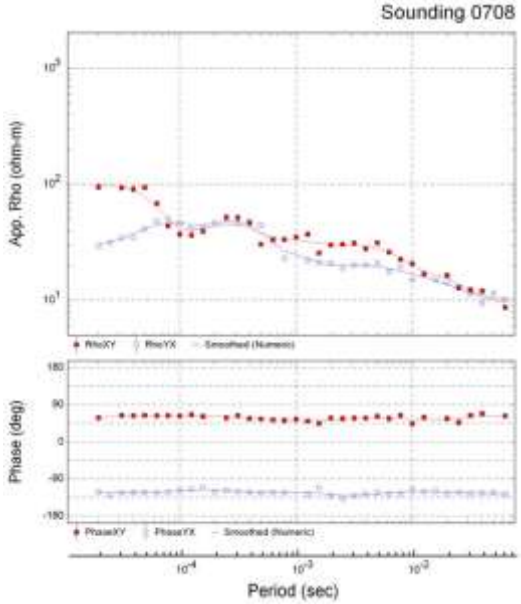
Sounding 0708
App. Rho (ohm-m)
Phase (deg)
Period (sec)

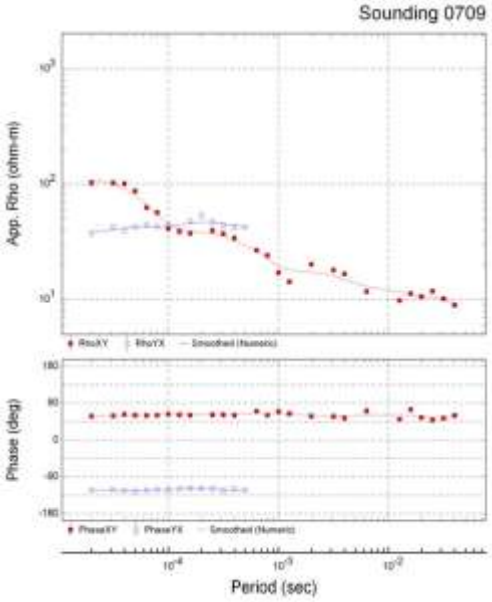
Sounding 0709
App. Rho (ohm-m)
Phase (deg)
Period (sec)

BIBLIOGRAPHY

Abdelghany, O.. (2003). Late Campanian to Maastrichtian foraminifera from the Simsima Formation, western side of the Northern Oman Mountains. *Cretaceous Research*, 24, 391-405.

Al Farraj, A., Harvey, A.M.(2004). Late Quaternary interactions between aeolian and fluvial processes: a case studyin the northern UAE35. *Journal of Arid Environments*, 56, 235–248.

Al Nuaimi, H., Al-Hammadi, M., El-Mahmoudi, A., and Sherif, M. (2003). "Landforms and water resources in the United Arab Emirates: An Overview. Water Resources System.

Al Sharhan, A. S., Rizk, Z. A., Narin, A. E. M., Bakhit, D. W. and AlHajari, S. A.(2001). Hydrogeology of an arid region: the Arabian Gulf and adjoining areas. *Elsevier Science, Netherlands*, 25-53.

Al Sharhan, A.S. and Nairn, A.E.M. (1997). Sedimentary Basins and Petroleum Geology of the Middle East. , Elsevier, Amsterdam. at Laxemar at the Äspö Hard Rock Laboratory, southern Sweden. Appl. Geochem., 15, 953-962.

Barton AB, Zoback MD,Moos D. (1995). Fluid flow along potentially active faults in crystalline rock. *Geology*, 238:683–686.

Blakely, R.J. (1995). *Potential Theory in Gravity and Magnetic Applications*. Cambridge University Press, New York.

Cagniard, L. (1953). Basic theory of the Magnetotelluric Method of Geophysical Prospecting. *Geophysics*, 18, 605-635.

Caine JS, Evans JP, Forster CB. (1996). Fault zone architecture and permeability structure. *Geology*, 24:1025–1028.

Coleman, R. G. (1971). Petrologic and geophysical nature of serpentinites. *Geol. Soc. Am. Bull.* 82, 897-918,

Cook, P.G., Williams, M., Simmons, C.T., Love, A.J., Halihan, T., Herbert, G., and Heinson, G. (2003). *A Guide to Regional Groundwater Flow In Fractured Rock Aquifers*. Seaview Press, Henley Beach, South Australia.

Cordell and Henderson, 1968 L. Cordell and R.G. Henderson. (1968). Iterative three-dimensional solution of gravity anomaly data using a digital computer, *Geophysics*. 33, 4, 596–601.

Edgell, H. Stewart. (2006). Arabian deserts nature, origin and evolution. Dordrecht: Springer.

Elektb Haak V, Simpson F, Bahr K, Bigalke J, Eisel M, Harms U, Hirschmann G, Huenges E, J_dicke H, Kontny A, K_ck J, Nover G, Rauen A, Stoll J, Walther J, Winter H, Zulauf G. (1997). KTB and the electrical conductivity of the crust. *J Geophys Res*. 102 B8:18289–18305

El-Sadek M A. (2009). Subsurface structural mapping of the area lying between Gabal Elgalala Elqibliya and Elgalala Elbahariya, Northern Eastern Desert, Egypt, *Journal of Geophysics and Engineering*.6, 111–119.

Embabi, N.S. (1991). *Dune types and patterns in the United Arab Emirates using Lansat TM data*. 24th International Symposium on Remote Sensing of the Environment. Rio de Janeiro, Brazil.

Fujiwara, T., Kinoshita, H. and Morijiri, R. (1999). Magnetic structure of the southern Boso Peninsula, Honshu, Japan, and its implications for the formation of the Mineoka Ophiolite Belt. *Earth Planets Space*. 51, 413−424.

Garmoon, H. K. F. (1996). Hydrogeological and geomorphological studies on the Abu Dhabi-Dubai-Al Ain triangle, United Arab Emirates. PhD dissertation, Geology Department, Faculty of Science, Ain Shams University, Egypt, 227.

Gartrell, A., Y. Zhang, M. Lisk, and D. Dewhurst. (2004). Fault intersections as critical hydrocarbon leakage zones: Numerical modeling of an example from the Timor Sea, Australia: *Marine and Petroleum Geology*, 21, 1165– 1179.

Geometrics. (2000). Operation Manual For Stratagem systems running IMAGEM Ver. 2.1.

Ghoneim, E. (2008). Optimum groundwater locations in the northern United Arab Emirates. International Journal of Remote Sensing, 29, 20: 5879-5906.

Ghoneim, E. (2009). Ibn-Batutah: A possible simple impact structure in southeastern Libya. *Geomorphology*, 1033, 340-350.

Ghoneim, E., Ozdogan, M., Almulla, A., Koch, M., Ahmad, K., and El-Baz, F. (2005). Thermal anomalies in eastern Arabia: Implication to groundwater recharge. Geological Society of America Abstracts with Programs, 37 7: 107.

Glennie, K. W., Boeuf, M. G. A., Hughes-Clarke, M. W., Moody-Stuart, M., Pilaar, W. E H., and Reinhardt, B.M.(1973). Late Cretaceous nappes in Oman Mountains and their geologic evolution: Am. Assoc. Petrol. Geol. Bull., 57, 5-27.

Glennie, K.W. (2001). Evolution of the Emirates Land Surface: an Introduction. "United Arab Emirates: A New Perspective". London: Trident Press, Edited by edited by Edmund Ghareeb and Ibrahim Al Abed, 9-27.

Glennie, K.W., Boeff, M.G.A., Hughes, M.W., Moody-Stuart, M., Pilaar, W.F.A. and Reinhardt, B.M. (1974). Geology of the Oman Mountains. Konikl. Nederlands Geol. Mijnbowkundig Genoots. Verh., 31, 423.

Goldman, M., H. Gvirtzman, M.A. Meju, and V. Shtivelman.(2005). Hydrogeophysical case studies at the regional scale, in Hydrogeophysics, edited by Y. Rubin and S.S. Hubbard, Springer, The Netherlands, 361–390.

Grant, F.S., and West, G.F. (1965). Interpretation theory in applied geophysics: McGraw-Hill Book Co.

Henriksen, H., 2006. Fracture lineaments and their surroundings with respect to groundwater flow in the bedrock of Sunnfjord, Western Norway. Norwegian Journal of Geology, Vol. 86, pp. 373-386.

http://www.intrepid-geophysics.com/ig/manuals/english/ckdpotdp.pdf

Hudson M.R., Grauch V.J.S., Minor S.A. (2008). Rock magnetic characterization of faulted sediments with associated magnetic anomalies in the Albuquerque basin, Rio Grande rift, New Mexico. Geological Society of America Bulletin in press.

Hunt, C. P., S. K. Banerjee, J. Han, P. A. Solheid, E. Oches, W. Sun, and T.-S. Liu.(1995). Rock-magnetic proxies of climate changes in the loesspalaeosol sequences of the western Loess Plateau of China, Geophys. J. Int., 123, 232–244.

Jiracek, G. R., Haak, V., and Olsen, K. H. (1995). Practical magnetotellurics in a continental rift environment, in K.H. Olsen, ed., Continental rifts: evolution, structure, and tectonics, Elsevier, New York, 103-129.

Jones, A.G. (1998). Waves of the future: superior influences from collocated seismic and electromagnetic experiments. *Tectonophysics.* 286, 273–298.

Kaufman, A.A., and Keller, G.V. (1981). The Magnetotelluric Sounding Method: Elsevier, Amsterdam.

Kazmin, V., Ricou, L.E., Sbortshkov, I.M. (1986). Structure and evolution of the passive margin of the eastern Tethys. *Tectonophysics*. 123, 153-179

Keller, G.V. (1989). Electrical properties, in Carmichael, R.S., Ed., Practical handbook of physical properties of rocks and minerals: CRC Press, Boca Raton, Florida, 359-427.

Kusky, T. Robinson, C. El-Baz, F. (2006).Tertiary-Quaternary faulting and uplift in the northern Oman Hajar Mountains. *Journal of the Geological Society*. 162, 871-888.

Ledo, J., Jones, A.G., and Ferguson, I.J. (2002). Electromagnetic images of a strike-slip fault: the Tintina fault-northern Canadian Cordillera. *Geophysical Research Letters*. 89, 1530–1533.

Lippard, S.J Smewing, J.D. Rothery, D.A. and Browning, P.(1982). The geology of the Dibba zone, northern Oman mountains, a preliminary study. *Journal of the Geological Society*. 139, 59-66.

Mickus, K.(2000). Magnetic Method, Paper 1-9, Presented at the 1st international conference on the Application of Geophysical Methodologies and NDT to the Transportation Facilities and Infrastructure, St. Louis, MO.

Ministry of Agriculture and Fisheries.(1981). Water and soil year book, Ministry of Agriculture and Fisheries, Water and Soil Department, United Arab Emirates, 2, 1977-1979.

Nabighian M. N., Grauch V. J. S., Hansen R. O., LaFehr T. R., Li Y., Peirce J. W., Phillips J. D., and Ruder M. E.(2005). The historical development of the magnetic method in exploration, Geophysics, 70, 33ND-61ND,.

Nasir, S and Klemd, R.(1998). New carbonatite occurrences along the Hatta transform fault zone Northern Oman Mountains, United Arab Emirates, *Journal of African Earth Sciences*. 27, 3–10

Noweir, M.A, Alsharhan, S.A.(2000). Structural Style and Stratigraphy of the Huwayyah Anticline: an Example of an AI-Ain Tertiary Fold, Northern Oman Mountains. GeoArabia, 5,3, 387-401.

Noweir, M.A, Alsharhan, S.A, Boukhary, A. (1998). Structural and Stratigraphy Setting of the Faiyah Range, Northwestere Oman Mountain Front, United Arab Emirates. GeoArabia, 3, 3, 387 398., GulfPetroLink, Bahrain.

Olesen, O., Dehls, J.F., Ebbing, J., Henriksen, H., Kihle, O. & Lundin, E.(2006). Aeromagnetic mapping of deep-weathered fracture zones in the Oslo Region – a new tool for improved planning of tunnels. Norwegian Journal of Geology, 87, 253-267.

Palacky, G.J. (1987). Resistivity characteristics of geologic targets, in Nabighian, M.N., ed., Electromagnetic methods in applied geophysics theory: Tulsa, Okla., *Society of Exploration Geophysicists*. 1, 53–129.

Pearce, J.A., Alabaster, T., Shelton, A.W. and Searle, M.P. (1981). The Oman ophiolite as a Cretaceous arc-basin complex: evidence and implications. Phil. Trans. Roy. Soc. Lond. A300, 299-317.

Poterma, T.A.(1984). Magnetospheric currents: American Geophysical Union.

R.M. Stesky and W.F. Brace.(1973). Electrical conductivity of serpentinized rocks to 6 kilobars, J. Geophys. Res. 78, 7614.

Reid, A.B., Allsop, J.M., Granser, H., Millett, A.J., Somerton, I.W. (1990). Magnetic interpretation in three dimensions using Euler deconvolution. *Geophysics*. 55, 80–91.

Rizk, Z.S. and Al Sharhan, A.S. (2003). Water resources in the United Arab Emirates. In Water Resources Perspectives: Evaluation, Management and Policy, Developments in Water Series 50, A.S. Alsharhan and W.W. Wood Eds, 245–264, Amsterdam: Elsevier.

Rizk, Z.S. and Garamoon, H. (2006). The influence of major lineaments on ground water resources in the eastern region of the northern University of Sharjah. Journal of Pure & Applied Sciences, 3, 83–111.

Rizk, Z.S. (1999). A review article on water resources in the United Arab Emirates. Unpublished Article, Department of Geology, Faculty of Science-Menoufia University, Shebin El Kom, Eygpt, 44.

Robertson, A. H. F., Blome, C. D. Cooper, D. W. nJ., Kemp, A E. S., & Searle, M. P. (1990a). Evolution of the Arabian continental margin in the Dibba Zone, Northern Oman Mountains. In: Robertson, A H. F., Searle, M. P. & Ries, A C. eds the Geology and Tectonics of the Oman Region. Geological Society, London, Special Publication, 49, 251-284.

Robertson, A.H.F., Kemp, A.E.S., Rex, D.C. and Blome, C.D. (1990b). Sedimentary and structural evolution of a continental margin transform lineament: the Hatta zone, northern Oman Mountains. In: Robertson, A.H.F., Searle, M.P. and Ries, A.C., Editors, 1990. The geology and tectonics of the Oman regionGeological Society London, Special Publication 49, 285–305.

Robinson. E. S.(1970). Upward continuation of total intensity magnetic fields, *Geophysics*. 35, 920- 926.

Rodi, W.L., and Mackie, R.L. (2001). Nonlinear conjugate gradients algorithm for 2-D magnetotelluric inversion, *Geophysics*. 66, 174-187.

Roest, W., J. Verhoef, and M. Pilkington, 1992, Magnetic interpretation using the 3-D analytic signal: *Geophysics*. 57, 116–125.

Searle, M. P.(1988). Thrust tectonics of the Dibba zone and the structural evolution of the Arabian Continental margin along the Musandom Mountains Oman and United Arab Emirates. Journal of the Geological Society, London, 145, 43-53.

Searle, M.P. (1983). Sedimentological and structural evolution of the Arabian continental margin in the Musandam mountains and Dibba zones, United Arab Emirates. Geol. Soc. Am. Bull. 94,1381-1400.

Searle, M.P. & Malpas, J.(1980) Structure and metamorphism of rocks beneath the Semail ophiolite of Oman and their significance in ophiolite obduction. Trans. Roy. Soc. Edinburgh, Earth Sciences 71, 247-262.

Searle, Mike and Cox, Jon. (1999). Tectonic setting, Origin and Obduction of the Oman Ophiolite. Geological Society of America, Bulletin, 111, 104-122

Sharma, PV. (1997). Environmental and engineering geophysics. Cambridge University Press, Cambridge, UK, 475.

Singhal, B. S. and Gupta, R. P. 1999 Applied Hydrogeology of Fractured Rocks, Kluwer Academic, Dordrecht, Netherlands.. R.(1964). Computation of magnetic anomalies caused by two-dimensional bodies of arbitrary shape Computers in the Mineral Industries, Part 1 ed G A Parks

Sodsri, S. (1992). The Buckled Belt, Middle East Well Evaluation Review Schlumberger publications, 13.

Styles, M.; Ellison, R.; Arkley, S.; Crowley, Q. G.; Farrant, A.; Goodenough, K. M.; McKervey, J.; Pharaoh, T.; Phillips, E.; Schofield, D.; Thomas, R. J. (2006). The geology and geophysics of the United Arab Emirates : Volume 2, Geology. Abu Dhabi, United Arab Emirates, United Arab Emirates, Ministry of Energy, Petroleum and Minerals Sector, Minerals Department, 351pp.

Tarbuck, E.J., Lutgens, F.K. and Tasa, D. (2006). *Earth: An introduction to physical geology 8/E*. Pearson Prentice Hall.

Talwani,M., Worzel, J.L. and Landisman, M. (1959), Rapid Gravity Computations for two-dimensional bodies with application to the Mendocino Submarine Fracture Zone, Journal Geophysical Research, 64 , 49–59

Talwani. M. and Heirtzler, J. (1964). Computation of magnetic anomalies caused by two-dimensional structures of arbitrary shape. In: Computers in the Mineral Industries, I. Stanford Univ. Publ. Geol. Sci., 9l: 464-480.

Telford, W.M., Geldart, L.P., and Sheriff, R.E.(1990). *Applied geophysics*, Cambridge University Press, Cambridge, UK.

Thompson, D.T.(1982). EULDPH: a new technique for making computer-assisted depth estimates from magnetic data, *Geophysics*. 47, 31–37.

Tikhonov, A.N. (1950). Determination of the electrical characteristics of the deep strata of the earth's crust: Dok. Acad. Nauk., USSR, 73, 2, 295-297.

Unsworth, M.J., and P.A. Bedrosian (2004). Electrical resistivity at the SAFOD site from magnetotelluric exploration, Geophys. Res. Lett., 31, L12S05, doiL10.1029/2003GL019405.

Vozoff, K.(1972). The magnetotelluric method the exploration of sedimentary basins. *Geophysics*. 37, 98−141.

Wallin, B. and Peterman, Z.(1999). Calcite fracture fillings as indicators of palaeohydrogeology at Laxemar at the Äspö Hard Rock Laboratory, southern Sweden. Appl. Geochem., 15, 953-962

Wijns, C., C. Perez, and P. Kowalczyk.(2005). Theta Map: Edge detection in magnetic data:Geophysics, 70, L39-L43.

Woodward G.L. Alsharhan, AS.(1994). Dolomitization and chertification of the Early Eocene Rus Formation in Abu Dhabi, UAE. *Sedimentary Geology*. 91, 273-285.

Yumul Jr., G.P. and Dimalanta, C.B. (1997). Geology of Southern Zambales Ophiolite Philippines: juxtaposed terranes of diverse origin. J. Asian Earth Sci. 15, 413–421

Zhang, Y and Paulson, K.V. (1997). Enhancement of signal-to-noise ratio in natural-source transient magnetotelluric data with wavelet transform, Pure Appl. Geophys. 149, 405–419

Zonge, K.L. and Huges, L.J.(1991). Controlled source audio-frequency magnetotellurics. In: Nabighian, M.N. ed., Electromagnetic Methods in Applied Geophysics. Tulsa, Oklahoma, SEG, 2B, 713-809

VITA

Khalid Ahmad was born on October 4th, 1976 in United Arab Emirates (UAE). He earned his bachelor's degree in Geology (1999) from UAE University in Al Ain, UAE. He finished his master's degree in Geophysics in 2003 from University of Tulsa in Oklahoma, USA. Then he joined University of Missouri, Rolla for Ph.D. program in Geophysics in 2004. The name of the university is changed to Missouri University of Science and Technology while he attended. He earned his Ph.D. degree in geophysics from Missouri University of Science and Technology in 2010.